OPTICAL CHARACTERIZATION OF INHOMOGENEITIES IN BLUE-EMITTING
INGAN/GAN MQWS

by

Cheng Li

A dissertation submitted to the faculty of
The University of North Carolina at Charlotte
in partial fulfillment of the requirements
for the degree of Doctor of Philosophy in
Electrical Engineering

Charlotte

2014

Approved by:

_____
Dr. Edward B Stokes

_____
Dr. Yong Zhang

_____
Dr. Mohamad-Ali Hasan

_____
Dr. Tsing-Hua Her

_____
Dr. Greg Gbur

ABSTRACT

CHENG LI. Optical characterization of inhomogeneities in blue-emitting InGaN/GaN MQWs. (Under the direction of DR. EDWARD B. STOKES)

The growth of blue-emitting InGaN/GaN MQWs, the system setup of a low temperature PL/EL/IV system for temperature dependent PL/EL/IV spectroscopy, and the system setup of a CLSM with nanometer-scale spectrum measurement and TRPL measurement abilities are described. A range of temperature-dependent PL experimental work, CLSM imaging experimental work and TRPL experimental work on blue-emitting InGaN/GaN MQWs are presented.

In temperature-dependent PL measurements, the decreasing of spectrum-integrated PL intensity with increasing temperature is explained with a two-nonradiative-channel model, in which the two nonradiative channels correspond to the thermal activation of carriers out of the strongly localized states and the weakly localized states, respectively. The 'S-shaped' red-blue-red shift of PL peak energy and the 'inverse S-shaped' change of PL FWHM when temperature increases from 10 K to 300 K are explained with carrier localization and carrier dynamics.

CLSM imaging and nanometer-scale PL spectral measurements show that the PL intensity fluctuates in micrometer scale, and that the bandgap energy in bright region is tens of meV smaller than that in dark region. The small-bandgap-energy regions are localization centers which limit the diffusion of the carriers and prevent carriers from diffusing to the NRRCs.

Nanometer-scale TRPL measurements are conducted on blue-emitting InGaN/GaN MQWs for the first time, as far as the author knows. The measurements

show that both bright region and dark region are characterized by two lifetimes: fast decay lifetime τ_1 is smaller than 3 ns and slow decay lifetime τ_2 is longer than 10 ns. The fast decay with shorter lifetime τ_1 corresponds to the carrier localization in weakly localized states, where the radiative recombination is more quenched by NRRCs and also competes with carrier transfer intro strongly localized states. And the slow decay with longer lifetime τ_2 corresponds carrier localization in strongly localized states. The fact that both fast decay and slow decay exist in both bright region and dark region indicates that both bright region and dark region has small bandgap energy fluctuation in themselves. Measurements show that the slow decay lifetime τ_2 in bright region is longer than that in dark region, indicating a higher probability of nonradiative recombination in dark region or carrier transporting from dark region to bright region.

Measurements show that larger bandgap energy difference between small-bandgap-energy regions and large-bandgap-energy regions provides stronger carrier localization effect, via the presence of higher CLSM image average intensity, larger PL intensity ratio and longer smaller-bandgap-energy slow decay lifetime τ_2 when larger bandgap energy difference occurs.

The effect of MOCVD growth parameters on MQW bandgap energy fluctuations and average intensity was analyzed. It was found out that by increasing growth pressure, decreasing growth rate, increasing growth temperature, increasing effective V/III ratio, and increasing gas speed, the bandgap energy difference between bright region and dark region increases, leading to higher average PL intensity.

ACKNOWLEDGEMENTS

TABLE OF CONTENTS

LIST OF ABBREVIATIONS

AFM	atomic force microscopy
$AlCl_3$	aluminum chloride
AlGaN	allium gallium nitride
AlN	allium nitride
APD	avalanche photodiode
APT	atom probe tomography
BPF	band-pass filter
CCD	charge-coupled device
CL	cathodoluminescence
CLSM	confocal laser scanning microscope
Cp_2Mg	bis(cyclopentadienyl)magnesium
CW	continuous wave
DBS	dichroic beam splitter
DLTS	deep level transient spectroscopy
EL	electroluminescence
EQE	external quantum efficiency
eV	electron volts
FWHM	full width at half maximum
GaAs	gallium arsenide
$GaCl_3$	gallium chloride
GaN	gallium nitride

H$_2$	hydrogen
HCl	hydrochloric acid
HVPE	hydride vapor phase epitaxy
He-Cd	helium-cadmium
HTA	high temperature anneal
InCl$_3$	indium chloride
InGaN	indium gallium nitride
InN	indium nitride
IQE	internal quantum efficiency
IR	infrared
IRF	instrument response function
IV	current-voltage
K	Kelvin
LD	laser diode
LED	light emitting diode
LEEBI	low energy electron beam irradiation
LPF	long-pass filter
MBE	molecular beam epitaxy
Mg	magnesium
MOCVD	metalorganic chemical vapor deposition
MQW	multiple quantum well
N$_2$	nitrogen
ND	neutral density

Nd	neodymium
NH_3	ammonia
NRRC	non-radiative recombination center
NSOM	near-field scanning optical microscope
OD	optical density
OPO/OPA	optical parametric oscillator/optical parametric amplifier
PL	photoluminescence
PMT	photomultiplier tube
PZT	lead zirconate titanate
QCSE	quantum-confined Stark effect
RF	radio frequency
RHEED	reflection high energy electron diffraction
RIE	reactive ion etching
RMS	root mean square
RTA	rapid thermal anneal
RRC	radiative recombination center
SEM	scanning electron microscope
Si	silicon
SiC	silicon carbide
SiH_4	silane
SIMS	secondary ion mass spectrometry
SNR	signal to noise ratio
SPCM	single photon counting module

TCSPC	time-correlated single photon counting
TEGa	trimethylgallium
TEM	transmission electron microscope
TD	threading dislocation
TMAl	trimethylaluminum
TMIn	trimethylindium
TMGa	trimethylgallium
TRPL	time-resolved photoluminescence
UV	ultraviolet
YAG	yttrium aluminum garnet ($Y_3Al_5O_{12}$)
Zn	zinc

CHAPTER 1: INTRODUCTION

LEDs (light emitting diodes) are promising solid-state semiconductor light-emitting sources, since they present a lot of advantages over incandescent light sources, such as low energy consumption, long lifetime, fast switching, and small size.

InGaN (indium gallium nitride) is widely used as active material for LEDs, since the bandgap of InGaN is tunable from 0.7 eV (electron volts) to 3.4 eV, expanding from IR (infrared) to deep UV (ultraviolet) and covering the whole visible light range, and green/blue LEDs based on the InGaN-GaN (gallium nitride) system are of high efficiency and brightness.

Because of the 16% lattice mismatch between GaN and c-plane sapphire [1, 2], a large amount of TDs (threading dislocations), with density of 10^8-10^{10} cm^{-2} [3], run along the growth direction. Since TDs work as NRRCs (non-radiative recombination center), it is surprising that even with such high TD density, InGaN MQWs (multiple quantum wells) show high IQE (internal quantum efficiency) [4], while for MQWs made of other semiconductor materials such as GaAs (gallium arsenide), a much smaller TD density would still lead to very low IQE [5].

Much effort has been spent to explain the high-IQE property of InGaN MQWs. It has been suggested that in InGaN MQWs the bandgap fluctuations and resulting carrier localization effect is the reason for the high IQE [6]. These bandgap energy fluctuations

may be caused by micrometer or nanometer scale fluctuations in indium content [7-9] or well thickness [10-15] in InGaN quantum well layer.

A clear understanding of the bandgap energy fluctuation and carrier localization effect is very important, because it may help people to improve the performance of LEDs that are based on InGaN MQWs or even some other materials.

Previous work on InGaN MQWs tended to focus on the origin of the carrier localization effect. Spatially resolved characterization of InGaN emission, using NSOM (near-field scanning optical microscope) [16-20], CL (cathodoluminescence) [21-25], and TEM (transmission electron microscope) [9, 12, 26, 27], have revealed inhomogeneous PL (photoluminescence) intensity and PL peak distributions in InGaN epilayers and QWs. Confocal microscopy has also been used to study spatially resolved PL in green and amber emitting InGaN LEDs [28-32].

The experiments described in the current work involve the investigation of micrometer-scale bandgap energy fluctuation and carrier localization in InGaN MQWs. The research has focused on the structures in the QW layer which have different bandgap energies. Electrons and holes distribute unevenly in the QW layer, as a result of bandgap energy fluctuations.

Temperature-dependent PL measurements have been used to provide an insight into the carrier localization effect in InGaN MQWs. By monitoring the change of PL intensity with increasing temperature and by using curve fitting analysis, it has been possible to show the carrier localization in both stongly localized states and weakly localized states. The dependence of the PL peak energy and PL FWHM (full width at half

maximum) on temperature have also been explained using carrier localization and carrier dynamics.

CLSM (confocal laser scanning microscope) imaging and nanometer-scale PL spectroscopy has been used to investigate the spatial variation of PL peak intensity and bandgap energy. A direct and clear view of bandgap energy fluctuation and carrier localization has been observed.

TRPL (time-resolved photoluminescence) measurements have been used to investigate the carrier recombination processes in different localized states, since the TRPL system has been integrated into the confocal microscope system. Identifying the carrier lifetimes is an important step in the investigation of carrier localization and carrier transportation.

Further experiments have been done on blue-emitting InGaN/GaN MQWs which were grown under different MOCVD (metalorganic chemical vapor deposition) growth conditions. The effect of MOCVD growth parameters on bandgap energy fluctuation and average PL intensity has been investigated. This has important consequences in guiding us the growth of blue-emitting InGaN LEDs with high efficiency.

Chapter 2 discusses the basic physics of III-N semiconductors. The natures of the zinc blende crystal structure and wurtzite crystal structure are described. The basic properties of QWs are explained, including carrier confinement, exciton formation, built-in electric field and QCSE (quantum-confined Stark effect). Finally, the growth of III-N semiconductor material by HVPE (hydride vapor phase epitaxy), MBE (molecular beam epitaxy), and MOCVD is discussed. The growth methodologies and structure for the samples studied in this work are explained in detail.

Chapter 3 discusses in detail the carrier localization effect in InGaN QWs. Carrier localization effect in atomic scale, in nanometer scale and in tens of or hundreds of nanometer scale are introduced. The physics of carrier localization effect in each scale is explained and some of other groups' experiment results are shown.

Descriptions of the experimental devices which were used in this work are presented in Chapter 4. The laser light sources are described, both the CW (continuous wave) He-Cd (helium-cadmium) laser, the pulsed Nd (neodymium) :YAG (yttrium aluminum garnet) laser and the pulsed semiconductor laser. The principles of ultrafast pulse generation are outlined. The basic concept of temperature-dependent PL is introduced, and the temperature dependent PL system which was used in this work is described in detail. The Chapter then discusses the working scheme of confocal microscope and the setup of the confocal laser scanning system which was used in this study. Finally, the chapter explains the principle of the time-correlated single photon counting system.

Chapter 5 describes the result of the experiments. The result of the temperature-dependent PL studies are introduced first, containing the explanations of temperature-dependent PL intensity, temperature-dependent PL peak energy, and temperature-dependent PL FWHM, with carrier localization in different localized states and carrier dynamics. Then the results of CLSM imaging, nanometer scale PL spectral measurements and nanometer scale TRPL measurements are described. The fluctuation in PL intensity, bandgap energy, and PL lifetime are observed and discussed. The last section deals with the effect of MOCVD growth parameters on the bandgap energy fluctuation and the PL brightness of MQWs. The effects of changing growth pressure,

growth rate, growth temperature, effective V/III ratio and effective gas speed are all discussed in detail.

CHAPTER 2: PHYSICS OF III-NITRIDE SEMICONDUCTORS

2.1 Physics of III-N Semiconductors

2.1.1 GaN

Since the introduction of first nitride-based LD (laser diode) in 1994 by Shuji Nakamura [33], GaN has been of great interest to engineers and scientists as a light emitting material. One advantage of III-N materials (including GaN) is that they offer direct bandgap as large as several electron volts, which makes them good candidates for blue-violet light emitting material.

GaN can crystallize in two different structures: the zinc blende structure and the wurtzite structure [34]. Under ambient conditions, it is the wurtzite structure that is thermodynamically stable [35].

In both zinc blende and wurtzite structure, each atom is tetrahedrally bonded to its neighbors, as shown in Figure 2.1. The zinc blended structure has a cubic unit cell, which contains four gallium atoms and four nitrogen atoms. The cubic unit cell, which is similar as the unit cell of diamond crystal structure, contains two interpenetrating face-centered cubic sublattices, offset by 1/4 of the distance along the body diagonal. Along the [0001] direction (c-axis), the crystal structure can be seen as a stack of layers of atoms. For the zinc blende structure, the stacking layers along the [0001] direction are: $Ga_AN_AGa_BN_BGa_CN_C$ [36]. The cubic crystal structure of zinc blende GaN can be described in terms of the edge length a of the cube. a in bulk GaN is determined by using

x-ray diffraction as 4.511-4.52 Å [37]. All III-N semiconductor materials, including GaN, have direct bandgap, which makes them good material for light emitting sources. The bandgap energy of zinc blende structure GaN is 3.2-3.28 eV at 300 K (Kelvin) and 3.302 eV at low temperature [37, 38].
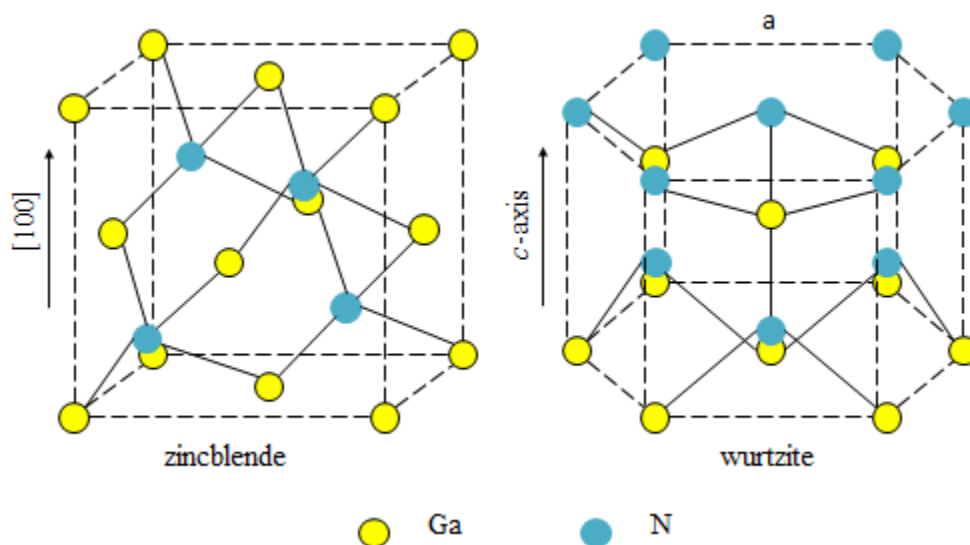
Figure 2.1: The zinc blende and wurtzite crystal structures of GaN. The zinc blende structure can be described using the edge length a, while the hexagonal wurtzite structure can be described using the edge length a of the basal hexagon and the height c of the hexagonal prism.

On the other hand, the wurtzite structure has a hexagonal prism unit cell, which contains six gallium atoms and six nitrogen atoms. The wurtzite structure consists of two interpenetrating hexagonal close-packed sublattices, each with one type of atom, offset along the [0001] direction by 5/8 of the unit cell height. For wurtzite structure, the stacking layers along the [0001] direction are $Ga_A N_A Ga_B N_B$ [36]. The hexagonal crystal structure of wurtzite GaN can be described using the edge length a of the basic hexagon and the height c of the hexagonal prism. The lattice parameters of bulk GaN have been

determined to be *a*=3.189 Å and *c*=5.186 Å [39, 40]. The bandgap energy of wurtzite structure GaN is 3.42 eV at 300 K and 3.505 eV at 1.6 K.

Generally, GaN grown on Si(001) substrate, or on GaAs(001) substrate crystallize in zinc blende structure, while GaN grown on sapphire(0001) substrate, or SiC (silicon carbide) (0001) substrate crystallizes in wurtzite structure.

No matter what structure it crystallizes in, GaN exhibits a built-in electric field containing two components: the spontaneous field and the piezoelectric field [41]. The spontaneous field is the result of the symmetry of the nitride crystal and difference between Ga and N atoms: there is a spontaneous polarization in the unit cell due to the equilibrium positions of the positive and negative charges. The direction of the spontaneous field is determined by the polarity of the crystal. On the other hand, the piezoelectric field occurs because of lattice mismatch between GaN and substrate: the strain in the unit cell leads to piezoelectric polarization. The direction of the piezoelectric field depends on the polarity of the crystal and whether the material is under compressive or tensile stress [42].

When external electric field is not applied, the total macroscopic polarization, which equals the sum of the spontaneous field in the equilibrium lattice and the piezoelectric field introduced by strain, is zero.

2.1.2 InN

InN (indium nitride) is also an important III-N semiconductor material used for light emitting. Similar as GaN, InN can also crystallize in zinc blende structure and wurtzite structure. Because the absence of any reliable data, the bandgap of zinc blende structure InN has not been determined yet. On the other hand, the direct bandgap energy

of wurtzite structure InN has been a source of some controversy. For many years, the bandgap was believed to be around 1.89 eV at 300 K [43], but right now the bandgap has been determined to be 0.78 eV at 300 K [44]. It now appears that early results were wrong due to difficulties in obtaining high quality InN. Oxygen contamination may be the main reason that skewed the early bandgap measurement result, since the bandgap energy of In_2O_3 is 3.75 eV [45], which may push the bandgap upward. Recently, InN films with much lower defect concentration and much higher electron mobility are available because of the improvements in epitaxial growth techniques. However, since InN has very poor thermal stability, it dissociates quickly when temperature reaches beyond 600 °C, which means that to stabilize the material up to the melting point a high growth pressure would be required. On the other hand, the fact that there is large difference between the atom size of In and N leads to tendency to form metallic clusters of the group III constituent, inhomogeneous strain, and highly distorted interatomic distances, making it very difficult to obtain InN with good quality and causing anomalies in all InN's properties.

The cubic crystal structure of zinc blende GaN can be described in terms of the edge length a of the cube as a=4.98 Å, while the hexagonal crystal structure of wurtzite InN has lattice constant of a ranges from 3.533 Å [46] to 3.548 Å [47] and c ranges from 5.693 Å [46] to 5.760 Å [47]. Similar as GaN, InN has a strong built-in electric field containing spontaneous field and piezoelectric field.

2.1.3 AlN

Similar as GaN and InN, AlN (allium nitride) can also crystalize in wurtzite structure and zinc blende structure. Because of the low stability of zinc blende AlN, only

a few zinc blende AlN has been successful grown on zinc blende substrates, such as Si (silicon), 3-C SiC and GaAs substrate [48]. Bandgap-studies indicated a Γ-valley indirect bandgap of 5.34 eV [49], X-valley bandgap of 4.9 eV and L-valley bandgap of 9.3 eV [50] at room temperature. On the other hand, wurtzite AlN has a direct bandgap with bandgap energy of 6.2 eV [51] at room temperature. Because of the very strong bond between aluminum and nitrogen atoms, AlN is very stable and decomposes at temperature as high as 1800 °C.

The zinc blende AlN has lattice constant of a=4.35 Å [52], and the hexagonal crystal structure of wurtzite AlN has lattice constant of a=3.112 Å [53] and c=4.982 Å [53]. Similar as GaN and InN, AlN has a strong built-in electric field containing spontaneous field and the piezoelectric field.

During the growth of AlN, the N overpressure on Al is smaller than that over Ga or In, paving the way for equilibrium growth of AlN bulk crystals [34].

2.1.4 InGaN

InGaN is a ternary semiconductor which is made of a combination of GaN and InN. It has direct bandgap energy that is tunable between the bandgap energy of InN and GaN by adjusting the In/Ga ratio. As a result, InGaN is responsible for light emission in the green, blue, violet, and near-UV colors of the optical spectrum, making it a very promising material for light emitting devices.

In general, the bandgap energy of $In_xGa_{1-x}N$ (where x is the In mole fraction) can be described by following Vegard's law

$$E_g^{In_xGa_{1-x}N} = E_g^{GaN}(1-x) + E_g^{InN}x - bx(1-x) \tag{1.1}$$

where $E_g^{In_xGa_{1-x}N}$, E_g^{GaN}, and E_g^{InN} are the bandgap energy of In$_x$Ga$_{1-x}$N, GaN, and InN respectively, and b is bowing parameter. For wurtzite crystal structure In$_x$Ga$_{1-x}$N, GaN and InN, the bowing parameter is b=2.43 eV [54]. Similarly, the lattice constant of In$_x$Ga$_{1-x}$N follows linear Vegard's law

$$a_{In_xGa_{1-x}N} = a_{GaN}(1-x) + a_{InN} \text{ and } c_{In_xGa_{1-x}N} = c_{GaN}(1-x) + c_{InN} \tag{1.2}$$

where $a_{In_xGa_{1-x}N}$, $c_{In_xGa_{1-x}N}$, a_{GaN}, c_{GaN}, a_{InN} and c_{InN} are the a and c lattice constants for In$_x$Ga$_{1-x}$N, GaN, and InN respectively.

As for GaN and InN, InGaN has a strong built-in electric field. The great difference between gallium atoms and indium atoms makes the 'built-in' electric field even stronger, which could lead to phase separation and other inhomogeneities in InGaN.

2.1.5 AlGaN

AlGaN (allium gallium nitride) is a ternary semiconductor which is made of a combination of GaN and AlN. It has direct bandgap energy which is tunable between the bandgap energy of AlN and GaN by adjusting the Al/Ga ratio. As a result, AlGaN is responsible for light emission in the near UV to deep UV of the optical spectrum.

In general, the bandgap of Al$_x$Ga$_{1-x}$N (where x is the Al mole fraction) can be described by following Vegard's law

$$E_g^{Al_xGa_{1-x}N} = E_g^{GaN}(1-x) + E_g^{AlN}x - bx(1-x) \tag{1.3}$$

where $E_g^{Al_xGa_{1-x}N}$, E_g^{GaN}, and E_g^{AlN} are the bandgap energy of Al$_x$Ga$_{1-x}$N, GaN, and AlN respectively, and b is bowing parameter. For wurtzite crystal structure Al$_x$Ga$_{1-x}$N, GaN and AlN, the bowing parameter is b=1 eV [55]. Similarly, the lattice constant of In$_x$Ga$_{1-x}$N follows linear Vegard's law

$$a_{Al_xGa_{1-x}N} = a_{GaN}(1-x) + a_{AlN} \text{ and } c_{Al_xGa_{1-x}N} = c_{GaN}(1-x) + c_{AlN} \tag{1.4}$$

where $a_{Al_xGa_{1-x}N}$, $c_{Al_xGa_{1-x}N}$, a_{GaN}, c_{GaN}, a_{AlN} and c_{AlN} are the a and c lattice constant for

$Al_xGa_{1-x}N$, GaN, and AlN respectively.

As a result of the wide bandgap and high electronegativity of nitrogen, the acceptor energy levels are rather deep in AlGaN, resulting in lack of shallow acceptor level and difficulties to obtain p-type AlGaN. The most commonly used p-type dopant is Mg (magnesium). However, AlGaN has very large Mg binding energy, which gets even larger when the Al mole fraction is increased [56, 57], leading to small hole concentration and making it very difficult to reach p-type doping AlGaN. Moreover, because of the large bandgap energy, AlGaN has poor ohmic contact, especially for p-type doping AlGaN.

For the study of AlGaN, please check the appendix.

2.2 Quantum Wells

2.2.1 Basic Properties of Quantum Wells

In bulk semiconductors, electrons and holes can move in all three spatial dimensions. However, by fabricating semiconductor structures, it is possible to restrict the number of dimensions electrons and holes can move.

QW is formed by having a thin layer of semiconductor material with narrower bandgap sandwiched between two layers of semiconductor materials with wider bandgap. The thickness of the narrower bandgap layer must be comparable to the de Brogilie wavelength of electrons and holes, so that the effect of quantum confinement can take place. In a QW, electrons and holes are one-dimensional confined and their motion is restricted to a two-dimensional plane. Because of its two-dimensional nature, electrons

and holes in QW has a density of states as a function of energy that has discrete steps, in contrast to smooth square root dependence in bulk semiconductor materials, as shown in Figure 2.2. Additionally, in QW the effective mass of holes in the valence band is changed very close to that of electrons in the conduction band.
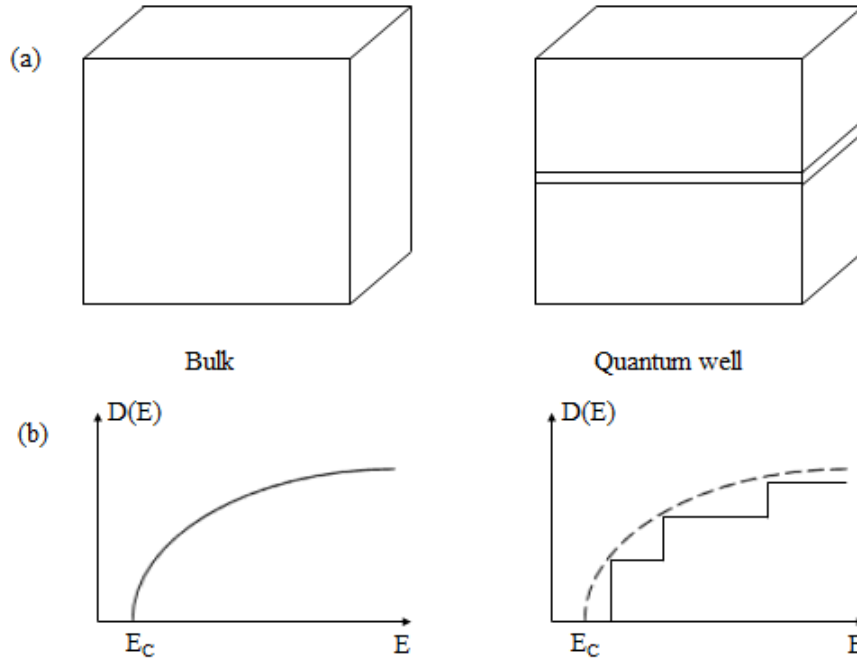
Figure 2.2: Schematic morphology (a) and density of states (b) in bulk semiconductor material and QW.

In the simplified case, the energy levels of a QW with dimension (∞, ∞, d_z) can be calculated by solving Schrodinger equation with appropriate boundary conditions, and is given as [58]

$$E\left(n_z\right)=\frac{\pi^2\hbar^2 n_z}{2m^* d_z^2},$$

(1.5)

where m^* is the effective mass of the carrier, and n_z is the quantum number specifying the quantized levels in each spatial direction [59].

2.2.2 Carriers in Quantum Wells

If a bulk semiconductor material is optically pumped using photons with energy larger than the bandgap of the material, electrons in the bulk material will be excited from the valence band to the conduction band and become free electrons, leaving free holes in the valence band. These free electrons and holes can diffuse in all three dimensions within their lifetimes; as a result, they may be far away from each other. On the other hand, optical-pumping-generated electrons and holes in QW are confined in a two dimensional layer and are restricted in the third dimension in their movement. This increases the overlap of electron and hole wavefunctions, and as a result, increase the probability of recombination between electrons and holes.
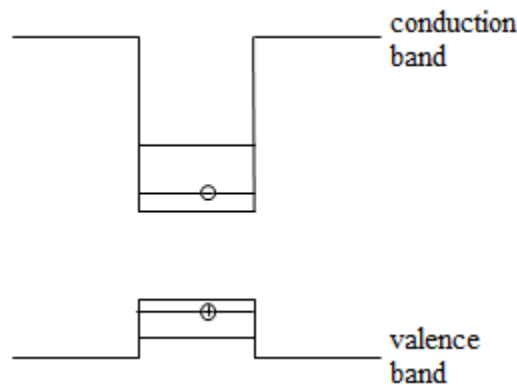
Figure 2.3: One electron and one hole form an exciton in QW.

In the QW, Coulombic attraction can lead to the formation of an excited state in which a hole and an electron remain bound to each other in a hydrogen-like state, which is called an exciton as shown in Figure 2.3. The binding energy of the exciton is determined by the separation of the confined electrons and holes. Over time, it will be possible for the electron and hole that comprise the exciton to recombine radiatively and generate a photon with energy equal to the exciton energy.

2.2.3 Properties of InGaN Quantum Wells

2.2.3.1 Bandgap of InGaN Quantum Wells

InGaN is very important for optoelectronic light emitting sources. With its long recombination time (without the spatial separation of electron and hole wavefunctions), InGaN becomes a good active region material for light emitting optoelectronic sources such as LEDs and LDs. InGaN has narrower bandgap than GaN, which leads to the fact that InGaN quantum well is generally made of InGaN well sandwiched between GaN barriers. Compared to the GaN barriers, it is the narrower bandgap of the InGaN well that leads to the existence of quantum-confined states within the QW. Theoretical calculations can be used to estimate the energy levels of these states: the single-particle properties can be obtained by solving Schrodinger equation within the effective mass approximations and envelope function, using boundary conditions and a plane-wave expression. The single-particle states are then used to calculate the optical matrix elements within the rotating-wave approximations.

2.2.3.2 Built-in Electric Field and QCSE in InGaN Quantum Wells

The built-in electric field in InGaN QWs, consisting of spontaneous field and piezoelectric field, has significant effect on the optical properties of the QWs. If InN is epitaxially grown on GaN, the 11% lattice mismatch would result in the generation of a piezoelectric field as strong as 16 MVcm^{-1}, using calculated piezoelectric coefficients [60]. For In$_x$Ga$_{1-x}$N in QWs with x=0.1~0.2, the lattice mismatch is much smaller than that in the pure InN condition, but a strong piezoelectric field of the order of MVcm^{-1} would still be expected. Since the lattice constant of InN is larger than that of GaN, InGaN QW is compressively strained when grown on GaN, piezoelectric polarization

(P_{PZ}) charges with an opposite sign to spontaneous polarization (P_{SP}), as a result, piezoelectric field (F_{PZ}) is in the opposite direction comparing with spontaneous field (F_{SP}). In polar hexagonal c-plane (0001) InGaN QWs, both spontaneous field and piezoelectric filed are perpendicular to the QW plane: the direction of the spontaneous field is from the substrate to the surface, while the direction of the piezoelectric field is from the surface to the substrate. In nonpolar hexagonal a-plane (11$\overline{2}$0), hexagonal m-plane (1$\overline{1}$00), and cubic (001) InGaN QWs, both spontaneous field and piezoelectric field are parallel to the QW plane.

Built-in electric field in polar c-plane QWs will cause QCSE [61-66]. The QCSE shows the influence of an electric field on the band structure of a QW. When an electric field is not presented, electrons and holes in the QW may only occupy a set of discrete states, as shown in Figure 2.3. However, both the electron states and hole states shift to their lower energies, respectively, when an electric field is presented. This reduces the emission energy of the QW, as shown in Figure 2.4. In addition, since the electric field gives rise to forces on the electrons and holes in opposite directions, it spatially separates electrons and holes and shifts them to the opposite side of the well, which reduces the overlap of electron and hole wavefunctions and reduces the recombination efficiency of the system. Moreover, at high excitation density, the emission energy blue shifts as a result of the reduction in the effective electric field strength by Coulomb screening. Consequently, the built-in electric filed leads to red-shift of PL peak, broadening of PL peak, and longer decay time.
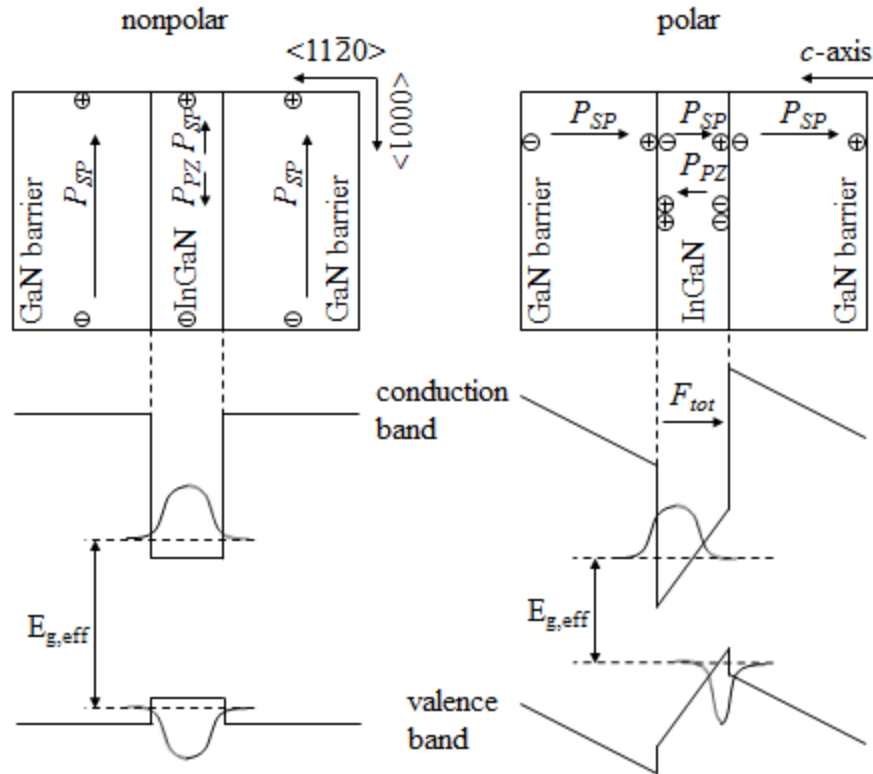
Figure 2.4: Band structure of QW under built-in electric field. The total polarization is generally dominated by piezoelectric polarization due to the large lattice mismatch between GaN and InN [63, 64]. In nonpolar hexagonal *m*-plane (1$\bar{1}$00) [67], hexagonal *a*-plane (11$\bar{2}$0) [68], and cubic (001) [69, 70], InGaN QW, the spontaneous and piezoelectric field are parallel with the sample surface, so the QW does not experience QCSE. In polar hexagonal *c*-plane (0001) InGaN QW, the QW is affected by an electric field pointing from top interface to bottom interface of the QW [62-66]. So the QW band structure is inclined.

2.2.3.3 Carrier Localization in InGaN Quantum Wells

Carriers in the InGaN QWs do not distribute uniformly. This is because of the inhomogeneities in the QW layer, which are the local bandgap energy fluctuations. The bandgap energy fluctuation could be the result of InN molar fraction fluctuation [7-9] or well thickness fluctuation [10-15]. Inhomogeneities can localize electrons and holes in RRCs (radiative recombination centers), or anti-localize electrons and holes from NRRCs. This will be discussed more in detail in Chapter 2.

2.3 Fabrication of InGaN (AlGaN)

2.3.1 Substrates for InGaN (AlGaN) Growth

Though bulk GaN has been produced and are commercially available as native substrate, most of the InGaN (AlGaN) materials are still grown on non-native substrate, considering the high cost of native substrate. So far, the best choice for InGaN (AlGaN) substrate is c-plane (0001) sapphire; in addition, a-plane (11$\bar{2}$0), m-plane (10$\bar{1}$0), and r-plane (1$\bar{1}$02) sapphire have also been used. Other substrates used to grown InGaN (AlGaN) are Si, SiC, and GaAs.

InGaN (AlGaN) grown on a-plane (11$\bar{2}$0), m-plane (10$\bar{1}$0), or r-plane (1$\bar{1}$02) sapphire substrate forms non-polar InGaN (AlGaN). Non-polar InGaN (AlGaN) has less intrinsic defects, and as a result allows the fabrication of optoelectronic devices with an enhanced optical output, shorter radiative recombination lifetimes, and emissions that are blue-shifted with respect to comparable devices made with polar InGaN (AlGaN). Since spontaneous polarization is not an issue in non-polar InGaN (AlGaN), optoelectronic devices made with non-polar InGaN (AlGaN) do not suffer from QCSE. On the other hand, InGaN (AlGaN) grown on c-plane (0001) sapphire substrate has hexagonal symmetric crystalline structure and forms polar InGaN (AlGaN). InGaN (AlGaN) grown on c-plane sapphire substrate has sharp layer interface, smaller point defect density, better material quality, lower dislocation density, and as a result higher EL (electroluminescence) intensity.

2.3.2 Growth of InGaN (AlGaN)

In order to grow high quality InGaN (AlGaN), a lot of crystal growth methods have been investigated and tested. However, the growth of high quality InGaN (AlGaN)

remains very difficult. This is partially because of the lack of native III-nitride semiconductor material substrates. Even though GaN bulk crystals have been produced and limited native substrates are commercially available recently, most of the InGaN (AlGaN) is still epitaxially grown on a non-native substrate, for example, *c*-plane sapphire substrate. Another reason that hinders the growth of high quality InGaN (AlGaN) is the large difference in lattice constant between GaN and InN (AlN), which leads to a solid phase miscibility gap. Typically, the growth of InGaN (AlGaN) is achieved via HVPE, MBE, and MOCVD.

2.3.2.1 Growth of InGaN (AlGaN) by HVPE

One method to grow InGaN (AlGaN) is HVPE [71-73]. In this growth method, HCl (hydrochloric acid) vapor is sent to melting Ga and In (Al), which are in ultra-pure form. Reactions between Ga/In/Al and HCl generate $GaCl_3$ (gallium chloride), $InCl_3$ (indium chloride) and $AlCl_3$ (aluminum chloride), which are then transported downstream to the substrate by carrier gas (H_2 (hydrogen) or N_2 (nitrogen)) separately, in order to avoid the reaction between them before they reach the substrate. $GaCl_3$ and $InCl_3$ ($AlCl_3$) are mixed with NH_3 (ammonia) at the substrate surface at temperature of 600~750 °C for InGaN growth and 1100 °C for AlGaN growth; with this temperature these three compounds decompose, and Ga, In (Al) and N atoms are made available for their recombination into InGaN (AlGaN). When In (Al) source is not used, GaN buffer layer can be grown.

The growth rate can be as high as 0.01-0.5 μm/hr for InGaN [72] and 0.5 μm/hr for AlGaN [34]. InGaN (AlGaN) grown by HVPE tends to exhibit a strong n-type carrier

concentration. HVPE is capable of growing low-defect, crack-free, and high-quality

InGaN (AlGaN) material. A schematic diagram of HVPE reactor is shown in Figure 2.5.
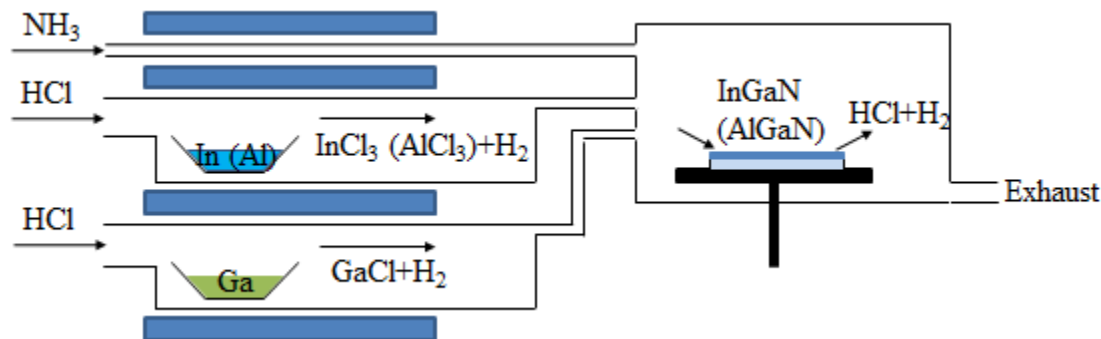
Figure 2.5: Schematic diagram of HVPE [74].

2.3.2.2 Growth of InGaN (AlGaN) by MBE

MBE is a single crystal deposition method that takes place in vacuum or ultra-high vacuum. It depends on the interaction of molecular or atomic beams at the surface of a heated substrate. The ultra-high vacuum and the absence of carrier gas in MBE result in the highest achievable purity of the grown films. A schematic diagram of an MBE system is shown in Figure 2.6.

For growth of InGaN (AlGaN) in MBE, solid elements such as Ga and In (Al), in ultra-pure form, are heated separately in Knudsen effusion cells until sublimation. The gaseous elements are then combined with an NH_3 injector or a source of activated nitrogen, and condensed on the surface of the substrate, where they may react with each other and form InGaN (AlGaN) on the substrate. In the absence of In (Al), which can be achieved by closing the shutter at the output of In (Al) source, GaN can be grown on the substrate. MBE growth of InGaN is typically conducted at temperature between 550 °C and 700 °C [75, 76], while growth of AlGaN is conducted at temperature between 650 °C

and 800 °C [34, 77]. Since the growth is very slow comparing with other deposition methods, MBE is not suitable for large-scale production.
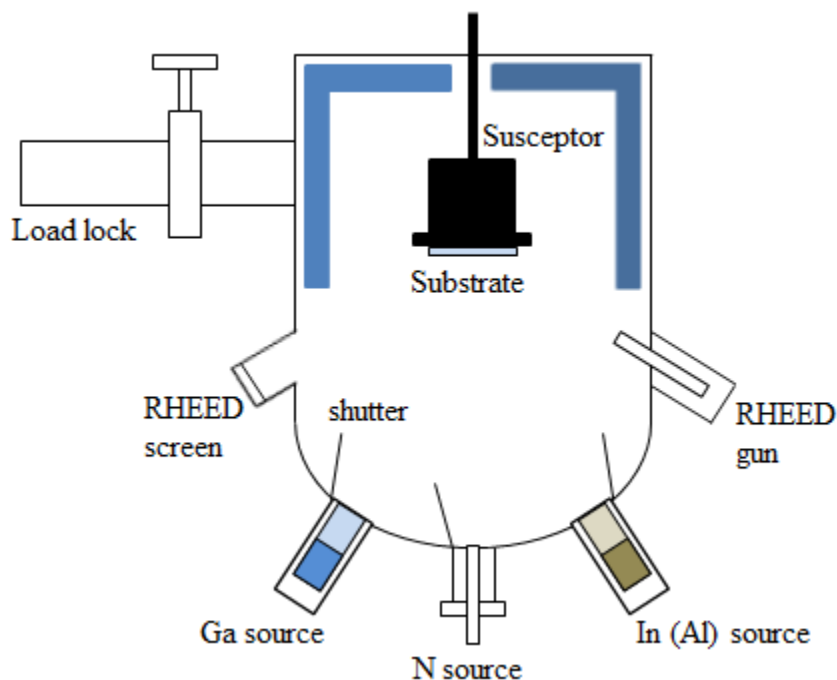
Figure 2.6: Schematic diagram of MBE. The RHEED (reflection high energy electron diffraction) gun and screen are used for in-situ monitoring the growth.

2.3.2.3 Growth of InGaN (AlGaN) by MOCVD

MOCVD, also known as MOPVE, is a complex method that is based on chemical reaction to grow crystalline films on a substrate. Metalorganics and hydrides containing the required chemical elements are diluted in carrier gas and sent to the reactor separately, in order to avoid the reaction between them before they reach the surface of the substrate. TMIn (trimethylindium), TMAl (trimethylaluminum), TMGa (trimethylgallium), TEGa (trimethylgallium) and NH_3 are generally used as the source of In, Al, Ga and N, respectively. N_2 and H_2 are used as carrier gas. However, N_2 is generally used when growing p-type III-V material, since H atoms may form an Mg-H bond with Mg atoms, which is the p-type dopant, and passivate Mg atoms. The growth temperature is related

with the bond strength of the semiconductor material to be grown, and usually ranges between 700 °C and 1100 °C for InGaN and AlGaN[34, 78]. Comparing with MBE, the growth takes place not in vacuum but from the gas phase, in an atmospheric or near-atmospheric pressure. Conventionally, p-type III-N materials, grown by MOCVD, are followed by a post-growth annealing process, to activate acceptor impurities (break Mg-H bond), as it has been suspected that hydrogen is responsible for passivating Mg atoms [79, 80]. A schematic diagram of a MOCVD system is shown in Figure 2.7. The growth rate is ~0.1 μm/hr for InGaN [81] and ~0.5 μm/hr for AlGaN [82].

In addition to the difficulties mentioned before, growth of high quality InGaN (AlGaN) is even more difficult since the high N volatility in InN (AlN) makes it necessary to use high nitrogen pressure over InN (AlN), which leads to a solid phase miscibility gap.

The situation becomes even more difficult for InGaN growth, as a result of the low dissociation temperature of InN, which begins at temperature as low as approximately 600 °C at low pressure [83]. Better crystal quality can be obtained if InGaN is grown at high temperature (800 °C), but very high V/III ratio is required and the indium mole fraction in the alloy is low, which means high NH_3 flow rate is required. In this case, if trying to increase indium pressure in the vapor, indium droplets will form on the surface. Conversely, high indium mole fraction can be obtained at low growth temperature (600 °C), but at the expense of crystalline quality [78].

Growth of InGaN QWs with MOCVD requires that the temperature varies during the growth. InGaN wells are usually grown at a lower temperature than GaN barriers: InGaN is grown around 800 °C, while GaN is grown around 1000 °C. This is because the

thermal disassociation temperature of InN is lower than that of GaN, which makes InN easier to decompose at high temperature. Temperature ramping was usually used for this two temperature growth: after the growth of InGaN well layer/GaN barrier layer, temperature ramps to growth temperature of GaN barrier/InGaN well layer slowly [84].
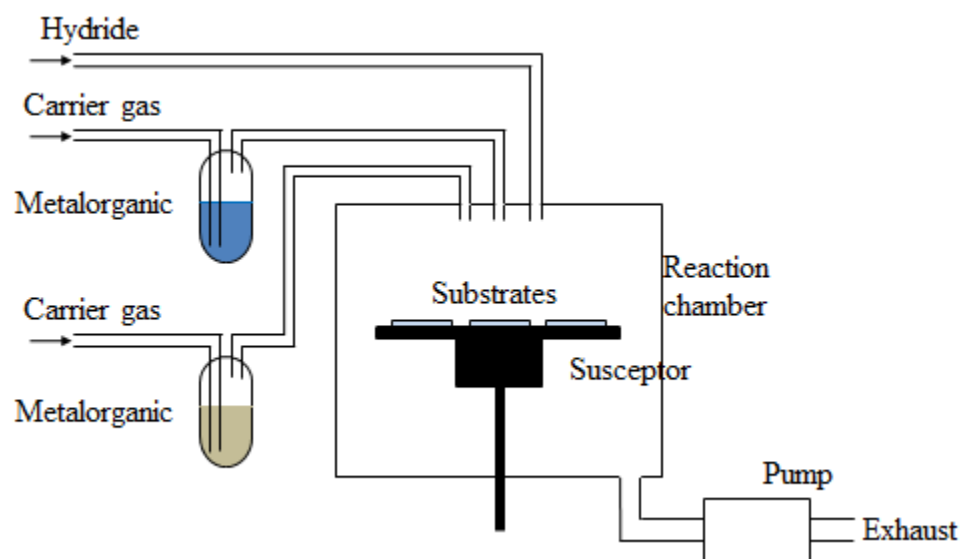
Figure 2.7: Schematic diagram of MOCVD.

2.3.2.4 Blue-emitting InGaN/GaN MQWs Grown by MQCVD

The blue-emitting InGaN/GaN MQW samples in this research were provided by Veeco Instruments Inc. and were grown by Veeco K465i Turbodisc reactor. They were grown on planar c-plane oriented (0001) sapphire substrates, miscut 0.2° towards m-plane. TEGa and TMIn were used as group III sources; NH_3 was used as group V source; and N_2 was used as carrier gas.

The c-plane sapphire substrate was first in-situ cleaned in hydrogen (H_2) atmosphere at 1070 °C for 5-10 minutes, to achieve clean surface for the following crystal growth. Next 25-nm-thick GaN nucleation layer was grown at 500 Torr and 550 °C, to wet sapphire substrate, achieve 2D growth, and provide smooth surface for the

following growth. This nucleation layer growth formed amorphous structure instead of crystal structure. Then, 200-nm-thick GaN roughening layer was grown at 500 Torr and 1000 °C-1050 °C. 3D GaN islands, formed during this growth step, can filter the TDs which were generated at the interface between GaN and sapphire as a result of lattice mismatch and propagated along the growth direction. It should be noted that since the islands grow bigger when thickness increased, new TDs were introduced when islands meet [85, 86]. Then the growth temperature and pressure were set to 1050-1100 °C and 200 Torr, respectively, which were the standard temperature and pressure for growing GaN. A 1-µm-thick uGaN recovery layer was first grown at this temperature and pressure, to smoothen the as-grown 3D surface for the following crystal growth. The growth continued with 0.5-µm-thick GaN buffer layer and 2-µm-thick nGaN, during which SiH_4 (silane) was used as n-type dopant source. The n-type GaN layer ended up with approximately 7×10^{18} cm^{-3} silicon doping level, as measured by SIMS (secondary ion mass spectrometry). The as-grown part that was described above is generally called GaN template. The XRD FWHM of the GaN templates were controlled to a range of 250-270" for ω(002) and 260-280" for ω(102) rocking curves, which translated into a TD density of approximately 4.4×10^8 cm^{-2} [87]. The surface morphology of the GaN templates, measured with AFM (atomic force microscopy) in a 5×5 µm^2 scan area, exhibited a RMS (root mean square) roughness of 0.4 nm. For all the samples used in this research, the GaN templates were identical with equivalent TD density and morphology as mentioned above, leading to near-equivalent TD density in each MQW sample.

Following the GaN template, the MQW structure was deposited, which consisted of four periods of InGaN quantum wells and GaN barriers. The GaN barriers were grown

at 1050-1100 °C and 200 Torr, while the quantum wells were grown at around 800 °C with pressures varying from 100 to 700 Torr. The MQW layer structure was maintained at the same period thickness (2.7-nm-thick InGaN quantum wells and 12.5-nm-thick GaN barriers) as measured using XRD by adjusting both TEGa and TMIn flows while keeping the TMIn/TEGa molar ratio constant. In this case, the MQW structures were close to exactly the same such that QCSE and strain-related internal electric fields were considered not to be a major influence in the run-to-run comparison. The period growth rate was controlled at ~0.9 nm/min. The same TEGa flow rate was used for both QW and barrier layer growth. The growth temperature was adjusted for each sample to achieve a target PL peak wavelength of ~459 nm, corresponding to an indium composition of ~14%. Basically, the 450 Torr sample need to be grown 5-7 °C higher than 200 Torr samples, and 700 Torr samples need to be grown 5-7 °C higher than 450 Torr samples. Despite having near-equivalent structural properties, the samples exhibited different sample average PL intensities, varying by factors of two when measured using a Nanometrics RPMBlue PL system. A schematic diagram of the sample structure is shown in Figure 2.8.
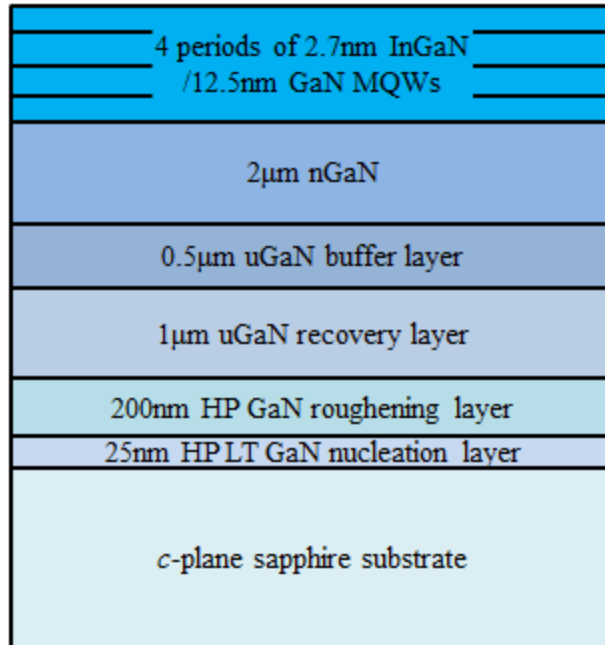
Figure 2.8: Structure of blue-emitting InGaN MQWs provided by Veeco Instruments Inc.

2.4 Summary and Conclusion

Even though the nitride semiconductors GaN, InN, AlN, InGaN, and AlGaN are still not well understood in many areas, they are still of great interest for study and commercial use because of their wide direct bandgap that is tunable between 0.79 eV and 6.2 eV, ranging from infrared to deep ultraviolet. These materials exhibit strong built-in electric fields, containing spontaneous filed and piezoelectric field.

QWs are semiconductor nanostructures in which carriers are confined in one dimension. The carriers in QWs have a density of states as a function of energy that has discrete steps, as a result of their two dimensional movement nature. In QWs made of III-nitride semiconductors, the strong built-in electric field can tilt the band structure and cause QCSE, which will lead to a red-shift of the peak emission energy comparing to the zero-filed case and a longer recombination lifetime.

Several different techniques have been used to grow III-N semiconductor materials, including HVPE, MBE and MOCVD. And MOCVD is nowadays the most commonly used technique. III-N semiconductor materials can be grown on different substrates, and *c*-plane sapphire is the most commonly used candidate. The blue-emitting InGaN/GaN MQWs and Mg doped p-type AlGaN thin film studied in this work were all grown on *c*-plane sapphire substrate by MOCVD.

CHAPTER 3: CARRIER LOCALIZATION EFFECT IN INGAN QWS

3.1 Introduction

As mentioned before, InGaN QWs are generally epitaxially grown on c-plane sapphire substrate, with GaN working as buffer layer. However, because of the 16% lattice mismatch between GaN and c-plane sapphire substrate [1, 2], a large amount (10^8-10^{10} cm^{-2}) of TD run along the growth direction in GaN and InGaN [3]. This TD density is six orders of magnitude higher than the TD density in GaAs thin films or QWs. Since TDs are considered to be NRRCs, it is expected that the NRRC density in InGaN is six orders of magnitude higher than that in conventional GaAs. However, even with such high NRRC density, InGaN QWs show high IQE, while for other semiconductor materials such as conventional GaAs, NRRC density a million times lower would still lead to very low IQE [5]. A lot of work has been expended to explain the high-IQE properties of InGaN QWs. It has been suggested that in InGaN QWs some micrometer-scale or nanometer-scale features localize carriers and prevent them from diffusing to dislocation centers and recombining nonradiatively, resulting in the high efficiency.

Carrier localization in InGaN QWs can occur in different lateral length scales, ranging from single or few atoms scale, through few nanometers scale, to structure with hundreds of nanometers scale.

3.2 Carrier Localization in Atomic Scale

Carrier localization at atomic scale suggests that holes are localized at –In-N-In-chain. This was proved by the experiment in which a positron beam was injected into InGaN thin film. Since positrons have positive charge similar to holes, the behavior of positrons can represent the behavior of holes. The experiment showed that positrons, which are electrons with positive charge, have extremely short diffusion length (<4nm) [1]. This could be attributed to two possible reasons. First, positrons are trapped by group-III vacancies, which form acceptor-type defects and have negative charges. Secondly, as shown in Figure 3.1, since InN has higher valence band maximum than GaN, positrons are trapped at InN side, which is –In-N-In- chain. The first possibility could be wrong, since group-III vacancies are NRRCs which lead to nonradiative recombination of the trapped carriers, this is in contrary to the fact that InGaN thin films have high IQE. As a result, holes, which have positive charges same as positions, are captured by localizing valence states associated with –In-N-In- chain.
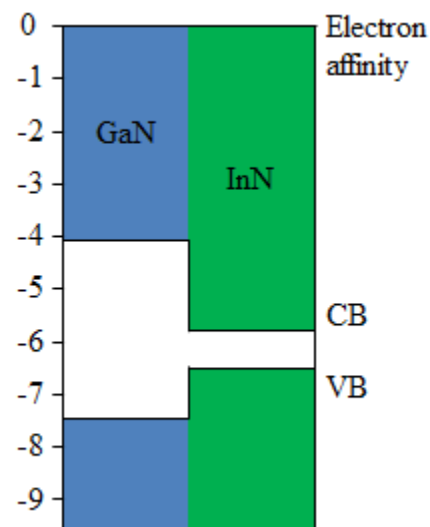
Figure 3.1: Band structure of InN and GaN [88].

3.3 Carrier Localization in Nanometer Scale

The basic idea of carrier localization at nanometer scale is that the bandgap energy of quantum well layer fluctuates in nanometer scale. It is suggested in this theory that the bandgap energy of InGaN quantum well layer is not laterally uniform. Instead, the bandgap energy at some regions are smaller than that at other places [28]. Without these bandgap energy fluctuations, carriers in quantum well layer can diffuse in any direction, reach TD centers and recombine nonradiatively, as shown in Figure 3.2(a). The more the carriers reach TD centers and recombine nonradiatively, the lower the IQE is. On the other hand, with these bandgap energy fluctuations, carriers are localized in regions with smaller bandgap energy and few NRRCs. As a result, carriers have to recombine radiatively in the smaller-bandgap-energy region and cannot reach TD centers and recombine nonradiatively, so a high IQE is expected, as shown in Figure 3.2(b).
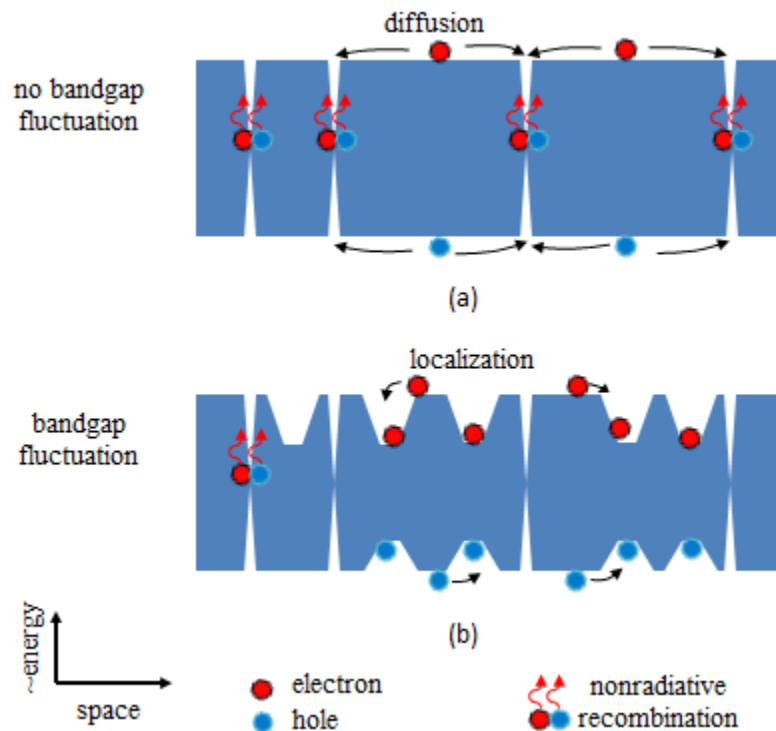
Figure 3.2: Cartoon of bandgap energy fluctuation in nanometer scale.

There are two possible origins of bandgap energy fluctuation in nanometer scale: inhomogeneous distribution of indium content within the QW layer, which is also called indium clustering, and InGaN QW layer thickness variations.

3.3.1 Indium Clustering

The idea of indium clustering suggests that when InGaN quantum well layer is grown with MOCVD, the growth does not end up with a thin film with uniformly distributed indium content, instead, regions with higher indium content than other places are automatically formed [7]. These regions, with higher indium content, are called "self-assembled indium-rich region" or "indium cluster". As shown by the InGaN bandgap calculation equation (Equation 2.1), the higher the indium content is, the smaller the bandgap energy is. So indium clusters, which have smaller bandgap energy than other places in the QW layer, can work as carrier localization centers [89].
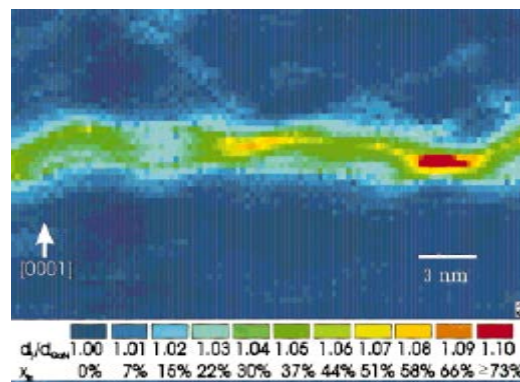
Figure 3.3: Color-coded map of the local indium concentration in blue emitting InGaN/GaN QW, calculated based on TEM lattice fringe images showing strain contrast. An inhomogeneous indium distribution is observed in the quantum well varying between 20% and 80% [26].

A lot of techniques have been used to observe these indium clusters. TEM was used to measure the strain contrast in lattice fringe, based on which the indium mole fraction can be calculated. One TEM measurement showed that the indium clusters had indium mole fraction as high as 80% [26], which leads to a bandgap energy much smaller than the low-indium-content regions, as shown in Figure 3.3. The reason why these indium clusters can form automatically during growth is still not very clear. But it is believed that the phase separation plays and important role in the formation of indium cluster.

However, since these indium clusters are actually calculated based on the strain contrast data that measured by TEM, it is argued that the observed indium cluster are artificial- the strain contrast is generated when the InGaN QW layer is exposed to electron beam in TEM [90-92]. Figure 3.4 shows the TEM lattice fringe images of InGaN QW layer after a series of exposure time. With short exposure time, the lattice fringe image shows very small strain contrast, indicating uniform distribution of indium; while with the increasing of exposure time, strain contrast becomes stronger and indium clusters become more and more clear. As a result, it is possible that the indium clusters observed with TEM are an imaging artifact rather than a self-assembled feature formed during growth.
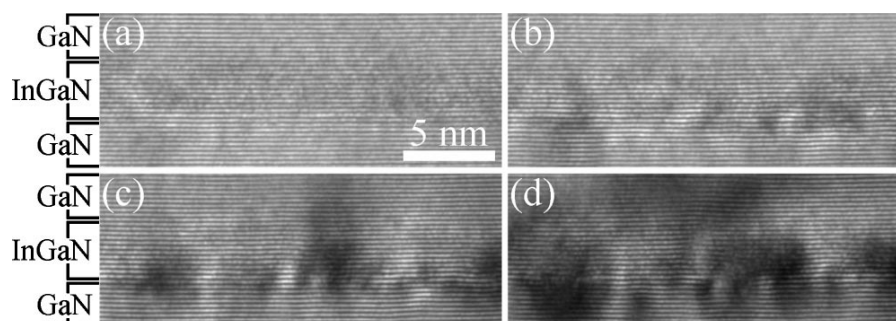
Figure 3.4: (0002) lattice fringe images showing strain contrast evolution in an $In_{0.22}Ga_{0.78}N$/GaN MQW after be exposed to a 200 kV electron beam flux of 35 A/ cm^2 after: (a) 20, (b) 220, (c) 420, and (d) 620 s [90].

In this case, other techniques have been introduced to study the nanostructure of InGaN QW layer, in which APT (atom probe tomography) is a very promising technique since it can provide three-dimensional information about the composition of a sample at sub-nanometer scale [10, 93-95]. In APT a high voltage is applied to the sample, which has needle geometry with radius on the order of 100 nm. In this case, atoms from the needle-geometry sample can be ionized and field-evaporated due to the large electric field. For semiconductor analysis, a laser is generally used to provide pulses of thermal energy and trigger field-evaporation. A radial electric field is used to project the evaporation ions onto a position sensitive detector, and the chemical identities of the evaporation ions are determined by time-of-flight mass spectrometry. Finally, with the data a three-dimensional atom map can be reconstructed. A reconstruction of InGaN MQW APT data is shown in Figure 3.5. It is seen that the distribution of indium atoms in QW layers is pretty uniform, with no indium cluster showing at all. This suggests that the indium clustering may not be the reason of bandgap energy fluctuations.
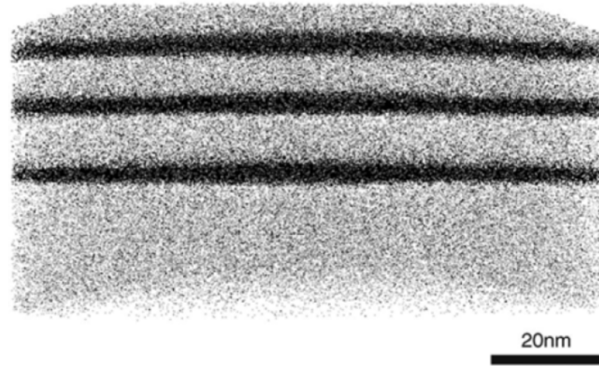
Figure 3.5: Image showing InGaN QWs, reconstructed from APT data. Gallium atoms are shown as gray and indium atoms as black. Other atoms are omitted for clarity. [10]

However, some other researches done by using high-resolution TEM show contrary result. With very short exposure time, the damage caused by electron-beam is minimized. Even though in the resulting high-resolution images no blotchy strain contrast is seen (the images appear pretty uniform to naked eyes), the images are compared with images from QWs which are a random alloy, to get rid of the influence of noise. The results show that for QWs with indium content of 25%, deviations from random alloy can be observed [96], which again proves the existence of indium cluster.

3.3.2 Quantum Well Layer Thickness Fluctuation

As mentioned in Section 1.2.3.2, the built-in electric field in InGaN QWs plays an important role in the optical properties of the QWs. In wurtzite InGaN QWs that is grown on c-plane (0001) sapphire substrate, as a result of the high piezoelectric constants, a strong piezoelectric field of the order of $MVcm^{-1}$ would be expected, leading to strong QCSE. The QCSE tilts the energy band and reduces the effective bandgap energy. With the increment of the quantum well thickness, the lattice becomes more strained, resulting in stronger piezoelectric field, stronger QCSE, and smaller effective bandgap energy. That is to say, quantum well layer with larger thickness has smaller effective bandgap.

For example, for an $In_{0.25}Ga_{0.75}N$ QW layer with thickness of 3.3 nm, if the thickness increases by just one monolayer, the effective bandgap energy would decrease by 58 meV [20]. This suggests that the InGaN QW thickness fluctuations could lead to the QW bandgap energy fluctuation: regions with larger thickness have narrower bandgap.

APT measurement shows that the upper and lower interfaces of InGaN QW layer have different roughness, as shown in Figure 3.6 [10]. The lower interface appears smooth and abrupt, while the upper interface shows islands which are a few nanometers in lateral extent and one or two monolayers high. These islands, with larger thickness, have smaller bandgap energy.
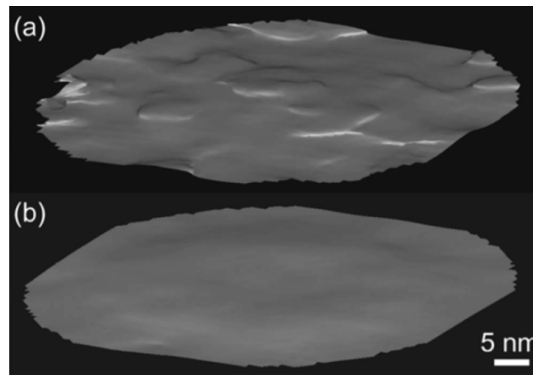
Figure 3.6: The upper (a) and lower (b) interfaces of InGaN QW layer reconstructed from APT experimental data. [10]

It should be noticed that if InGaN QWs are grown with MOCVD without using the two-temperature growth method that was mentioned in Section 1.3.2.3 or grown with MBE, no PL intensity fluctuation can be seen, indicating that no bandgap energy fluctuation exists. In this case, the InGaN QWs show much smaller room temperature ensemble PL intensity and IQE, probably because there is no nanometer scale carrier localization.

3.4 Carrier Localization in Hundreds of Nanometers Scale

When considering the carrier localization effect in a broader-scale structure that is hundreds of nanometer scale, it is no very appropriate to use the term "localization". This is because different from atomic scale or nanometer scale structure, which traps carriers in a small atomic or nanometer scale area, broader-scale structures provide a larger-bandgap-energy region around dislocation centers; so that a barrier is formed to prevent the carriers from diffusing to the dislocations, while the carriers' diffusing freely in other direction in the QW layer is not necessarily prevented. This anti-localization to dislocation effect is also called "dislocation screening".

Several different possible microstructures have been suggested to explain dislocation screening. One possibility is that the V-pits formed around dislocations have thinner QW on their sidewalls, providing regions with larger bandgap energy around the dislocations [97]. Figure 3.7 shows the schematic diagram of this dislocation screening. During the growth of InGaN MQWs in MOCVD, TDs run along the growth direction and form V-pits around them. The size of V-pits expands with the thickness of the film. Because of preferential evaporation of reactive species at the sidewalls of V-pits at InGaN growth temperature, the growth rate at sidewalls of V-pits is much smaller than that at the (0001) growth plane. So the MQWs thickness at sidewalls is thinner than that at (0001) growth plane, as shown in Figure 3.7(a)(b). Because of the piezoelectric field and QCSE, thinner quantum wells are less strained and have smaller band-bending, which results in a wider bandgap, as shown in Figure 3.7(b). Moreover, the bandgap energy at sidewalls of V-pits becomes even larger because of lower indium content in the sidewalls, which is the result of easily evaporation of reactive species. Sidewalls with

larger bandgap energy around the TDs act as barriers to prevent carriers from reaching TD centers and recombining nonradiatively.

A very important proof of this theory is that for InGaN QWs grown by MBE no V-pits have been reported so far, which may explain the reason why InGaN QWs grown by MOCVD exhibit much higher efficiency than comparable InGaN QWs grown by MBE, since in the MBE grown MQWs no self-screening from the dislocations is presented.
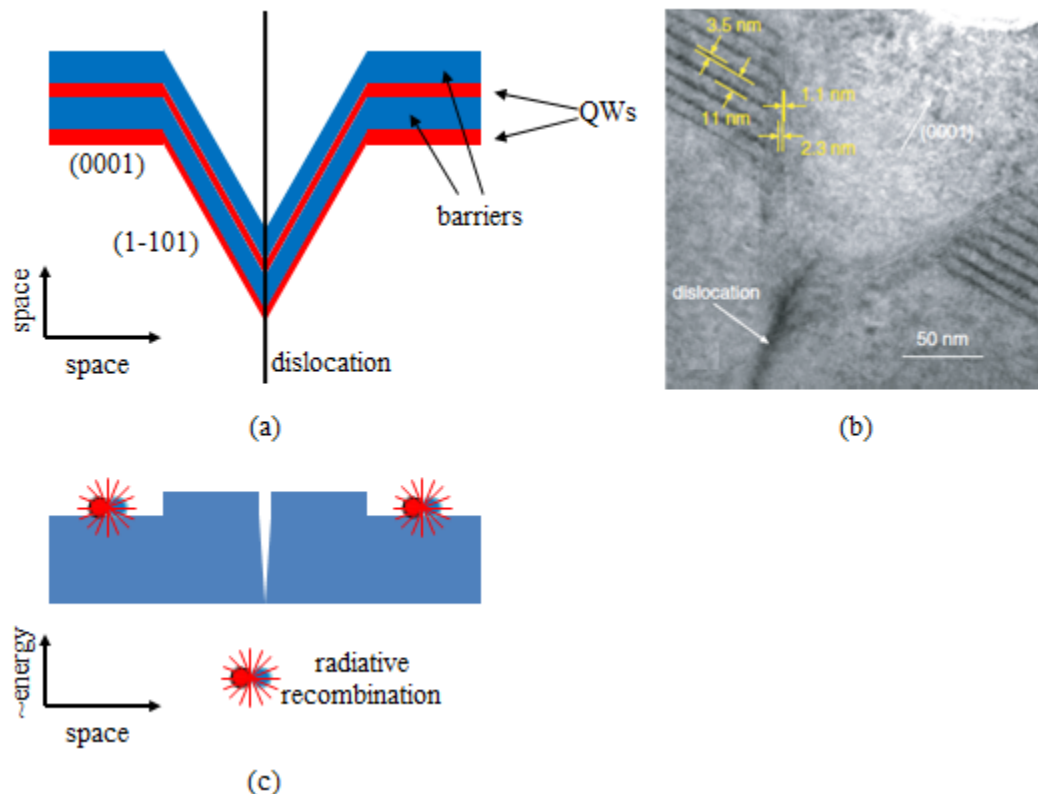
Figure 3.7: Schematic diagram (a), TEM image [97] (b), and bandgap diagram (c) of V-pits in InGaN MQWs.

Another possibility is that the QW width drops to zero on lateral scale of several hundreds of nanometers, resulting in a gap filled with GaN in the quantum well layer [9, 98-100]. In this case, QW layer can be seen as InGaN strips which are interlinking and

separated by GaN-filled troughs. About 90% of the TDs are observed to pass the QW layer through the GaN gaps or through the very edges of the InGaN strips where APT measurements show both low indium content and low QW thickness. In Figure 3.8(b), an InGaN QW, which was grown under the same condition as the InGaN epilayer in Figure 3.8(a), shows similar pattern as Figure 3.8(a) in its CL image. The InGaN strips appear bright in Figure 3.8(b) as a result of the higher probability of radiative recombination. Based on the position of V-pits in SEM (scanning electron microscope) image, which was recorded at the same time with the CL data, the position of the TDs can be identified. In Figure 3.8(d), the combination of the CL and SEM image shows that 92%±7% of the TDs pass the QW layer through the GaN troughs or the very edge of InGaN strips, where the bandgap energy is larger than the bandgap energy in InGaN strips. Consequently, local potential barriers around the TD cores are provided through the gappy QW layer.

3.5 Summary and Conclusion

Regardless of the high density of TDs, InGaN QWs show high IQE. People attribute this high IQE property to carrier localization, which prevents carriers from diffusing to NRRCs and recombining nonradiatively.

In atomic scale, holes are localized at –In-N-In- chain, and electrons are localized around holes because of the formation of excitons.

In nanometer scale, bandgap fluctuates as a result of indium clustering or InGaN quantum well layer thickness fluctuation. Regions with higher indium composition or larger quantum well thickness have smaller bandgap energy, which localize carriers.

In hundreds of nanometer scale, carriers are anti-localized to TDs, as a result of larger bandgap energy regions around the TD centers, which are provided by the sidewalls of V-pits or gaps filled with GaN in InGaN quantum well layer.
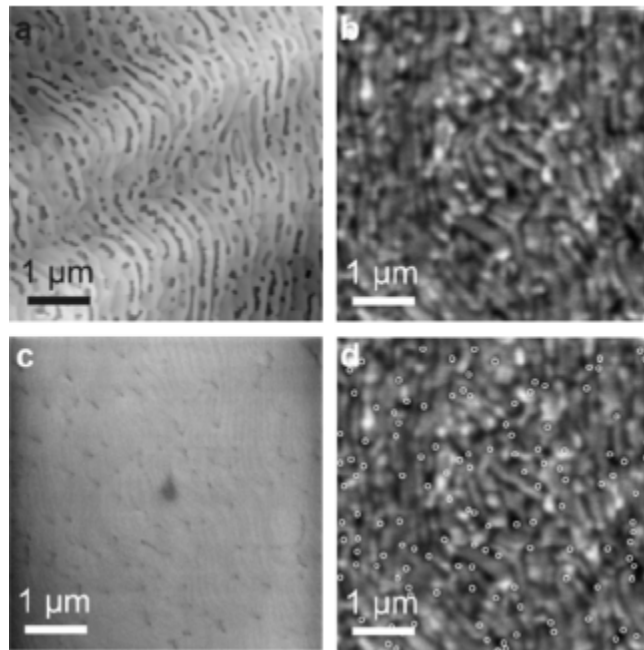
Figure 3.8: (a) AFM image of an annealed InGaN epilayer. Interlinking InGaN strips with GaN troughs between them can be seen; (b) CL image of an InGaN QW which is grown and annealed under the same conditions as the InGaN epilayer. Bright emission from the InGaN strips can be seen; (c) SEM image recorded at the same time with the CL image, showing a lot of V-pits; (d) V-pits observed in (c) are marked on the CL image as white rings. [100]

CHAPTER 4: EXPERIMENTAL DEVELOPMENT AND TECHNIQUES

4.1 General of Laser Light

4.1.1 Introduction

An important method to study the properties of semiconductor materials is luminescence technique. Luminescence is the emission of photons from a substrate not resulting from heat. Chemical reactions, electric current injection to the substrate, mechanical action, or absorption of photons can result in luminescence. In this work, luminescence is generated by absorption of photons (optical excitation); luminescence generated with this method is also called photoluminescence (PL).

Since PL is generated by the optical excitation of the substrate, a light source is necessary. Generally, laser radiation is used as the excitation source, as a result of its high monochromaticity, low beam divergence, and high power density. A laser can be classified into operating in either CW mode or pulsed mode, based on whether its output power is continuous over time or not. In this work, lasers working in both of these two modes were used.

4.1.2 Laser Working in CW Mode

4.1.2.1 Principles of CW Laser

A laser contains a gain medium, an excitation source, and a laser oscillator (also called optical cavity). The gain medium is normally a material of controlled shape, concentration, size, and purity. It can be of any state: gas, liquid, solid, or plasma. The

gain medium is excited by the excitation source, which can be an outside light source or electric field, into an excited state. Under the excitation, atoms in the gain medium reach higher energy states. These excited atoms then return to the ground state by spontaneous emission or stimulated emission. In the latter case, the emitted photons have the same direction, energy, and polarization as the passing by light. When there are more excited atoms in the gain medium than the ground-state atoms, which is called population inversion, there are more photons being generated than being absorbed, and as a result, the light is amplified. The optical cavity reflects the light back into the gain medium for more amplification, so that the light intensity can build up and lasing can be obtained. However, it is possible to obtain lasing with only a single pass of light through the gain medium, and an optical cavity is not needed in this case. As a result, optical cavity is generally required in a laser, but not absolutely necessary.

For CW laser, the output power is constant over time, so a steady excitation source is required to constantly replenish the population inversion of the gain medium.

4.1.2.2 CW Laser Used in This Work

4.1.2.2.1 CW He-Cd Laser Used in This Work

An IK3083R-D He-Cd CW laser, with 325.1-nm output wavelength and about 8-mW output power, was used for ensemble PL measurements, as shown in Figure 4.1. Its beam diameter ($1/e^2$) was 1 mm. The He-Cd laser is a gas laser. The discharge tube contains He gas at a pressure of several Torr, and Cd vapor which is about 1% of He. By transferring energy via Penning ionization from He metastable levels to the Cd upper laser levels, the CW laser is excited [101].
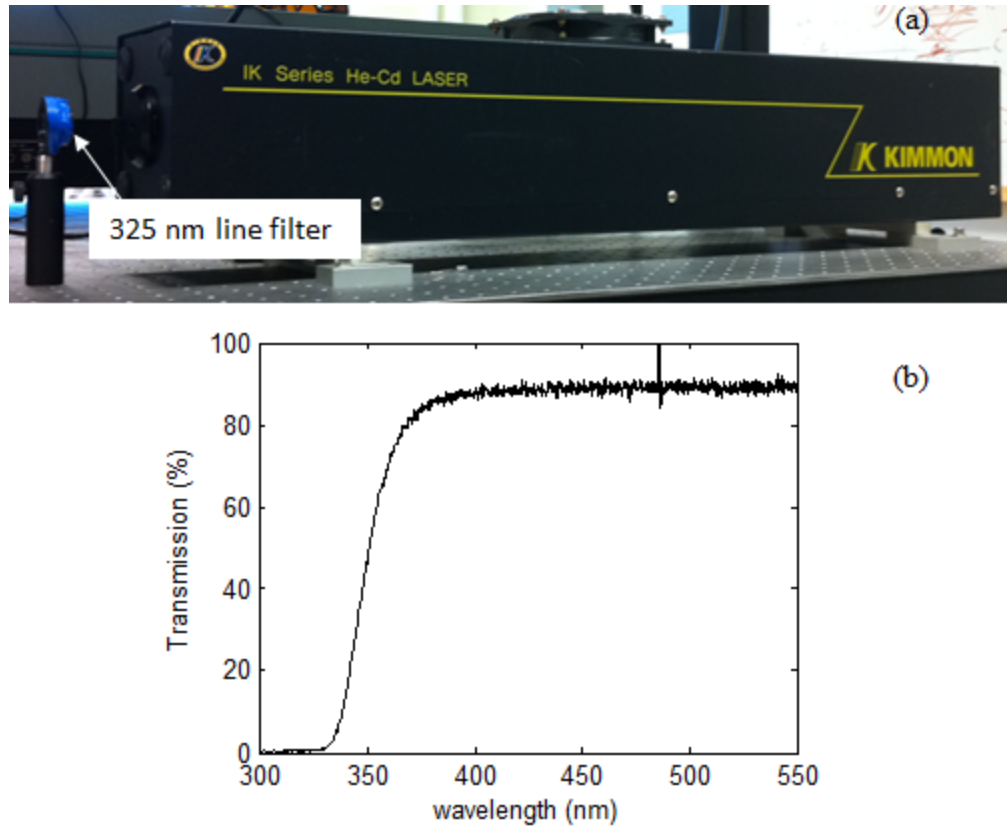
Figure 4.1: (a) Photo of He-Cd laser; (b) the transmission spectra of the line filter and cutoff filter used in the He-Cd laser.

4.1.2.2.2 CW Semiconductor Laser Used in This Work

A COHERENT Verdi G10 laser, with 532-nm output wavelength and 10-W output power, was used as excitation source for temperature dependent PL measurements. Its beam diameter ($1/e^2$) was 2.25 mm [102]. This is an optically pumped semiconductor laser, whose gain medium is a versatile and robust semiconductor chip. Because of the very thin gain medium, the thermal lensing issues are suppressed so that without affecting beam parameters, laser output power can be changed. Moreover, the "green noise" problem is removed by the short upper-state lifetime of the optically pumped semiconductor chip. The "green noise" is the noise generated by sum frequency in multi-longitudinal mode diode pumped solid state lasers.

The output laser beam from the COHERENT Verdi G10 laser was coupled into a COHERENT Mira 900 modelocked Ti:sapphire laser system, with which the laser beam wavelength can be tuned from 710 nm to 1000 nm [103]. During the measurements the wavelength was set to 800 nm.

The 800-nm laser beam was frequency doubled to 400-nm laser beam by a COHERENT second harmonic generator [104]. The output power was 430 mW.

The setup of this COHERENT laser system is shown in Figure 4.2.
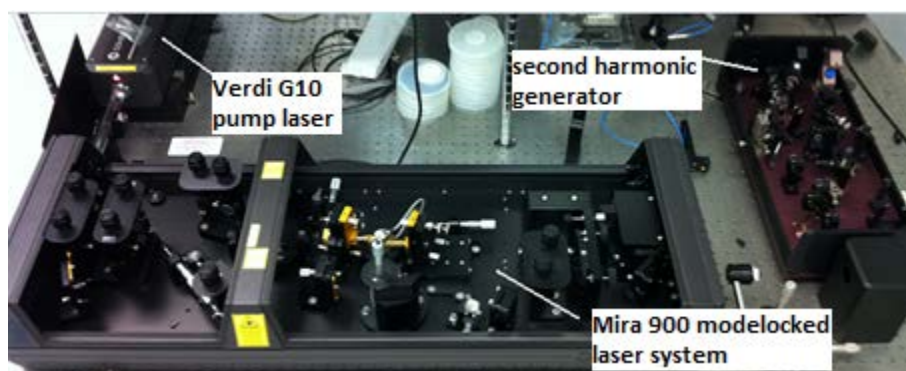
Figure 4.2: Photo of COHERENT semiconductor laser system.

4.1.3 Laser Working in Pulsed Mode

4.1.3.1 Principles of Ultrafast Pulse Generation

A problem of the PL excited by CW laser is that it can only provide time-integrated information of the electronic processes in the substrate. However, since in this study many electronic processes that occur in semiconductors take place in a very short time scale (nanoseconds to microseconds), a ultrafast method is necessary to resolve short-duration processes. In this case, ultrafast laser pulses in the picoseconds range are necessary to excite PL from substrate for time-resolved study.

One method to generate short laser pulses is Q-switching, which is achieved by putting a variable attenuator in the laser's optical resonator [101]. The variable attenuator is also called "Q-switch", and a low Q factor corresponds to high attenuation, which means low resonator loss per roundtrip.

At the beginning when the Q-switch is set to low Q factor (high attenuation), the laser gain medium is pumped, which produces a population inversion by preventing light-feedback into the gain medium. However, since there is no feedback from the resonator, laser operation cannot occur. In this case, as the medium is pumped, energy stored in the gain medium increases. As a result of the loss from processes like spontaneous emission, the stored energy reaches its maximum value. At this moment, Q-switch is tuned from low Q factor to high Q factor (low attenuation); so that the feedback from the resonator into the gain medium is allowed, stimulated-emission-generated optical amplification begins, and laser is generated. Since in the gain medium a lot of energy has already been stored, in the resonator the laser light intensity builds up quickly, and also in the gain medium the stored energy is consumed quickly, both of which result in a short laser pulse with high peak intensity.

Based on how the Q-switch is controlled, Q-switching can be classified into two kinds: active Q-switching and passive Q-switching.

For active Q-switching, the Q-switch is a variable attenuator that is externally controlled. It could be a mechanical device such as a shutter, or it could be a modulator such as an acousto-optic device. In this case, the change of the Q factor, or attenuation, is achieved by an external trigger, which means that the laser pulse rate can be controlled by external trigger.

For passive Q-switching, the Q-switch is a saturable absorber, whose light absorption decreases with increasing light intensity. When the energy stored in gain medium is low, the absorber has high absorption, which means a high attenuation in the resonator. As the stored energy increases, the absorber saturates and its absorption decreases, so the stored energy increases even faster. The absorber ends up with very low absorption so that laser pulse with high power is extracted from the energy stored in the gain medium. After the pulse, as the stored energy in the gain medium decreases, the absorber returns to its high absorption state. So the next laser pulse is delayed until the energy stored in the gain medium rebuilds to high value.

Q-switching can generate laser pulses with very high pulse energy. However, pulses produced by Q-switching have a minimum pulse length of several nanoseconds, which is too long to characterize some nanosecond-scale or picosecond-scale electronic processes.

Mode-locking is a method that is used to generate laser with super short laser pulses. Generally, the laser frequencies that a laser cavity can generate are determined by two factors. First, as the laser resonant cavity is a Fabry-Perot cavity structure that consists of two mirrors facing each other, only light waves with certain frequencies can interfere constructively and form standing waves when bouncing in the cavity, while light waves with other frequencies are suppressed by destructive interference. The light waves with these frequencies are called longitudinal modes, and their frequencies can be calculated as

$$v = \frac{mc}{2nL}, \quad (4.1)$$

where *L* is the cavity length, *n* is the medium refractive index in the cavity, *c* is the speed of light, and *m* is an integer. From Equation (4.1) it is seen that the longitudinal modes have discrete frequencies with a constant interval of

$$\Delta v = \frac{c}{2nL}. \tag{4.2}$$

Second, the gain medium in the cavity has its gain bandwidth. Only the longitudinal modes whose frequencies fall into the gain bandwidth and have roundtrip gain larger than the loss and can build laser emission. These longitudinal modes are the emission frequencies that a laser cavity can really generate and are called cavity modes, and their quantity can vary between several and 10^5 for different kinds of lasers devices. Generally, all these cavity modes are independent, with no fixed phase relationship between them. As a result, the total laser output, which equals to the sum of all the cavity modes, has random intensity fluctuations with time. In this case, the more the cavity modes are, the smaller the random intensity fluctuations are. However, if the cavity modes have a fixed phase relationship between each other, their sum will not show random intensity fluctuations. Instead, their sum will produce narrow pulses periodic distributed in time with same shape and intensity minimum in between. This condition is called mode lock. And the more the mode-locked cavity modes are, the sharper the output pulses are and the smaller the intensity between pulses is.

Mode-locking can be classified as active or passive mode-locking, based on how it's achieved.

Active mode-locking is generally achieved by introducing an external signal to modulate the light in the cavity. One way of doing this is called amplitude modulation (AM), by putting a shutter in the cavity [101]. If the shutter is modulated to open at a rate

that equals to the roundtrip rate, a single pulse of light can be reflected back and forth in the cavity. An acousto-optic intensity modulator is usually used as the shutter. A RF (radio frequency) signal (typically 25–50 MHz) is applied to the modulator, causing a periodic loss within the modulator. When the RF signal is zero, the loss is not present and the shutter is "open", the mode phases are locked and the short pulse passes through the shutter. In addition to AM method, frequency modulation (FM), which is based on an electro-optic frequency modulator, is also used for active mode-locking. This modulator may introduce a sinusoidally varying frequency shift to the light passing through it. If the modulation frequency equals to the roundtrip rate of light in the cavity, the light frequency will shift either up or down. Eventually, the upshift and downshift light will leave the gain bandwidth, leaving only the light which is unaffected by the frequency modulator in the gain bandwidth. As a result, a narrow laser pulse is generated. A third method to achieve active mode-locking is synchronous mode-locking, which is achieved by modulating the pump source so that the laser is effectively turned on and off and produces pulses.

In contrary to active mode-locking, the passive mode-locking technique does not need external modulation signal. Instead, it uses the light in the cavity, along with some devices in the cavity to achieve mode-locking. One method to achieve passive mode-locking is to insert a saturable absorber into the laser cavity. As was mentioned before, the absorption of saturable absorber decreases with increasing light intensity. In this case, the low intensity light will be attenuated by the saturable absorber, while the randomly distributed intensity peaks can pass through the absorber and oscillate in the cavity. As a result, an array of pulses and mode-locking are achieved. Another way of passive mode-

locking, which is also called self-mode-locking or Kerr lens mode-locking, is achieved by using a nonlinear amplifying medium whose refractive index is positively proportional to the light intensity [105]. Based on the Kerr effect, refraction is stronger on the axis of the beam than away from it [106]. As a result, the amplifying medium can focus the light beam. Since the refractive index is larger for light with higher intensity, the focusing effect is stronger for light with higher intensity, which means that high-intensity beams are smaller in diameter than low intensity beams. Low intensity beams can be blocked by carefully arranging an aperture in the laser cavity, leaving only the high intensity pulse.

Unfortunately, the mode-locking laser system is usually very complicated, which means that it takes a lot of efforts to maintain the system and re-align the system once it's misaligned. Moreover, the mode lock laser system is very expensive.

4.1.3.2 Semiconductor LDs Working in Pulsed Mode

LDs are lasers whose gain medium is semiconductor material. Most LDs are formed from p-n junction, through which carriers (electrons and holes) are injected into active region to achieve population inversion for stimulated emission [107]. The depletion region is seen as the gain medium for LDs, and Fabry-Perot cavity is usually used as resonant cavity.

When a LD is electrically forward biased, holes and electrons are injected into the gain medium through p-type region and n-type region, respectively. At the beginning, since there is no photon whose energy equals to the recombination energy in the gain medium, electrons and hole may coexist for a while and then recombine spontaneous. This spontaneous emission is the key factor to initiate laser oscillation. The photons generated by spontaneous emission can then cause recombination by stimulated emission,

generating another photon with the same polarization, phase, frequency, and propagation direction. As a result, the stimulated emission leads to gain in the intensity for light that has the correct wavelength, and the gain increases with the increasing of the number of carrier injected into junction. The gain medium is usually sandwiched between two sets of light-guiding layers and cladding layers above and below it, to form a cavity so that the light is confined to a relatively narrow layer. The two sidewalls of the gain medium are polished to parallel smooth surface, so that a Fabry-Perot cavity is formed. In this case, all the elements that are required for lasing are achieved. Photons that are emitted by electron-hole recombination and fit longitudinal mode of the cavity will travel in the gain medium, being confined by the light-guiding layers and cladding layers and reflected by the smooth sidewalls before they are emitted. As photons propagating in the cavity, their amount will increase as a result of stimulated emission. If photons which are generated due to stimulated emission are greater in amount than photon which are lost due to absorption or incomplete reflection, laser is built up in the diodes.

It should be noted that as a result of the working scheme of the laser diodes, their output laser wavelength is not just a function of the allowed longitudinal mode of the cavity and gain bandwidth of the gain medium. It is also determined by the bandgap energy of the gain medium which is semiconductor material.

Since the gain medium is usually very thin, the light is confined in a very thin layer in the vertical direction. So in the vertical direction there is only one single optical mode. In the transverse direction, if the cavity is much wider than the light wavelength, multi-transverse optical modes exist. Laser generated in this case is called "multi-mode". However, if the cavity width is comparable to the light wavelength, only a single

transverse mode exists and the laser generated in this case is called "single-mode". Generally, multi-mode laser has larger power comparing with single-mode laser, but the diffraction of single-mode laser is relatively smaller than that of the multi-mode laser, which makes single-mode laser smaller beam diameter and divergence. However, due to the small size of laser diodes, the diffraction is very strong, as a result, both modes have very large divergence angle (up to 50°), which means the output beam expands rapidly after emitted from the diode [107].

As has been mentioned above, the gain of laser diodes is determined by the amount of electrons and holes injected into the depletion region, which means that the gain can be controlled through electrically forward bias. In this case, if the forward bias is very small, the gain in the cavity is smaller than the loss, so laser cannot be built, and only light generated by spontaneous emission is emitted from the LDs. On the other hand, if the forward bias is larger than a threshold, the roundtrip gain is larger than the loss in the cavity, and laser is built and emitted. Moreover, laser diodes can work in both CW mode and pulsed mode by controlling the gain, or to say, the forward bias. If a constant forward bias is applied and the forward bias is large enough, the diodes have constant gain which is larger than the loss, as a result, the laser diodes work in CW mode. However, if the forward bias is modulated to turn the gain on and off, the laser is then turned on and off to generate pulses. In this case, laser diodes work in pulsed mode. And this method of generating laser pulses is called synchronous mode-locking [108], as has been introduced above.

Laser diodes have the advantages of low cost, low energy consumption and small size. They can be made into very small size to compact into integrated circuits. If

working in pulsed mode, the pulse length can be as short as 50 picoseconds. And also, the fact that laser diodes can easily achieve pulsed mode by modulating their forward bias benefits this research here.

MQW laser diodes are the laser diodes whose gain medium is made of multi-quantum wells. As a result of quantized density of states and limited number of dimensions that carriers can move, MQW laser diodes have higher efficiency than a bulk laser diode does [109].

Figure 4.3 shows the general structure of MQW LDs. The whole structure is grown on *c*-plane sapphire substrate with a GaN buffer layer. Carriers are injected through n-GaN and p-GaN with n-electrode and p-electrode on it, respectively. The n-$In_{0.1}Ga_{0.9}N$ layer also works as a buffer layer for the following thick n-$Al_{0.15}Ga_{0.85}N$ layer growth to prevent cracking of the layer. The p-$Al_{0.2}Ga_{0.8}N$ layer is used to prevent InGaN QW layers from dissociating during the growth of p-GaN layer. The QW active layers are sandwiched between a pair of n-GaN and p-GaN, and then a pair of n-$Al_{0.15}Ga_{0.85}N$ and p-$Al_{0.15}Ga_{0.85}N$. This is because the QW active layers are not good at effectively confining the light as a result of their small thickness. In this case, n-GaN and p-GaN layers are used as light-guiding layers, and n-$Al_{0.15}Ga_{0.85}N$ and p-$Al_{0.15}Ga_{0.85}N$ are used as cladding layers since they have lower refractive index, so that a cavity is formed and the light emitted from the active region are confined. In Figure 4.3, the left and right sidewalls are cleaved and polished to smooth surface using RIE (reactive ion etching), so that a Fabry-Perot cavity is formed. In order to increase the reflectivity of the sidewalls, high reflection facet coating is generally applied on them.
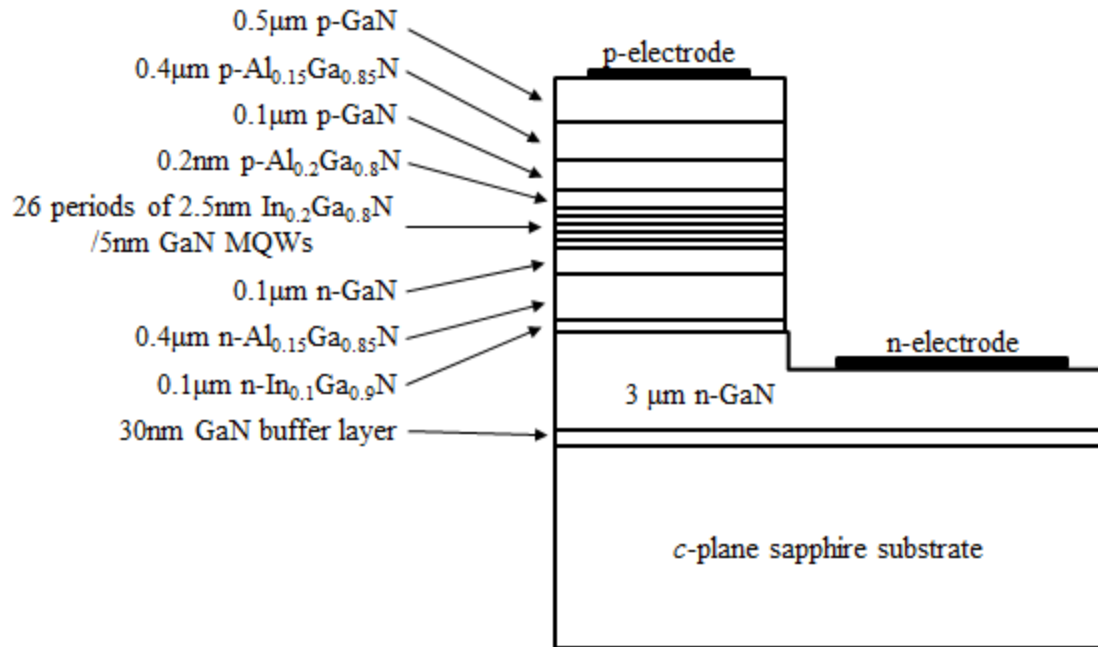
Figure 4.3: Structure of an InGaN MQWs laser diode [107].

Because of the strong diffraction effect, the output beam diverges rapidly after emitted from the diode. Since the thickness of the active layers is much smaller than their width, the divergence in vertical direction is much larger than that in transverse direction. As a result, MQW LDs have elliptical far field pattern, as shown in Figure 4.4. If a collimated beam is needed, a lens must be used.
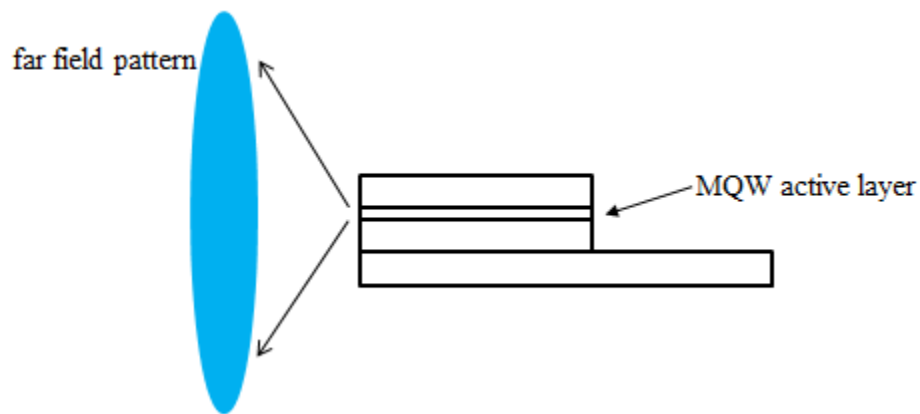
Figure 4.4: Far field pattern of MQW LD [107].

4.1.3.3 Pulsed Laser Used in This Work

4.1.3.3.2 Pulsed Nd:YAG Laser Used in This Work

Nd:YAG lasers are solid-state lasers that use Nd:YAG crystals as gain medium. The Nd:YAG crystal is Nd doped YAG, in which a small portion of yttrium is replaced with Nd. Nd:YAG lasers generally use flashtube or laser diodes as excitation source. The output wavelength of Nd:YAG lasers is typically 1064 nm, which can also be frequency doubled into 532 nm or frequency tripled into 355 nm. Nd:YAG lasers can operate in both pulsed and CW modes, with higher Nd concentration being used for pulsed mode and lower Nd concentration being suitable for CW mode. The pulsed mode is achieved by active Q-switching: an optical switch is inserted into the laser cavity and opens until the Nd ions reaches maximum population inversion.

The CONTINUUM Nd:YAG laser used in this work was used in pulsed mode as it has higher output power. Its output was frequency doubled into 532 nm, and its output energy was set to 0.5 J, with 10 Hz repetition frequency and 2 ns pulse width (duty cycle 2×10^{-6}%).

The output laser beam from Nd:YAG laser was coupled into a LaserVision OPO/OPA (optical parametric oscillator/optical parametric amplifier) system. The OPO is an oscillator that oscillates at optical frequencies. It contains a nonlinear optical crystal and an optical resonator. Through second order nonlinear optical interaction, the nonlinear optical crystal converts an input laser beam (the "pump") with frequency ω_p into two output beams (the "signal" and the "idler") of lower frequency ω_s and ω_i. The sum of the output beams' frequencies equals to the input beam frequency: $\omega_s + \omega_i = \omega_p$. The optical resonator serves for the resonation of signal beam, or idler beam, or both, so the

intensity of the output beam(s) can build up quickly. It is possible to change the output frequencies by changing the phase-matching or quasi-phase-matching properties of the nonlinear optical crystal. The OPA is a light source that can emit light with variable wavelengths by an optical parametric amplification process. After the signal beam being separated from the OPO output, the idler beam, collinearly with the beam which has the same frequency as the pump, goes through a nonlinear optical crystal. And at the output of OPA a stronger output which has the same frequencies as the signal and idler is acquired.
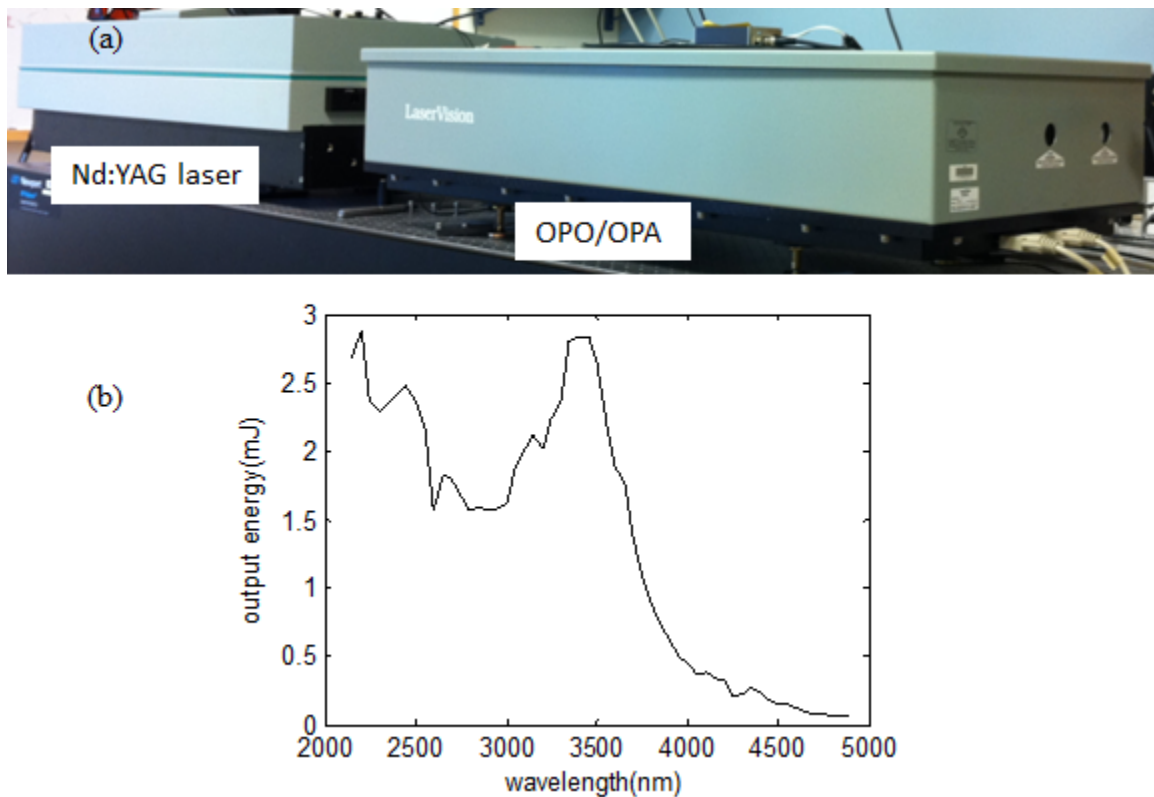
Figure 4.5: (a) Photo of Nd:YAG pumped OPO/OPA system; (b) output energy spectrum of the system.

In this work, the output laser beam of OPO/OPA system was tunable from 700 nm to 5000 nm, with 700 nm to 1300 nm of near IR, 1300 nm to 2100 nm of intermediate

IR, and 2100 nm to 5000 nm of mid IR. The output energy spectrum in mid IR is shown in Figure 4.5, measured with an OPHIR energy meter.

4.1.3.3.2 Pulsed LD Used in This Work

A LDH-P-C-405 PicoQuant semiconductor laser diode was used as pulsed laser. The laser system consisted of a laser head and a pulsed diode laser driver. The output wavelength was 402 nm. The output pulse repetition frequency was tunable between 10 MHz and 80 MHz. The average output power was tunable with 0~0.27 mW for 5 MHz, 0~0.5 mW for 10 MHz, 0~0.94 mW for 20 MHz, 0~1.9 mW for 40 MHz, and 0~4.3 mW for 80 MHz. The pulse width could be as short as 49 ps. Even though the pulse width could not be controlled directly, it depended on the laser output power. Figure 4.6 shows output power dependent laser beam shape for the laser diode operating at 40 MHz repetition frequency. By changing the laser output power, different pulse shape/width is generated. It is seen that symmetrical and clean pulses can be achieved at low output power, while with increasing power the pulse becomes broader, showing shoulder or additional peaks.

In this work, the laser diode was set to 10 MHz repetition frequency, with output pulse width ~300 ps, corresponding to 0.3% duty cycle. The output power, after traveling through a 1-m-long optical fiber, was 0.4 µW.
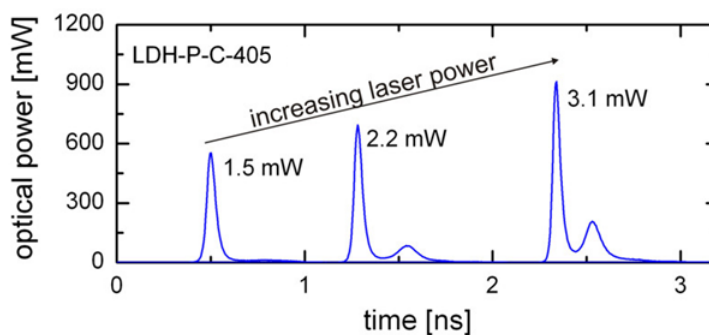
Figure 4.6: Power dependent laser beam shape [110].

4.2 Temperature-dependent PL

4.2.1 Introduction

Generally PL spectroscopy is measured at room temperature. However, since at low temperatures few carriers are thermal activated, semiconductor materials show properties that are different from at room temperature. As a result, it is very important to measure PL at low temperatures. Liquid N_2 and helium compressor are two methods that are usually used for reaching low temperatures: N_2 for 77 K and helium compressor for 4 K. In this work a low temperature PL system based on helium compressor was used.

4.2.2 Low Temperature PL System

A home-built low temperature PL system was used to analyze the temperature dependent PL properties of blue-emitting InGaN/GaN MQWs. The system is available in Characterization Lab, at Veeco Instruments Inc. Figure 4.7 shows the schematic diagram and the photo of this system.

The CW Verdi G10 semiconductor laser pumped laser system, which was introduced in Section 4.1.2.2.2, was used as excitation source. The 400-nm laser beam generated by the system was coupled into a single mode optical fiber, after which an optical lens was placed to focus the laser light into a 2-mm-diameter spot on the sample.

PL light from sample was first collected by a collimated lens, and then focused by another lens onto monochromator after which a Si detector was placed. Using thermal grease, the sample was mounted on a cold finger in a Cryo-head, which was connected with a vacuum pump, a Helium compressor and a temperature controller, so that temperature between 10 K and 300 K can be reached [111]. An Agilent 3631A power supply was connected to the sample if there were metal contacts on the sample, so that the system was also capable of measuring EL spectrum and IV (current-voltage) curve at different temperatures. A computer was connected to the system, and a Labview program was written to control the temperature controller, the power supply and the monochromator, and to acquire data from Si detector, so that the PL, EL, and IV spectrum can be taken at a couple of pre-set temperatures automatically. The user interface of the Labview program is shown in Figure 4.8.
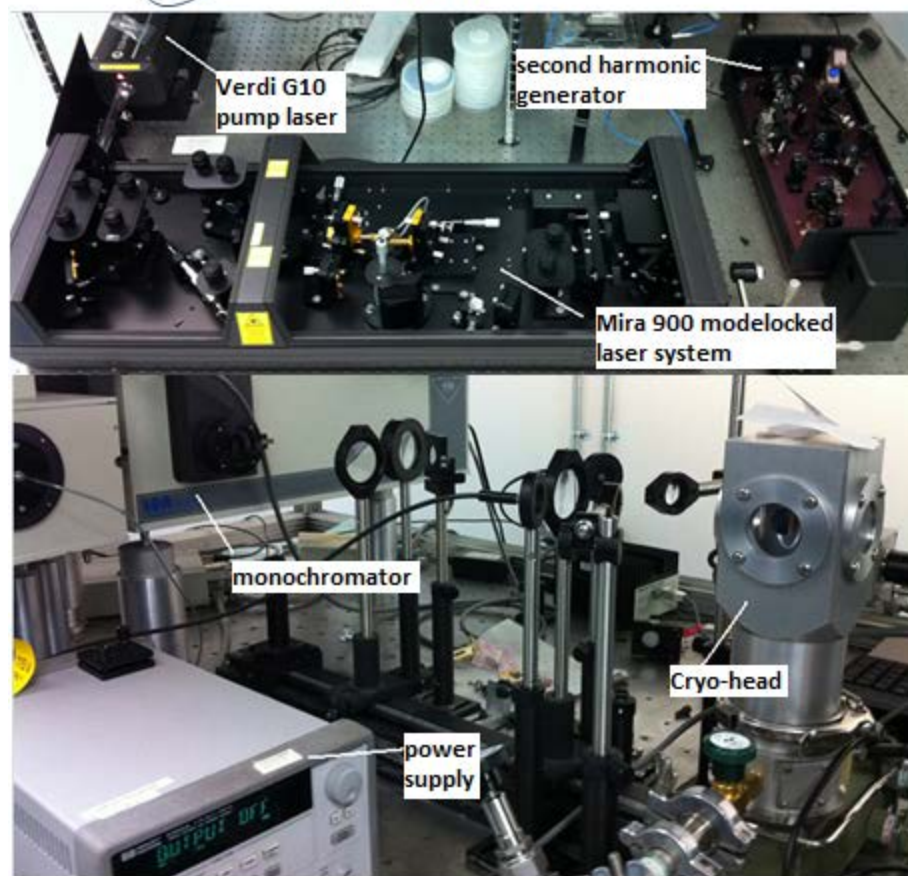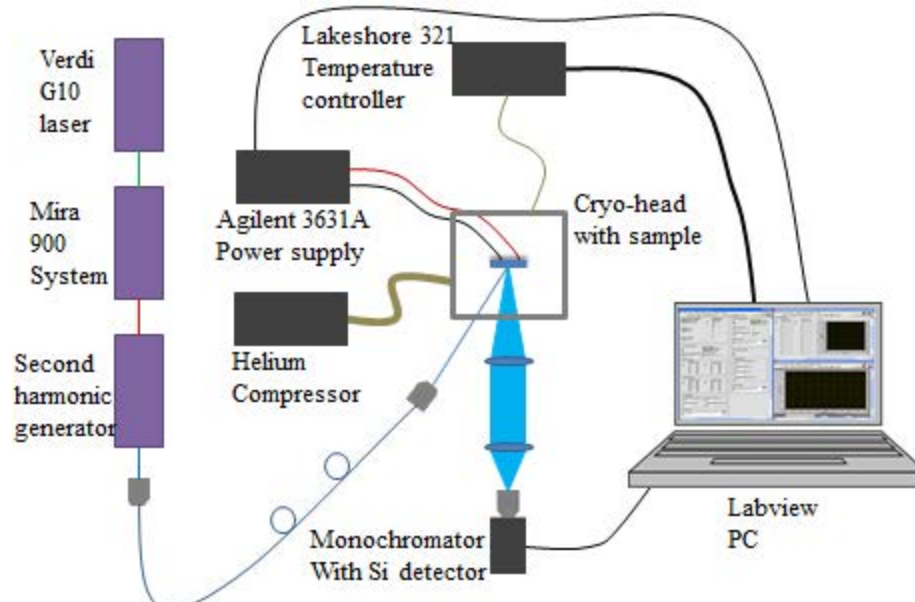
Figure 4.7: (Color) Schematic diagram and photo of low temperature PL system.
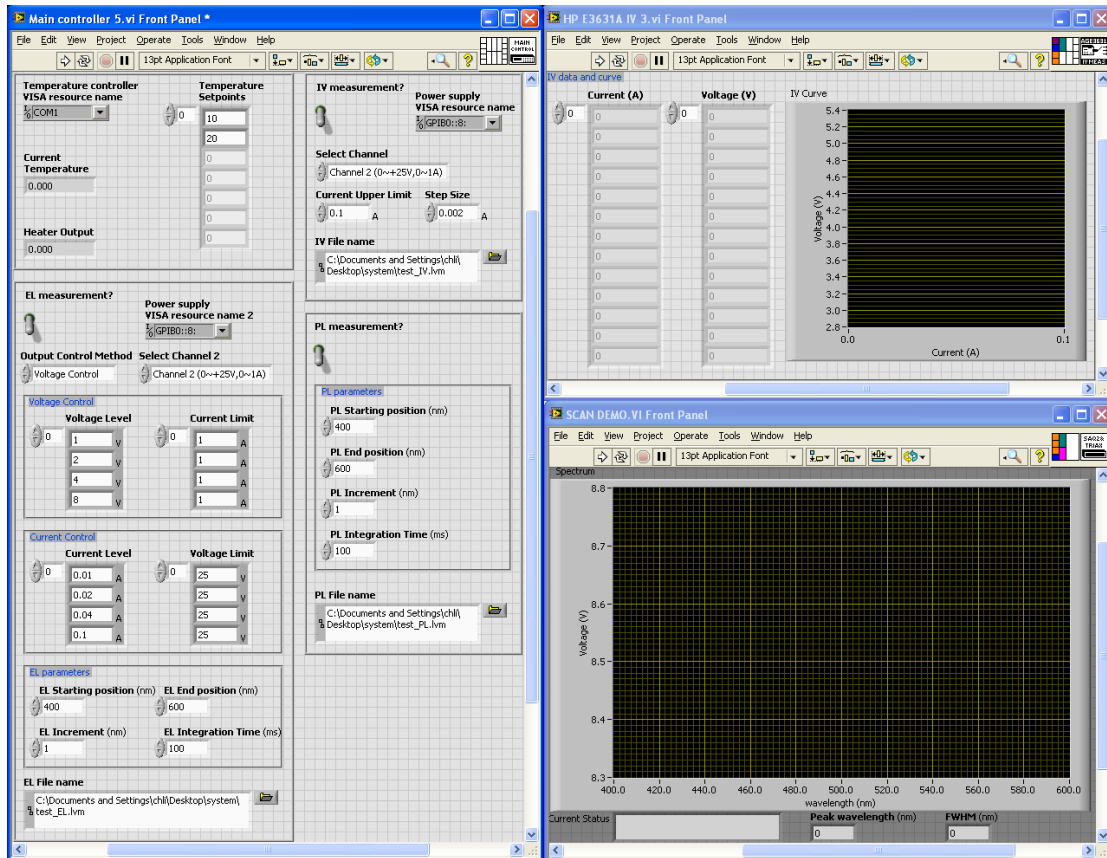
Figure 4.8: User interface of the Labview program that controls the low temperature PL/EL/IV system.

4.3 Confocal Microscopy

4.3.1 Introduction

The use of PL spectroscopy to study the properties of semiconductor materials was discussed before. Generally, people are interested in measuring PL spectrum for a large scale (ensemble PL). However, there are some situations in which PL spectrum in nanometer scale or micrometer scale is needed, for example, to measure the PL inhomogeneities in InGaN MQWs. In this case, direct excitation from He-Cd gas laser or InGaN laser diode is not enough since the output beam of them is millimeters in diameter, and methods need to be found to focus the laser beam into nanometer or micrometer scale.

Confocal microscopy and NSOM are two methods that are used for measuring nanometer- or micrometer-scale PL, and confocal microscopy was used in this work.

4.3.2 Working Scheme of Confocal Microscopy

Confocal microscopy is an optical imaging technique. By using point illumination and a pinhole to get rid of off-focus light, it can reach high resolution and high contrast imaging. Confocal microscopy is depth sensitive, which means that it is able to acquire images from selected depth in the sample. Based on their working scheme, confocal microscopes can be classified into three different types: CLSM, spinning-disk confocal microscopes, and programmable array microscopes. In this research CLSM was used, so here CLSM will be mainly introduced.

In a CLSM, a laser beam is reflected by a DBS (dichroic beam splitter) first and then focused by an objective lens into a focal point within or on the surface of a sample. Electrons and holes are generated under this laser excitation. These electrons and holes may recombine at the focal point and generate fluorescence light, or they may recombine after diffusing out of the focal point and generate fluorescence light, as shown in Figure 4.9. Fluorescence light, along with scattered and reflected laser light, is collected by the very same objective lens and then passes through the DBS. The DBS is chosen so that the laser beam, which is at relative shorter wavelength, cannot pass the DBS, while the fluorescence light, which is at longer wavelength, can pass the DBS. The passed fluorescence light then goes through a pinhole, which is confocal to the focal point on the sample relative to the objective lens, so that only the fluorescence light generated at focal point can go through while the fluorescence light generated out of the focal volume is blocked totally (Figure 4.9(a)) or mostly (Figure 4.9(b)), in either case, the fluorescence

light cannot contribute to the final imaging. After passing the pinhole, the intensity of the fluorescence light is filtered by a filter to selectively choose the wavelength that would be used for imaging, and then detected by a detector such as PMT (photomultiplier tube) or APD (avalanche photodiode), transforming the light signal into an electrical signal.
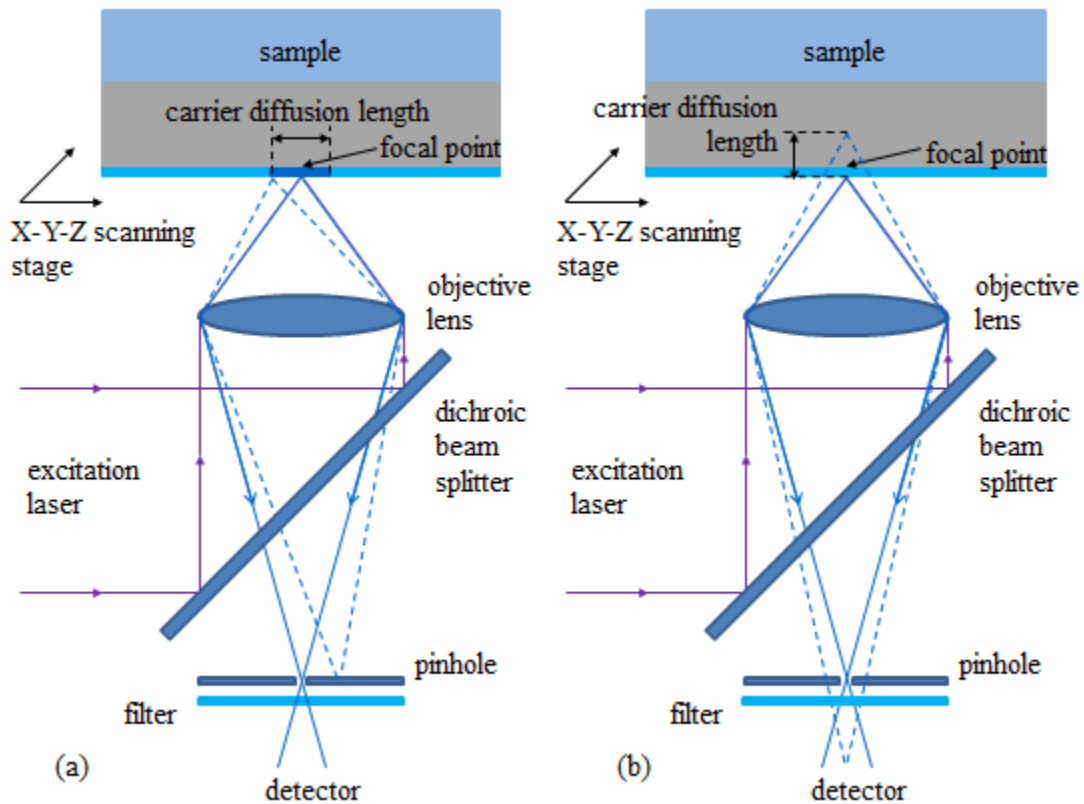
Figure 4.9: Working scheme of confocal laser scanning microscope.

By using the pinhole the out-of-focus fluorescence light is blocked, which can reduce the image size of the focal point and result in sharper images than those from conventional fluorescence microscopy. However, since most of the fluorescence light is blocked at the pinhole, the high resolution is achieved at the cost of low signal intensity; as a result, to get a strong signal and good SNR (signal to noise ratio), long exposure time is required. Another factor that may affect the image size of the focal point is the size of focal volume, as in reality the focal point is not an infinitely small point but a three-

dimensional diffraction pattern, whose size is determined by the numerical aperture of the objective lens and the laser wavelength. Ideally, if optimized objective lens and pinhole are used, the resolution can be as small as half of the excitation laser wavelength.

By using the above mentioned point illumination and pinhole, the fluorescence from the objective lens focal point can be imaged as one pixel, where the brightness of the pixel represents the fluorescence intensity of that point on the sample. When the focused laser beam scans on the sample, a two-dimensional image can be obtained pixel-by-pixel and line-by-line. Usually the scanning rate can be controlled: slow scanning provides a better SNR, resulting in better contrast and high resolution, but have the disadvantage of time-consuming. By adjusting the depth of the focal point in the sample, information can be collected from different focal planes, and then a three-dimensional image of the sample can be generated by assembling all the two-dimensional images for focal planes.

4.3.3 CLSM System Setup

In this work, a home-built CLSM system was used to analyze the submicron-scale PL characteristics of blue-emitting InGaN/GaN MQW samples. The home-built CLSM is available in Room 123, in Grigg Hall, at UNC Charlotte. Figure 4.10 shows the schematic diagram and the photo of this home-built scanning confocal microscope.
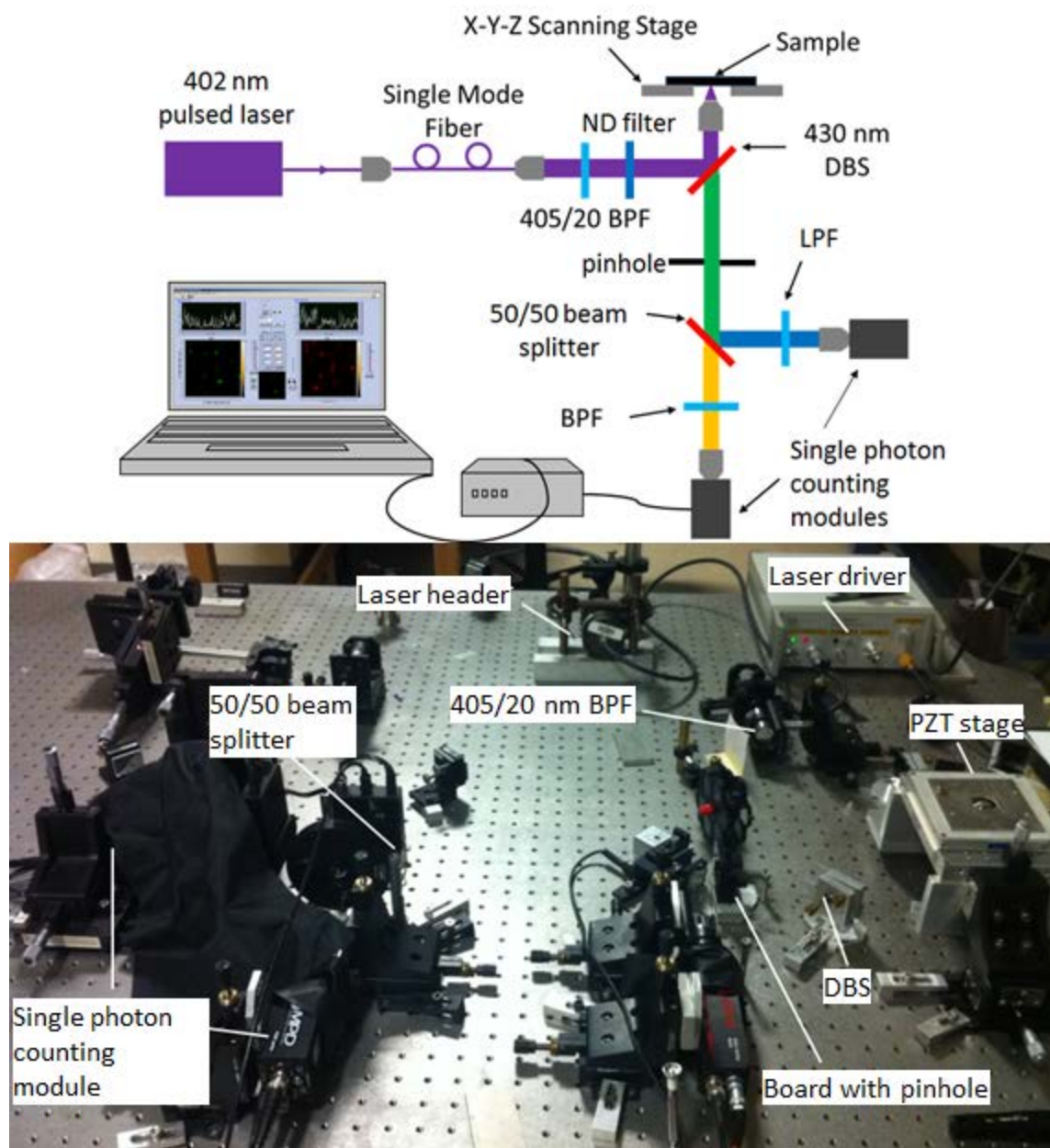
Figure 4.10: Schematic diagram and photo of CLSM system for imaging.

The LD introduced in 4.1.3.3.2 was used as excitation source for the CLSM system. Its output laser beam was coupled into a single mode optical fiber after which a 405/20 nm BPF (band-pass filter) was placed, in order to get rid of the possible luminescence light from the fiber. Although as a result of diffraction, the output laser beam had an elliptical beam shape with dimension of 1.5×3.5 mm (Figure 4.11(a)), after

passing through the single mode optical fiber, the beam became a nice Gaussian profile (Figure 4.11(b)). The laser beam was then reflected by a 430 nm DBS and focused by a 100× objective lens, whose numerical aperture was 1.25, on to the sample. Luminescence light from the sample was collected by the very same objective lens. A board with a pinhole was placed after the DBS, followed by a 50/50 beam splitter. The luminescence light split by the 50/50 beam splitter was detected separately using two EG&G SPCM (single photon counting module). In the experiment, one SPCM was preceded by a BPF to collect the bandedge emission light, depending on the bandgap of the samples, the BPF was chosen from 445/40 nm, 460/20 nm, and 485/20 nm; the other SPCM was preceded by a 538 nm LPF (long-pass filter) to collect the yellow band luminescence light. In this case, two color imaging could be achieved at the same time over the same place. For protection purpose, a ND (neutral density) filter was usually put in between the 450/20 nm BPF and the DBS, in case the laser was too strong to be blocked totally by filters.
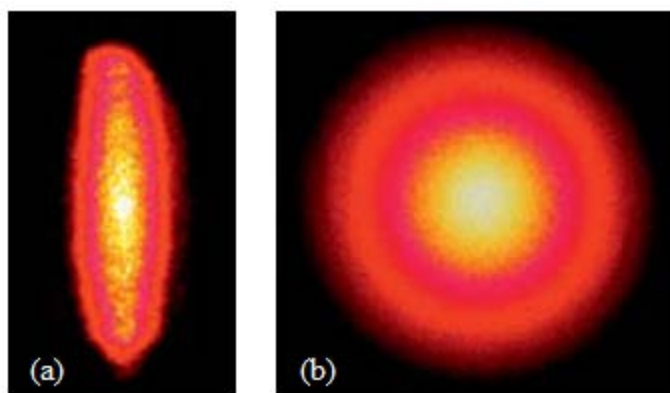
Figure 4.11: Beam shape at the output of LD (a) and optical fiber (b) [110].

In this system, the optical probe was stationary relative the instrument frame, while the sample was mounted upside down to a high speed scanning PZT (lead zirconate titanate) stage with nanometer precision control along three axes and was able to translate

over a range of 50 μm by 50 μm by 30 μm in *x*-, *y*-, and *z*-direction, respectively, at closed loop speeds of 10 Hz [112]. The movement of the stage was controlled by custom LabView software, which also controlled the scanning speed, the scanning area, and the scanning resolution, and recorded all data from SPCMs and plotted the CLSM images.

The system has a lateral spatial resolution of about 200 nm, and vertical spatial resolution of about 100 nm. Localization of molecular-sized features of less than 6 nm, as well as molecular separation of about 2 nm, was possible using deconvolution with the point spread function. Since optical fiber was used in the system, so zeroth order Bessel function was used for the point spread function [112].

For submicron-scale PL spectral measurements, the 50/50 beam splitter, the BPFs, the LPF, and the SPCMs were replaced with spectrometer and thermoelectrically cooled CCD (charge-coupled device) camera, as shown in Figure 4.12(a). For submicron-scale TRPL measurements, the SPCMs were replaced with TCSPC (time-correlated single photon counting) APDs, as shown in Figure 4.12(b).

During the measurements the excitation laser was set to 10 MHz frequency, with ~300 ps pulse width (~0.3% duty cycle). The excitation laser power was set to be 0.4 μW. A 1.7 ND filter was set in front of the DBS to attenuate the laser power. When the laser beam was focused by the 100× objective lens onto the sample 4/5 of its power was lost. So the average laser power injected onto the samples was

$$0.4 \mu W \times 10^{-1.7} \times \frac{1}{5} = 1.6 nW \ .$$

Considering the size of the laser beam when focused onto the sample, the average laser power density was

$$\frac{1.6nW}{\pi \times (100nm)^2} = \frac{1.6 \times 10^{-9} W}{\pi \times (100 \times 10^{-7} cm)^2} = 5.1W / cm^2,$$

corresponding to a mean carrier injection density of $\sim 1 \times 10^{17}$ cm^{-3}. This excitation condition was low enough to avoid sample heating.
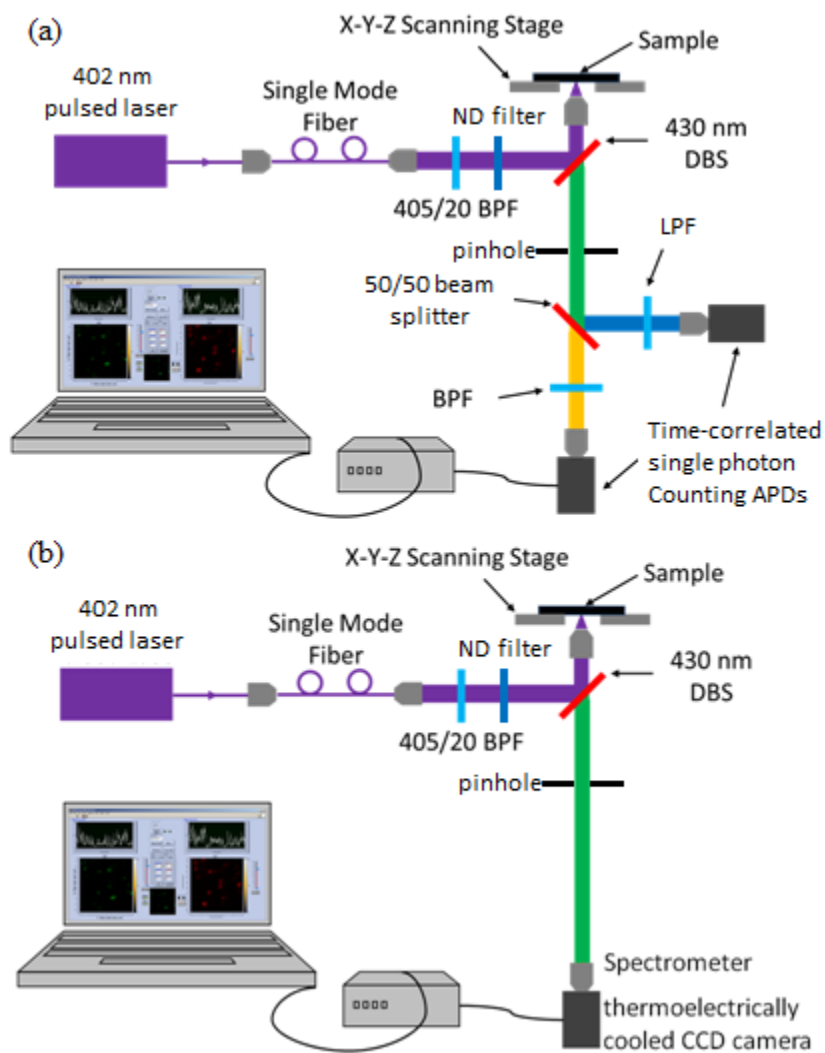
Figure 4.12: Schematic diagram of CLSM system for (a) spectrum measurements and (b) TRPL measurements.

4.4 Time-correlated Single Photon Counting

4.4.1 Introduction

The above mentioned PL is actually time-integrated PL, in which the change of PL with time is not considered. However, TRPL measurement is also very important since it can show the dynamics of short-timescale processes, and as a result show carrier lifetime. TRPL measurements require a pulsed laser source (as the one mentioned in Section 4.1.3.3.2), a fast detector, and fast readout electronics. The detector and readout electronics should be able to operate on the timescale of the interval between laser pulses. In this work, TRPL measurements were done by using TCSPC APDs.

4.4.2 Principle of Time-correlated Single Photon Counting

The basis of TCSPC is the detection of single photons from periodic light signals [113]. By recording how many times individual photons are detected at a certain time after the timer starts, it is able to reconstruct the original time-dependent spectrum indirectly.

TCSPC can be used to measure the carrier lifetime (or carrier recombination rate). Since various carriers in a sample will recombine and emit photons at different times even though they are excited simultaneously, the recombination should be recognized as having a certain rate rather than taking place at a specific time after excitation. In this case, by detecting single photon from a periodic excitation, measuring how long single photon takes to be emitted, and combining all the data points, TCSPC can build an 'intensity vs. time' graph which shows the exponential decay curve typical to these processes.

TCSPC must be done with periodic excitation over a consecutive series of very short time periods. In one period, it is possible to detect one photon, more than one photon, or nothing, in which the probability of detecting one photo is much higher than the probability of the other two. The time delay relative to the pulsed output of the laser used for excitation is measured for each photon. After many photons have been detected, a histogram of the detection time relative to the excitation laser pulse can be built, which is the TRPL spectrum [114]. This measurement process is shown in Figure 4.13.
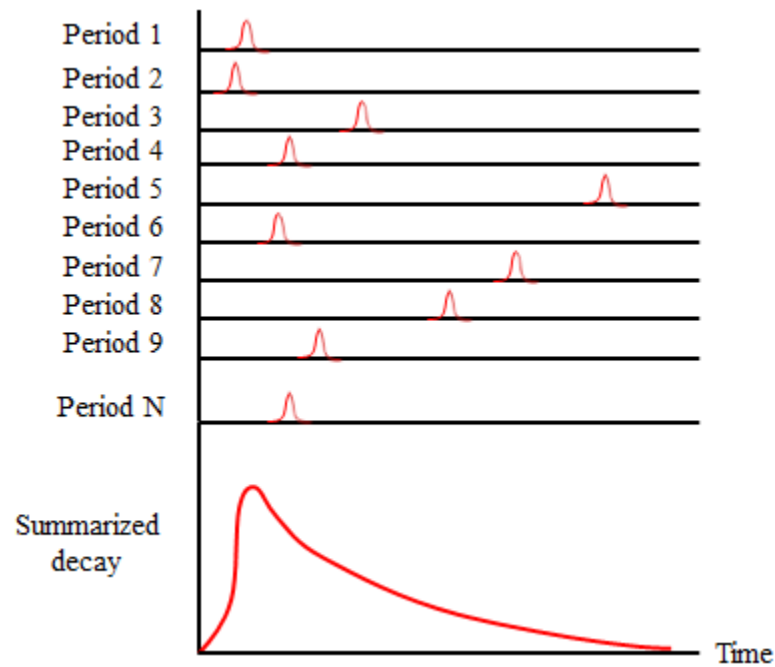
Figure 4.13: Principle of TCSPC.

4.4.3 Device for Time-correlated Single Photon Counting

In this work, a commercial PicoQuant TCSPC system was used for time-resolved measurements. The system contained a high-speed single photon detection module (PDM), which obtained excellent photon detection efficiency and superior time resolution through the use of epitaxial silicon single photon APD. The PDM was

controlled by a 'TimeHarp 200' module which was installed in the card slot of a PC. Synchronization with pulses from the excitation laser diode was achieved using a reverse start-stop mode. The schematic system of the TCSPC system is shown in Figure 4.14.
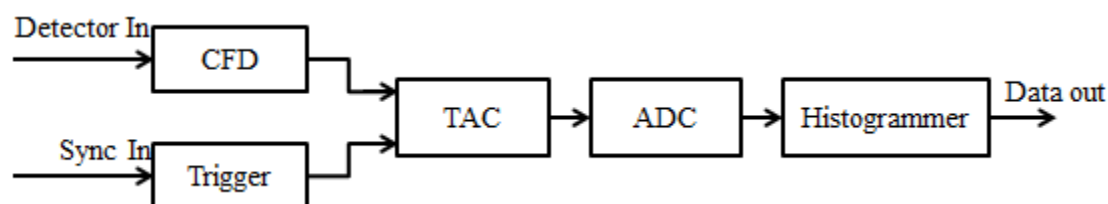
Figure 4.14: Schematic diagram of TCSPC system.

When a photon was detected by the APD, an electrical detector pulse was sent to the constant fraction discriminator (CFD) in the 'TimeHarp 200' module, which then delivered an output pulse synchronized with the temporal position of the detector pulse. The laser driver also sent out electrical SYNC pulses which were synchronized with the output laser pulses. The signals from the CFD and the laser SYNC were fed to the time to amplitude converter (TAC), which transferred the time difference between the two signals into electrical signal with its voltage proportional to the time difference. The TAC signal was fed to the analog to digital converter (ADC), which converted the signal to an address in the computer memory, proportional to the voltage of the signal. When a photon was detected, based on its time difference with excitation pulse, the content of the corresponding addressed memory increases by one. In this case, over time the memory can build a time-resolved curve.

The time-resolution of the TCSPC system in this work is 0.0296 ns.

4.5 Summary and Conclusion

A variety of lasers were utilized during the research, including He-Cd CW laser, semiconductor CW laser, Nd:YAG pulsed laser, and pulsed LD.

A temperature-dependent PL system was built and a Labview program was written to control the system. The system was used to study the temperature dependent PL characteristics of blue-emitting InGaN/GaN MQWs.

In order to study the lateral submicron scale PL distribution of the blue-emitting InGaN/GaN MQWs, the excitation laser beam must be focused down to a very small spot size. A confocal laser scanning microscope was used for PL imaging in submicron scale. With some setup changes, the microscope was also able to be used for PL spectroscopy measurements and TRPL spectroscopy measurements in submicron scale.

The He-Cd CW laser, semiconductor CW laser, Nd:YAG pulsed laser, OPO/OPA system, ultrafast pulsed laser diode, spectrometer, time-correlated single photon counting system used in this work were all standard, commercially available devices.

CHAPTER 5: EXPERIMENT RESULTS AND DISCUSSION

5.1 Low Temperature PL Study

Six InGaN/GaN MQW samples, with the structure mentioned in Section 2.3.2.4, are used for temperature dependent PL study. Figure 5.1 shows the surface morphology images of the samples, taken with AFM. The number of V-pits for each AFM image is counted, from which the density of V-pits is calculated based on equation
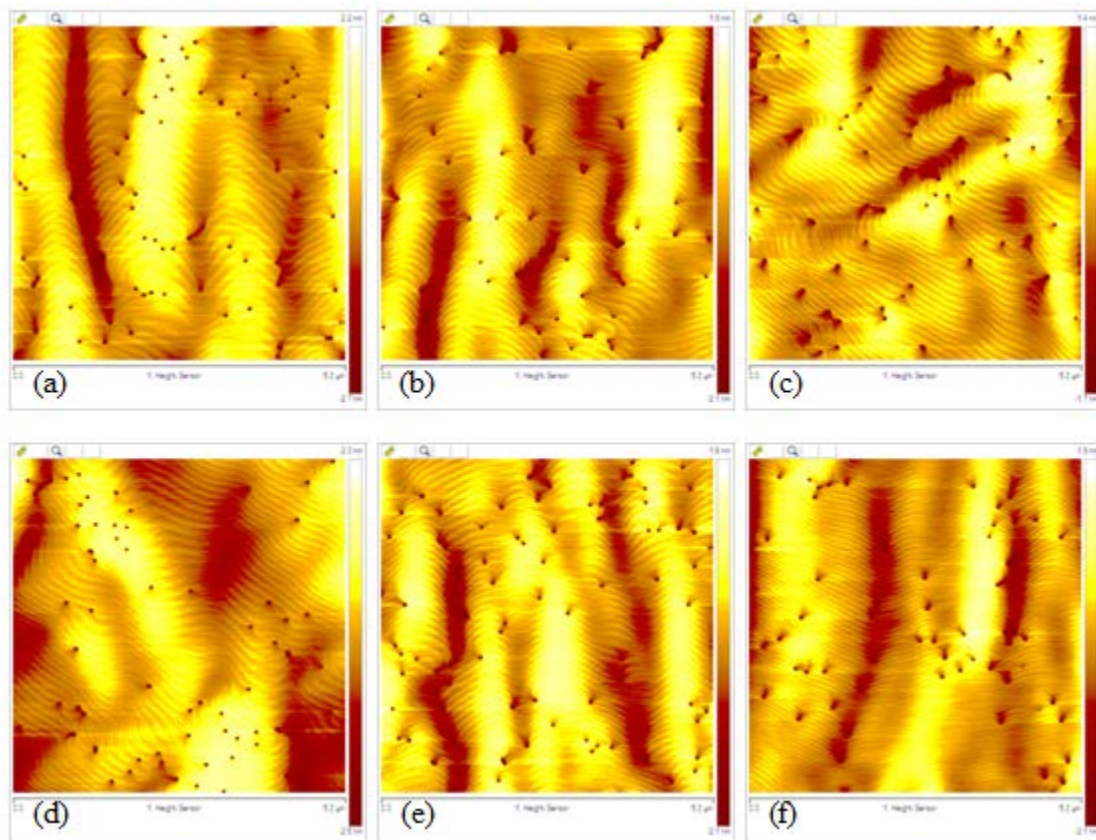
Figure 5.1: AFM images of sample surface for (a) sample #1; (b) sample #2; (c) sample #3; (d) sample #4; (e) sample #5; and (f) sample #6. All images are 5 μm×5 μm.

$$\text{density of V-pits} = \frac{\text{number of V-pits}}{\text{area}}. \qquad (5.1)$$

Table 5.1 lists the density of V-pits. It is seen that all the samples have similar density of V-pits (on the order of 10^8), which agrees with the early statement that all the MQWs have equivalent density of TDs. However, at room temperature, these samples have sample average PL intensity varying by two orders of magnitudes, as shown in Table 5.1. It should be noted that the sample average PL intensity was measured with Nanometrics RPM Vertex, by taking PL spectra with 2 mm step size over the whole sample surface, and calculating the mean value of the peak intensities of all the points. In Figure 5.2, sample average PL intensity is plotted as a function of the density of V-pits, from which a random distribution can be seen, indicating that the sample average PL intensity is independent of density of V-pits. This means that there must be some schemes other than V-pits that is responsible for the variation of PL intensity.
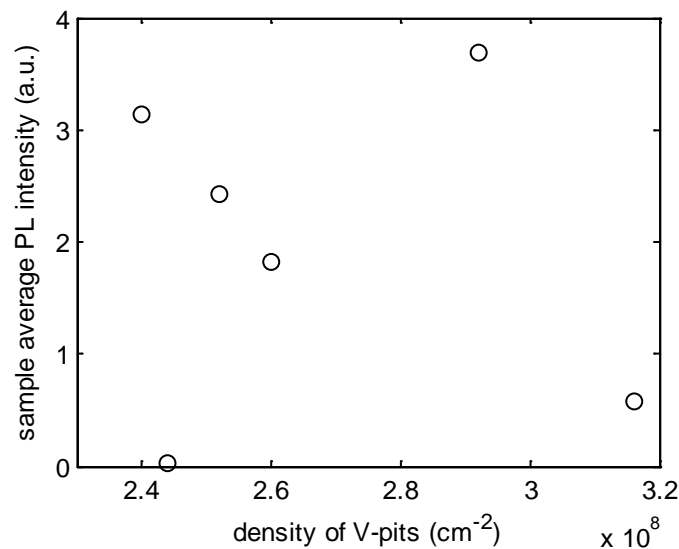
Figure 5.2 Density of v-pits vs. sample average PL intensity.

Table 5.1: Basic parameters for samples used in temperature dependent PL study

sample ID	#1	#2	#3	#4	#5	#6
PL peak wavelength @300K (nm)	442.8	445	446.4	457	450.8	456
sample average PL intensity (a.u.)	3.69	3.13	2.428	1.815	0.581	0.033
Number of v-pits	73	60	63	65	79	61
Density of v-pits (cm^{-2})	2.92e8	2.4e8	2.52e8	2.6e8	3.16e8	2.44e8
Spectrum-integrated PL intensity @10K	13914	18155	16825	11022	11497	10093
Spectrum-integrated PL intensity @300K	3214	4615	2902	1244	1082	282
IQE	0.2309	0.2546	0.1724	0.1129	0.0942	0.028
Rate constant A	15.6	10.8	36.5	36.5	26	150.9
Activation energy E_A (meV)	44.4	46.1	54.5	40.1	30.1	33.1
Rate constant B	1.3	1.9	1.4	0.7	1.1	2.9
Activation energy E_B (meV)	11.3	13	11.2	7	6.5	8.3

5.1.1 Temperature-dependent PL and Spectrum-integrated PL Intensity

PL spectra for each sample are measured from 10 K to 300 K with 10 K step size when temperature is below 140 K, 20 K step size when temperature is between 140 K and 200 K, and 50 K size when temperature is above 200K.

Figure 5.3 shows the PL spectra for each sample at several different temperatures. The low energy shoulders are attributed to longitudinal optical phonon replicas of the main recombination peak. The high energy should does not appear until temperature is higher than 100 K, indicating that it is attributed to the carrier recombination at higher energy levels since the carriers are thermal activated to the higher energy levels at increased temperature.
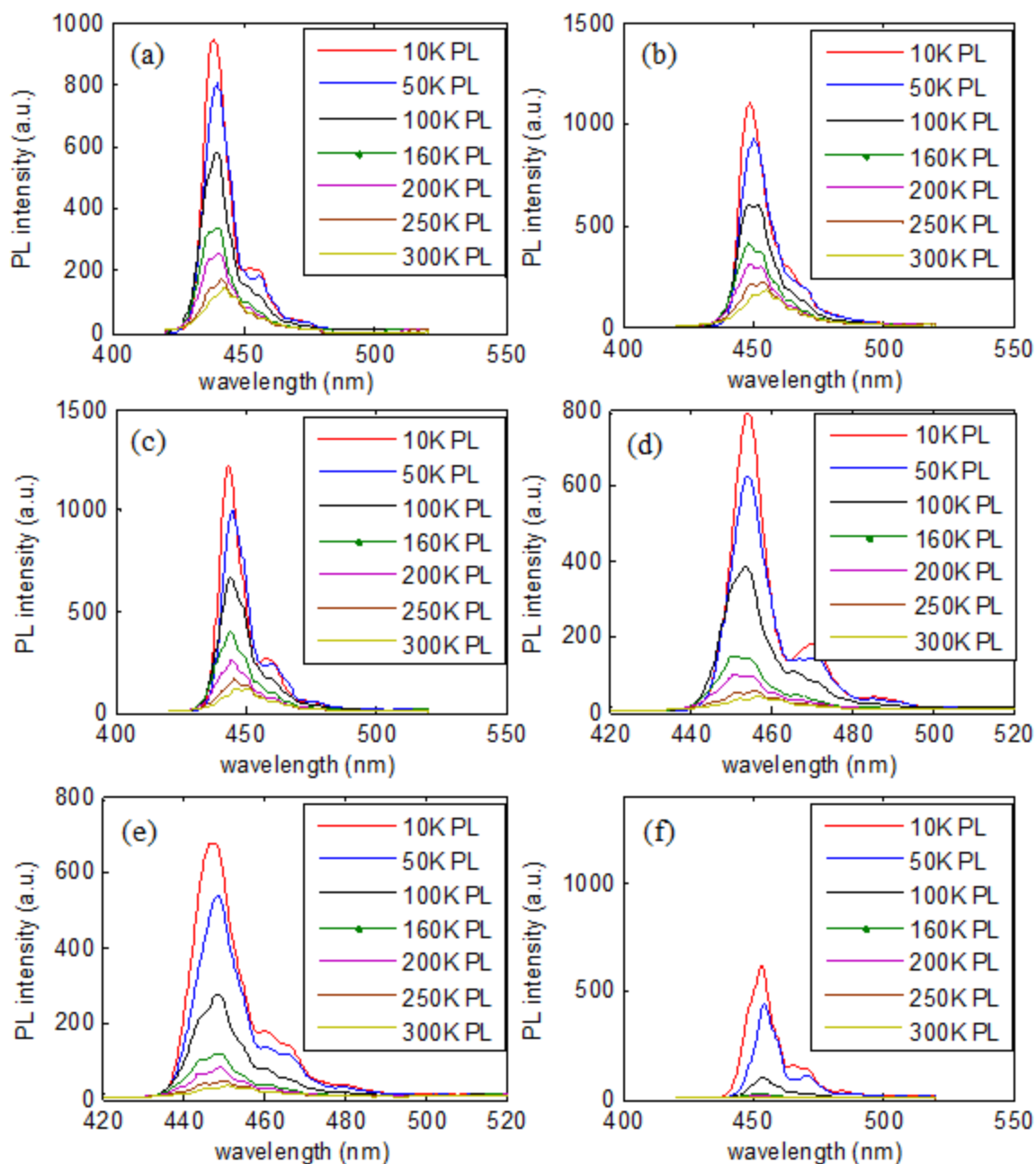
Figure 5.3: (Color) PL spectrums at different temperatures for (a) sample #1, (b) sample #2, (c) sample #3, (d) sample #4, (e) sample #5, and (f) sample #6

As temperature increases, the PL intensity decreases, indicating higher probability of nonradiative recombination at higher temperature. The spectrum-integrated PL intensities are calculated for PL spectra measured at 10 K and at 300 K and are listed in Table 5.1. At 10 K, different samples have near equivalent spectrum-integrated PL

intensities, while at 300 K, their spectrum-integrated PL intensities have an-order-of-magnitude variation. Since IQE can be calculated as

$$IQE = \frac{\text{spectrum integrated PL intensity @300K}}{\text{spectrum integrated PL intensity @10K}},$$

(5.2)

the IQE of the MQW samples have one order of magnitude variation, as listed in Table 5.1. Notice that generally MQW sample with higher room temperature average PL intensity shows higher IQE, as shown in Figure 5.4.
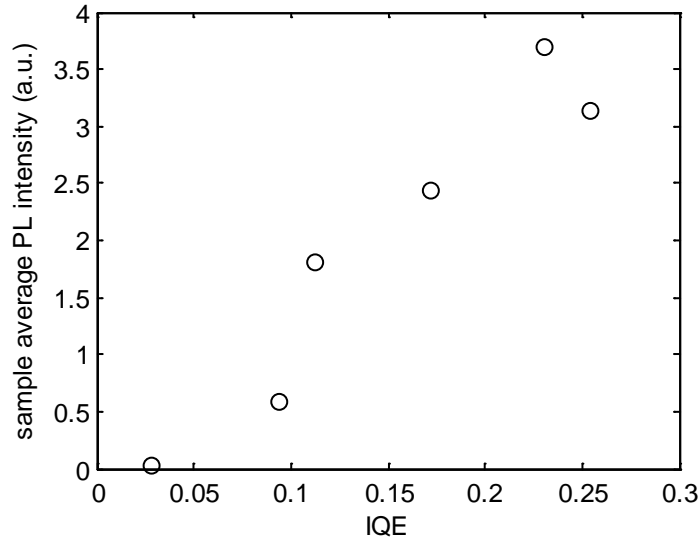
Figure 5.1: Room temperature sample average PL intensity vs. IQE.

To better understand the temperature-dependent spectrum-integrated PL intensity, in Figure 5.5, spectrum-integrated PL intensities are plotted as a function of the reciprocal value of temperature. And Arrhenius equation is used to fit the plot. First, a standard Arrhenius equation is tried to fit the experimental data:

$$I(T) = \frac{I_0}{1 + A\exp(-E_A / k_B T)},$$

(5.3)

where $I(T)$ is the temperature-dependent spectrum-integrated PL intensity, I_0 is the spectrum-integrated PL intensity at 10 K, k_B is Boltzman constant, A is a rate constant which is related with density of NRRCs [115], and T is the temperature in Kelvin.
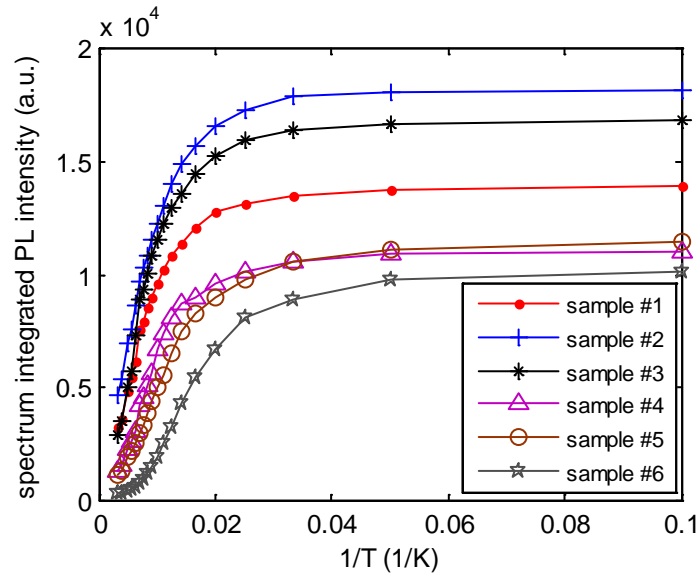
Figure 5.5: (Color) Spectrum integrated PL intensity as a function of 1/T for InGaN/GaN MQW samples.

By using standard Arrhenius equation for the fitting, it is assumed that there is only one nonradiative channel. Figure 5.6 shows the fitting curves on the experimental data of sample #1. It is seen that the fitting based on standard Arrhenius equation differs from the experiment curve a lot, especially at low temperature range. Same fitting process is repeated on other samples and similar results are obtained. This means that the standard Arrhenius equation could not provide good fitting to the experimental data, indicating that one nonradiative recombination channel is not enough to describe the temperature-dependent behavior. In this case, two nonradiative channels are assumed, and the second-order Arrhenius equation is used:

$$I(T) = \frac{I_0}{1 + A\exp(-E_A / k_B T) + B\exp(-E_B / k_B T)}, \tag{5.4}$$

where E_A and E_B are the activation energies for two nonradiative recombination channels, and A and B are the rate constants of the two channels [115]. In Figure 5.6, the black solid line shows that the fitting curve based on second-order Arrhenius equation give a very good fitting to the experimental data. The calculation is then repeated for all the other samples and similarly fitting based on Equation (5.4) gives good result with adjusted R-square larger than 0.99. The activation energies and the rate constants obtained from curve fitting are listed in Table 5.1.
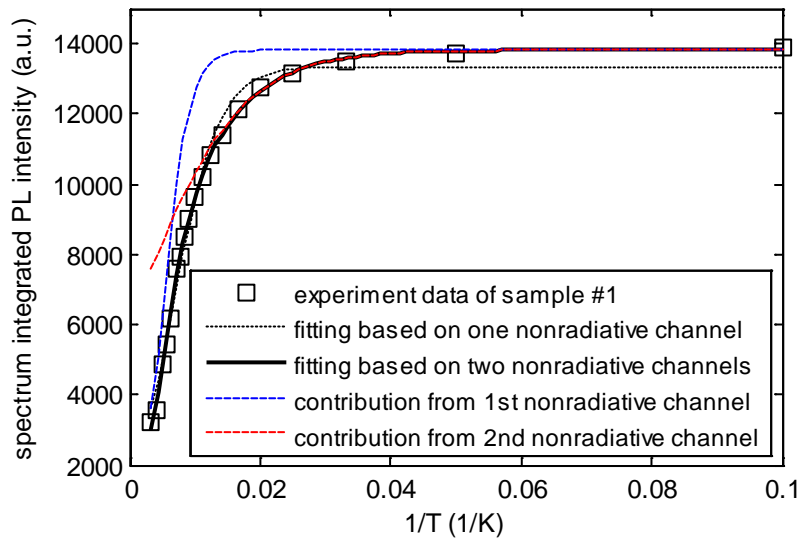
Figure 5.6: (Color) Spectrum integrated PL intensity as a function of temperature for sample #1 and the fitting curves to it.

The contributions from each nonradiative channel are plotted individually in Figure 5.6 based on the following equation:

$$I_1(T) = \frac{I_0}{1 + A\exp(-E_A / k_B T)} \text{ and } I_2(T) = \frac{I_0}{1 + B\exp(-E_B / k_B T)}, \tag{5.5}$$

where A, E_A, B, and E_B have same meaning as in Equation (5.4). Figure 5.6 shows that at high temperature the nonradiative recombination is mainly affected by the first channel (with higher activation energy E_A) since it provides better fitting to the experimental data at high temperature, while at relatively low temperature the second nonradiative channel (with lower activation energy E_B) dominates the nonradiative recombination process, since it provides better fitting to the experimental data at low temperature. Since the activation energy of the first channel is on the same order as the bandgap energy fluctuation, it is reasonable to attribute this nonradiative behavior to thermal activation of carriers out of the confining potential in QW layer [116]. A proof is the fact that the integrated PL intensity is quenched a lot at the temperature range where the first nonradiative channel dominates. A second proof is that rate constant A decreases with increasing thermal activation energy and sample average intensity decreases with increasing rate constant, as shown in Figure 5.7(a) and (b), indicating that carriers thermal activated by E_A are consumed by nonradiative recombination quickly. From the above analysis, E_A shows the depth of the confining potential. A rough correlation between E_A and the sample average PL intensity can be seen, as shown in Figure 5.7(c), a detailed explanation of this phenomenon will be explained later in this research. The origin of the second nonradiative channel is not yet clear, because of its small activation energy. One possible reason is thermal quenching of bound excitons towards free exciton band [115, 117]. However, it is very difficult to determine what kind of bound exciton dominates in this process due to the complexity of the structure. Another possible reason for the second nonradiative channel is thermal activation of carriers out of weakly localized state.
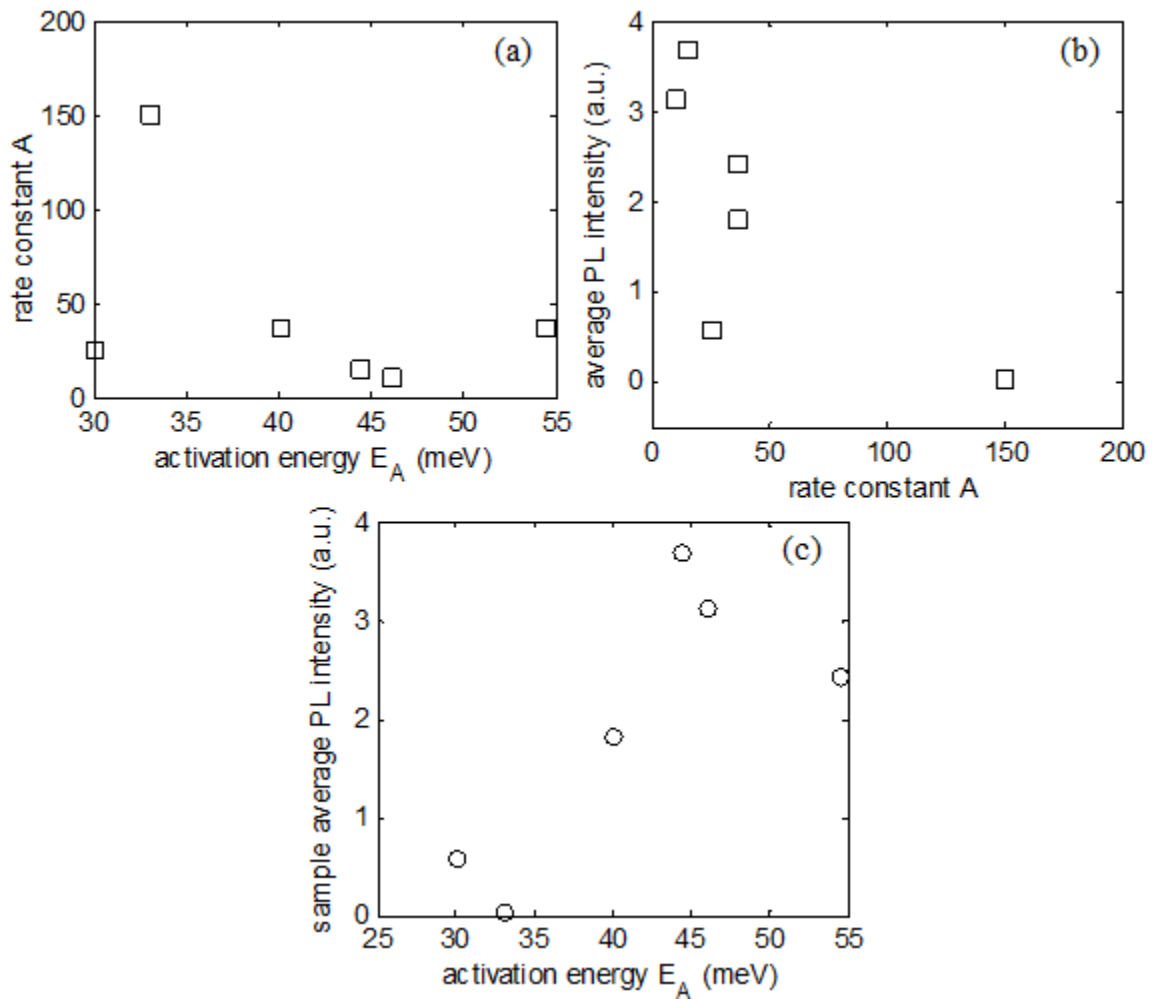
Figure 5.7: (a) first channel rate constant vs channel activation energy; (b) sample average intensity vs first channel rate constant(c) sample average intensity vs thermal activation energy E_A.

5.1.2 S-shaped PL Peak Energy Shift and Inverse S-shaped FWHM Shift with Increasing Temperature

In addition to the change in PL intensity, Figure 5.3 also shows that the PL peak energy shifts when temperature increases from 10 K to 300 K. However, different from what is predicted by Varshni's empirical expression:

$$E_g(T) = E_g(0) - \frac{\alpha T^2}{(T + \beta)},$$

(5.6)

where α=0.6965 meV/K and β=603.36 K [118], which states that the bandgap energy of semiconductor shrinks as temperature increases, the shift of PL peak energy with increasing temperature in Figure 5.3 shows more like an 'S-shaped curve'. For convenient observation, the PL peak photon energy is plotted as a function of temperature, as shown in Figure 5.8. When temperature increased from 10 K to 300 K the PL peak energy showed an S-shaped red-blue-red shift, which can be divided into three parts: (1) below about 70 K, PL peak energy decreases with increasing temperature; (2) from 70 K to around 160 K, PL peak energy increases with increasing temperature; and (3) above 160 K, PL peak energy again decreases with increasing temperature. Moreover, the FWHM of the PL spectra shows an inverse S-shaped shift with increasing temperature, as shown in Figure 5.9, which can also be divided into the above-mentioned three parts.

The reason for this S-shaped shift of PL peak energy and inverse S-shaped shift of FWHM can be explained using carrier localization at confining potential and carrier dynamics, as shown in Figure 5.10 and Figure 5.11.

(1) When temperature is below 70 K, the radiative recombination dominates the recombination process, so the radiative recombination lifetime (τ_r) is shorter than the nonradiative recombination lifetime (τ_{nr}). The radiative recombination lifetime can be expressed as [119]:

$$\tau_x^{2D} \propto \frac{1}{E_B^{2D}} \cdot \frac{M}{\mu} \cdot \frac{\Delta(T)}{1-\exp(-\Delta(T)/k_B T)} \qquad (5.7)$$
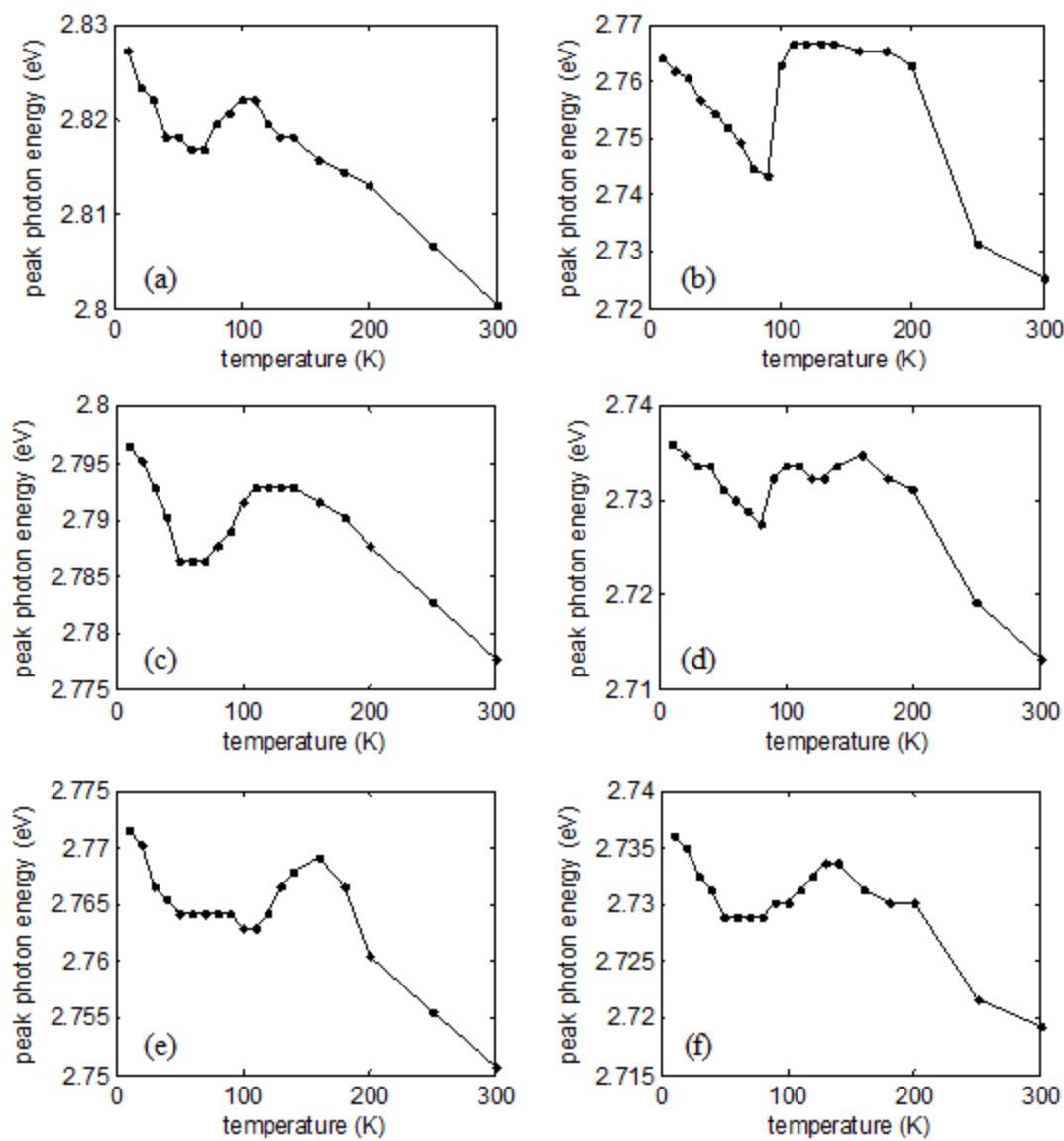
Figure 5.8: PL peak photon energy vs. temperature for (a) sample #1, (b) sample #2, (c) sample #3, (d) sample #4, (e) sample #5, and (f) sample #6
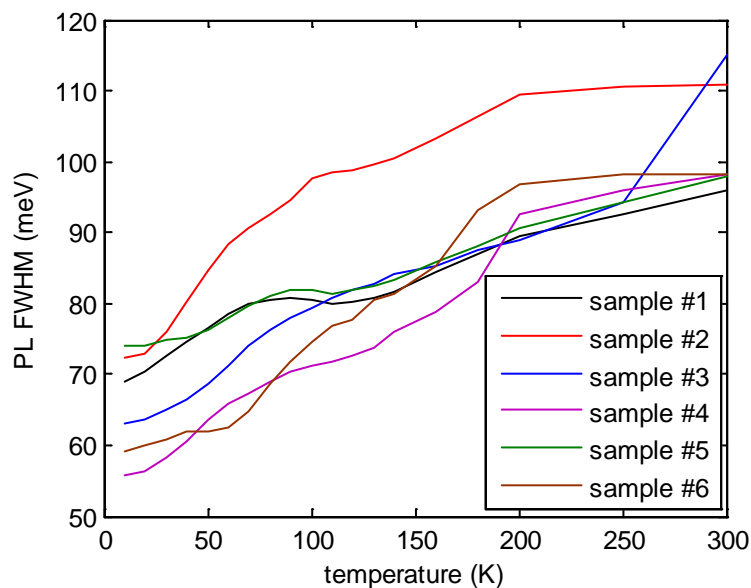
Figure 5.9: PL FWHM vs temperature.
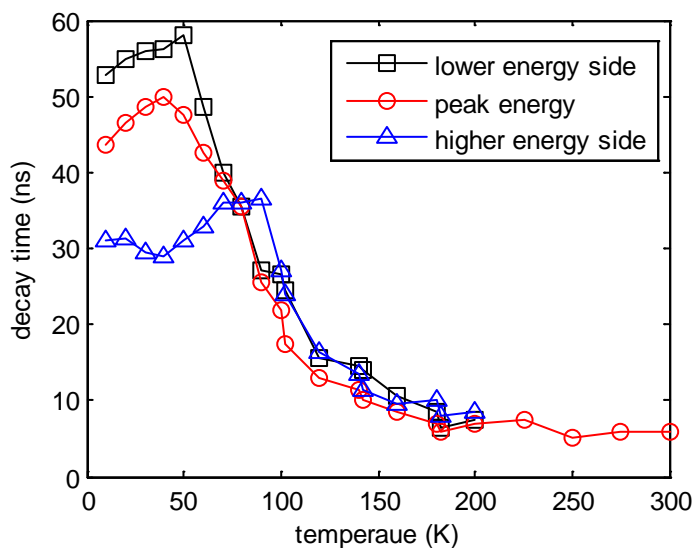
Figure 5.10: PL lifetime vs. temperature for the InGaN/GaN MQW structure. Note that for T<70 K the lifetime is smaller at lower energy side, while for T>70 K there is no difference between those three lifetimes. This 70 K is also the temperature at which the InGaN PL peak energy turns from redshift to blueshift with increasing temperature. Replotted from [120].
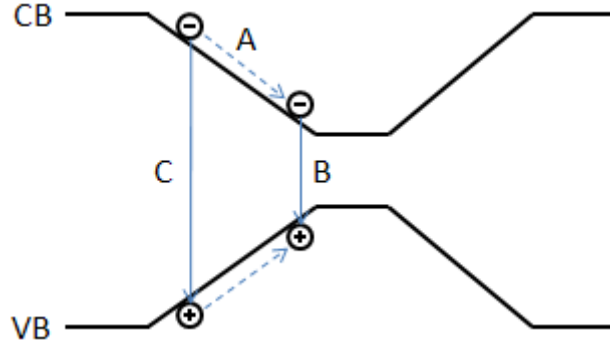
Figure 5.2: Explanation of red-blue-red shift of PL peak position as temperature increases. Process (A) shows the carriers relax down to the bottom of confining potential; process (B) shows the recombination at bottom of confining potential; and process (C) shows carriers recombine before reaching the bottom of the confining potential.

where $E_B^{2D} = 4h^2 / \mu (a_0^{2D})^2$ is the quasi 2D exciton binding energy, $a_0^{2D} = (m_0 \varepsilon_r / \mu) a_H$ is the 2D exciton Bohr radius, μ is the reduced mass $\mu^{-1} = (m_e^*)^{-1} + (m_h^*)^{-1}$, $M = m_e^* + m_h^*$, m_0 is the free electron mass, ε_r is the relative permittivity, a_H is the Bohr radius of the hydrogen atom, k_B is Boltzmann constant, and $\Delta(T)$ is the exciton linewidth at finite temperature. Basically, this radiative recombination lifetime is temperature dependent for the $\Delta(T)$ and $k_B T$ terms in Equation (5.7). For temperature below 70 K, the width $\Delta(T)$ is dominated by impurity and interface scattering and acoustic phonon scattering, as a result $\Delta(T)$ is much smaller than $k_B T$. Consequently, Equation (5.7) can be simplified into

$$\tau_x^{2D} \propto \frac{1}{E_B^{2D}} \cdot \frac{M}{\mu} \cdot k_B T \tag{5.8}$$

So the radiative recombination lifetime is proportional to temperature. Since the carrier lifetime (τ) is calculated by

$$\frac{1}{\tau} = \frac{1}{\tau_r} + \frac{1}{\tau_{nr}}, \tag{5.9}$$

it is predominantly affected by the smaller lifetime. As a result, as the temperature increases from 10 K to 70 K, radiative recombination lifetime increases and so does the carrier lifetime. This agrees with other researcher's experiment results. In Figure 5.10, for 10-70 K the measured lifetimes changes very small and there is large difference between the lifetimes measured above, at, and below the peak energy, which means that radiative recombination processes are dominant. Moreover, Figure 5.10 also shows that the carrier lifetime increases as temperature increases in this temperature range.

As their lifetime increases, carriers can diffuse down deeper into the confining potential before recombination, as shown in Figure 5.10 as step (A) and (B). This reduces the recombination energy, and as a result leads to a redshift in the peak energy with increasing temperature. Moreover, as the lifetime increases, carriers can diffuse to more energy states, which increases the number of energy states during recombination, and increases the PL FWHM.

(2) When temperature is between 70 K and 160 K, nonradiative process becomes dominant during carrier recombination, so nonradiative recombination lifetime is shorter than radiative recombination lifetime and carrier lifetime is mainly affected by nonradiative recombination lifetime. Since nonradiative recombination lifetime is related with temperature by [119]

$$\tau_{nr} = \frac{1}{sN_T\sqrt{8k_BT / \pi m^*}} \tag{5.10}$$

where s is carrier capture cross section, N_T is the density of NRRCs, and m^* is carrier effective mass, it decreases when temperature increases. Detailed calculation shows that

when temperature increased from 70 K to 160 K, the nonradiative recombination lifetime decreases by about 18% of the τ_{nr} at 10 K. Consequently, carrier lifetime decreases with increasing temperature at 70 K to 160 K.

Figure 5.10 shows a similar result. As the temperature increases beyond 70 K, the lifetime quickly decreases, indicating that the emission becomes mainly affected by nonradiative recombination process; the fact that in contrast to situations for T<70 K there is almost no difference between lifetimes above, at and below the peak for T>70 K can be a further proof of this. This 70 K is the characteristic temperature at which the PL peak energy turns from redshift to blueshift with increasing temperature.

With increasing temperature from 70 K to 160 K, carriers have shorter lifetime to diffuse to the potential minimum before recombination, as shown in Figure 5.11 as process (C). This leads to a blueshift in the peak energy as temperature increases, and broadens the higher energy side emission.

On one hand, the smaller lifetime reduces the number of energy states that the carriers can diffuse to, which reduces PL FWHM. On the other hand, the higher temperature increases the number of energy states that the carriers can reach, which increases the PL FWHM. The combination of these two factors leads to a near-stable PL FWHM at this temperature range.

(3) Above 160 K, as the nonradiative recombination lifetime is still shorter than the radiative recombination lifetime, the nonradiative recombination still dominates the recombination process. This can be proved in Figure 5.10 by very small carrier lifetimes and little difference between lifetimes above, at and below the peak. However, in this temperature range with increasing temperature the nonradiative recombination lifetime

decreases by only 6% of the τ_{nr} at 10 K, which is very small. As a result, carrier lifetime stays almost constant (in contrast to case (2)). In this case, the blueshift behavior caused by shorter carrier lifetime becomes insignificant. On the other hand, the temperature-induced bandgap shrinkage effect, introduced by Varshni's empirical expression, becomes relatively significant in this temperature range, since the bandgap energy shrinks by 46.1 meV when temperature increases from 160 K to 300 K, which is twice as large as the 18.3 meV bandgap shrinkage when temperature increases from 70 K to 160 K. This shrinkage in bandgap energy leads to the redshift in PL peak energy.

Because the carrier lifetime stays almost constant, the decrease of PL FWHM is minimized. However, the high temperature provides high thermal energy to the carriers so that they can hop between energy states within a much larger energy range, which increases the available number of energy states during recombination. As a result, the PL FWHM increases.

Consequently, inhomogeneity, carrier localization, and the change of carrier lifetime in the InGaN/GaN MQWs lead to the change of the carrier dynamics, resulting in carrier recombination at different energies of the localized states, the S-shaped shift of PL peak energy and the inverse S-shaped shift of PL FWHM.

5.2 CLSM Imaging and TRPL Measurements

5.2.1 CLSM Imaging and Bandgap Energy Fluctuation

A total of 14 blue-emitting InGaN/GaN MQW samples, grown under 3 different pressure regimes: 200 Torr, 450 Torr, and 700 Torr, are analyzed using the CLSM system. As mentioned in Section 2.3.2.4, for all conditions, the GaN templates are identical with equivalent morphology and TD density as measured using AFM and XRD, leading to

near-equivalent TD density in each MQW sample. In addition, the MQW layer structure is maintained at the same period thickness as measured using XRD by adjusting both TEGa and TMIn flows while keeping the TMIn/TEGa molar ratio constant. Detailed growth parameters are listed in Table 5.2. In this case, the MQW structures are close to exactly the same such that QCSE and strain-related internal electric fields are considered not to be a major influence in the run-to-run comparison. The growth temperature is also tuned to achieve a target PL peak wavelength of ~449 nm, corresponding to an indium composition of ~14%. Despite having near-equivalent structural properties, the samples exhibited different average PL intensities, varying by factors of two when measured using a Nanometrics PRMBlue PL system. Figure 5.12 shows the PL spectra of the samples, excited by a He-Cd laser. In this research the PL excited by He-Cd laser is called ensemble PL, since the excitation laser has a beam diameter of 1.1 mm, which is much larger than the microstructures on the MQWs. Notice that in Table 5.2, the effective V/III ratio is defined as
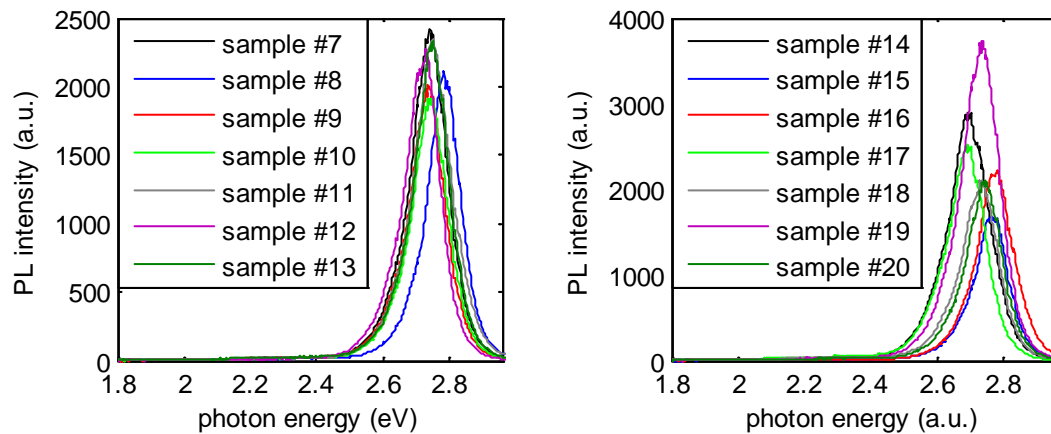
Figure 5.3: Ensemble PL spectra of samples #7 to #20. Excited by 325 nm HeCd laser and measured by OceanOptics USB2000.

$$V/III^* = \frac{\text{\# of mole of NH}_3}{\text{\# of mole of Alkyls}} \times \frac{\text{NH}_3 \text{ flow rate}}{\text{NH}_3 \text{ flow rate} + \text{N}_2 \text{ flow rate}}$$
$$= V/III \times \frac{\text{NH}_3 \text{ flow rate}}{\text{NH}_3 \text{ flow rate} + \text{N}_2 \text{ flow rate}}, \qquad (5.11)$$

which is actually a combination of the V/III ratio and NH$_3$ partial pressure ratio; and effective gas speed is defined as

$$S^* = (\text{wafer carrier rotation speed}) \times (\text{gas velocity at injector plate}). \qquad (5.12)$$

which is a combination of wafer carrier rotation speed and gas velocity. The effective gas speed shows how long injected gas can stay above the samples. Obviously, the faster the wafer carrier rotates and the gas flows, the larger the effective gas speed is, and the shorter time gas can stay.

Figure 5.13(a) shows the CLSM images of sample #7, taken with 445/40 nm BPF, where bright regions, on the order of micrometers in size, are surrounded by dark regions whose PL intensity was approximately 2-4 times smaller than the bright region's PL intensity. The CLSM imaging is repeated on all the samples, and similar results are obtained, as shown in Figure 5.13.

CLSM image was also taken with 538 nm LPF, to collect the yellow luminescence information. As shown in Figure 5.14, few features can be seen from the image, indicating very small yellow luminescence from the samples. This is in consistence with the ensemble PL spectra shown in Figure 5.12, which also show no yellow luminescence at all.

Table 5.2: Parameters used in MOCVD growth

Sample ID	Growth pressure (Torr)	Growth temperature (°C)	In/Ga ratio (molar)	N_2/NH_3 flow rate (slm)	V/III ratio	Effective V/III ratio (V/III*)	Rotation (rpm)	Gas speed	Effective gas speed (S*)
#7	200	788	1.69	134/52	15924	4457	800	0.13	104
#8	200	786	1.69	121/32	10278	2123	600	0.11	66
#9	200	790	1.69	101/52	17131	5778	600	0.11	66
#10	200	792	1.69	164/52	15767	3820	1000	0.15	150
#11	200	789	1.68	134/52	16093	4504	800	0.13	104
#12	200	792	3.02	134/52	10776	3016	800	0.13	104
#13	450	795	1.68	243/53	13724	2463	800	0.09	72
#14	450	798	1.68	291/54	11906	1851	1000	0.11	110
#15	450	801	1.69	347/54	15474	2092	600	0.08	48
#16	450	788	1.92	223/73	36225	8948	800	0.09	72
#17	700	800	1.69	287/74	17482	3572	690	0.07	48.3
#18	700	808	1.69	329/34	7346	684	690	0.07	48.3
#19	700	814	1.68	352/75	17050	2979	880	0.09	79.2
#20	700	806	1.69	354/85	19023	3668	920	0.09	82.8
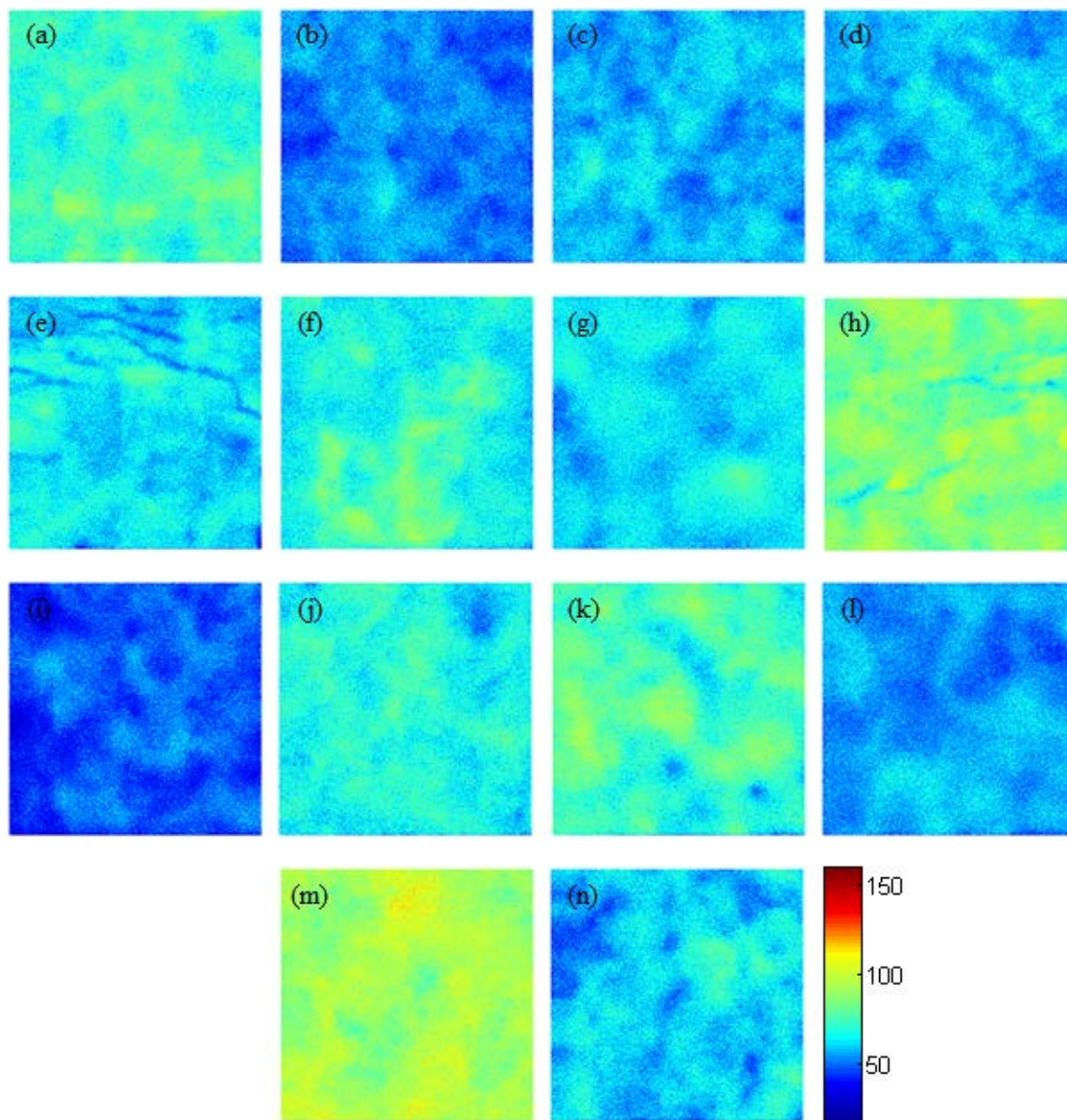
Figure 5.13: CLSM images taken with 445/40 nm BPF. (a) to (n) corresponds to sample #7 to #20, respectively. All images are 20μm×20μm in size.
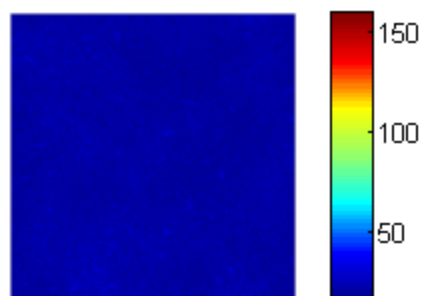
Figure 5.14: CLSM images for sample #7, taken with 538 nm LPF. Image is 20μm×20μm in size.

PL spectra measured at different places on sample #7 in Figure 5.13(a) show that the bright region has a PL intensity 3.27 times stronger than the dark region, and its PL peak energy is 44.2 meV smaller than the PL peak energy in the dark region, as shown in Figure 5.15. The PL spectra measurements are repeated on all samples and similar results are obtained. The PL peak in bright regions is 2-4 time higher, with peak energies being tens of meV red-shifted, compared to the PL peak in dark regions, indicating a smaller bandgap energy in bright regions. The PL peak intensity and transition energy difference data are all listed in Table 5.3.
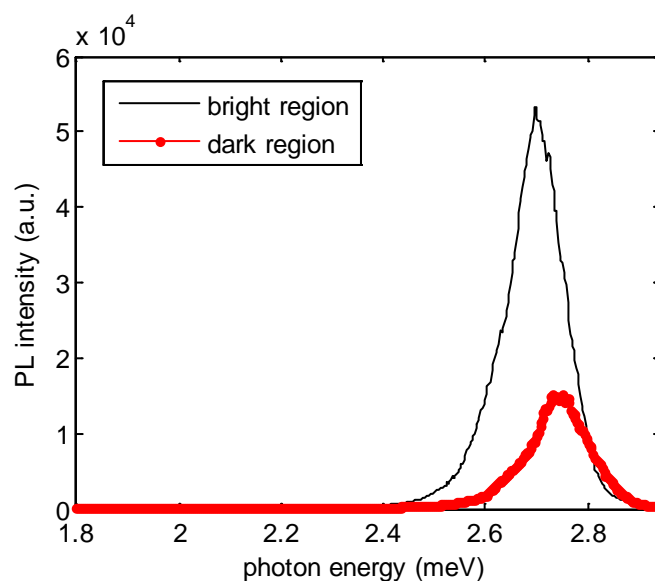
Figure 5.15: PL spectra at both bright region and dark region for sample #7.

It is proposed that carrier localization is the primary driver for the PL contrast differences observed in the samples; the smaller bandgap energy is the reason for the higher PL intensity in the bright regions. This is because the energy barriers between small-bandgap-energy regions and large-bandgap-energy regions make it very difficult for carriers in small-bandgap-energy regions to escape. Therefore, carriers are localized in the small-bandgap-energy regions, resulting in limited diffusion length and low possibility to meet NRRCs. On the contrary, in large-bandgap-energy regions, carriers are not limited in diffusion so that they can easily be captured by the nearby small-bandgap-energy regions or captured by nearby NRRCs, leading to low carrier concentration in the large-bandgap-energy regions and a high probability of nonradiative recombination. The combination of the two effects, low concentration of carriers and high probability of nonradiative recombination, leads to low PL intensity in large-bandgap-energy regions. Consequently, the small-bandgap-energy regions limits the diffusion of the carriers and reduce their chance to meet NRRCs, so the probability of nonradiative recombination is reduced. It should be noted that in this research the observed potential energy fluctuations were probably the result of QW layer thickness fluctuations, as the indium content fluctuation can be largely avoided for indium content smaller than 20% [90, 121].

Table 5.3: CLSM image data for group 2 samples

Sample ID	CLSM image average intensity	Ensemble PL peak energy (eV)	Ensemble PL FWHM (meV)	Bright region bandgap energy (eV)	Bright region PL FWHM (meV)	Dark region PL FWHM (meV)	Bandgap energy difference (meV)	Peak intensity ratio	CLSM image Standard deviation
#7	70	2.737	125.9	2.696	130.93	136.01	44.2	3.27	8.78
#8	49	2.785	120.7	2.781	111.6	113.27	39.1	3.06	7.44
#9	54	2.737	121.2	2.751	134.72	136.63	25.4	3.01	7.69
#10	55	2.745	124.1	2.731	135.89	138.05	30.5	3.13	7.70
#11	60	2.752	129	2.726	137.46	145.13	37.5	3.21	8.76
#12	66	2.724	124	2.694	123.13	127.11	41.6	3.27	9.61
#13	60	2.749	118.1	2.738	130.76	133.8	35.3	3.27	8.38
#14	80	2.694	122.3	2.689	130.34	138.29	41.5	3.58	9.58
#15	44	2.762	119.7	2.751	121.94	125.96	22.8	2.93	7.52
#16	64	2.780	125.1	2.733	133.79	144.67	47.9	3.79	8.48
#17	71	2.694	129.2	2.701	129.33	136.23	36.9	3.70	9.89
#18	52	2.737	125	2.711	129.31	133.24	27.1	3.09	7.63
#19	88	2.737	133.6	2.731	133.92	138.86	45.3	4.12	9.71
#20	57	2.745	124.1	2.733	130.17	131.36	27.6	3.23	8.90

In previous chapters it was mentioned that TDs are generally NRRCs, so it is interesting to analyze the role of TDs in the current samples. This analyze is feasible since very large V-pits with diameter of about 4 μm were found during CLSM scanning on sample #14, as shown in Figure 5.16(a). PL spectrum taken on the side wall of the V-pits indicates no luminescence peaks below 2.95 eV (beyond 420 nm) at all, as shown in Figure 5.16(b). A possible reason is that the bandgap energy of the V-pits sidewalls is larger than the excitation photon energy. To identify this, SEM and CL are also utilized. However, due to the high resolution and small size of the CLSM, SEM and CL, it is very difficult to image the same place with these two techniques. Figure 5.17(a) shows the SEM image of sample #14, with two large V-pits having the same size as the one in Figure 5.16. CL spectrum taken on the sidewalls of the V-pits shows a peak at 3.4 eV, corresponding to GaN bandedge emission, as shown in Figure 5.17(b). The measurement is repeated several time and similar results are obtained. The fact that no peaks other than GaN bandedge emission shows on the sidewall indicates that no MQWs are grown on the sidewalls of the V-pits, as shown in Figure 5.17(d), so carriers in MQWs cannot diffuse to TDs. As a result, in the current research, the TDs which are surrounded by V-pits can hardly contribute to nonradiative recombination, since the TDs are "screened" by regions with large bandgap energy. A further proof of this is that the SEM and CL measurements showed that the V-pits occurred in both bright and dark regions with near equivalent density and size distribution [122], as shown in Figure 5.18.
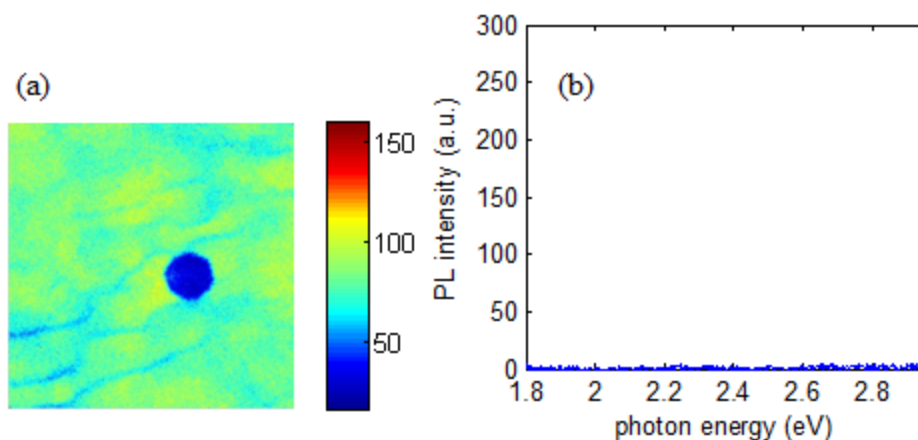
Figure 5.16: (a) CLSM image of sample #14 taken with 445/40 nm BPF, showing a very large V-pit with the size of about 4 μm, the image is 20μm×20μm in size; (b) PL spectrum taken at the sidewall of the V-pit.
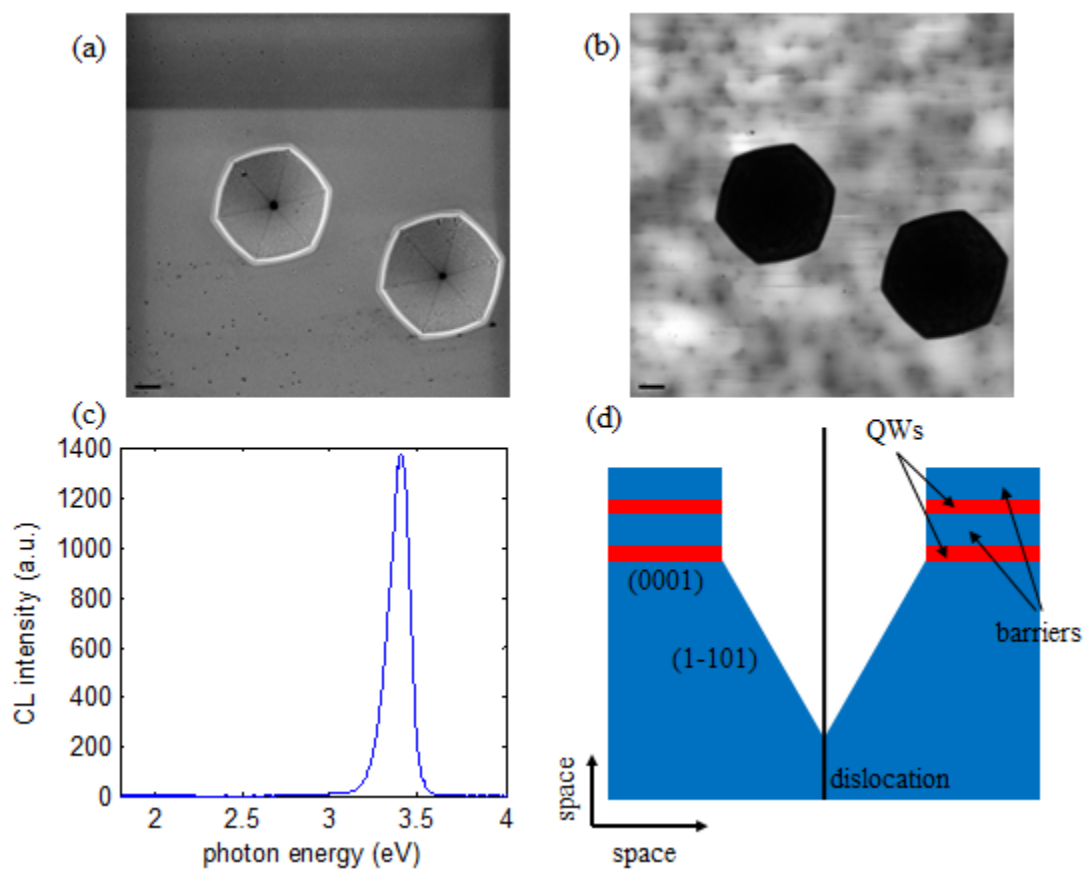
Figure 5.17: (a) SEM image of sample #14 showing surface morphology, large V-pits can be seen; (b) CL image showing intensity distribution at 459 nm, taken at the same place as SEM image; (c) CL spectrum taken at the sidewall of the V-pit; (d) model of the V-pits showing no MQWs on the sidewalls. The SEM and CL images are 15μm×15μm.
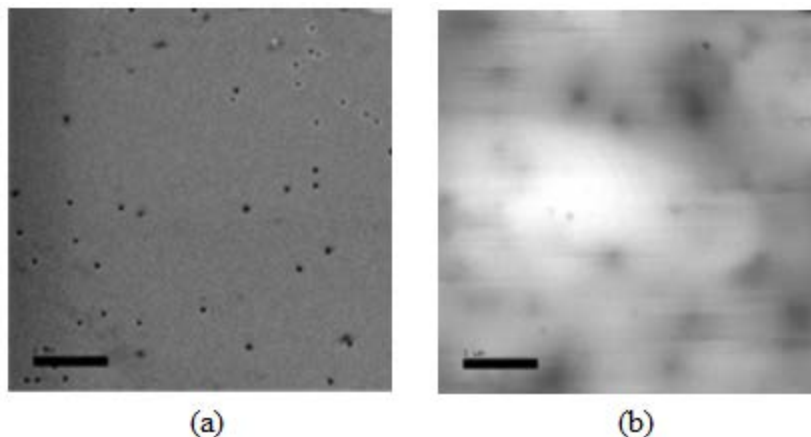
Figure 5.18: SEM image (a) and CL image at 445 nm (b) of the same place on sample #14. Both images are 5μm×5μm.

Due to the large excitation laser beam diameter, the ensemble PL light is actually the combination of the PL light from both bright regions and dark regions, so the ensemble PL light spectrum is related to the bandgap energy distribution in the sub-micrometer scale, that is to say, the FWHM of the ensemble PL spectrum is related with the bright region-dark region bandgap energy difference [123]. The larger the bandgap energy difference is, the more the PL in bright region is red-shifted comparing with the PL in dark region. As a result, a rough correlation can be seen between the bandgap energy difference and the ensemble PL FWHM, as shown in Figure 5.19(a). The reason why in Figure 5.19 (a) the ensemble PL FWHM does not increasing monotonically with bandgap energy difference is probably that the ensemble PL is excited in a much larger area (circle with 1.1 mm diameter) and covers more microstructural features than the CLSM image (where the bandgap energy difference is extracted) does. The FWHM of the PL spectra in bright and dark regions are also calculated, as indicated in Figure 5.19 (b). It is seen that the FWHM in the bright regions is always smaller than the FWHM in

the dark regions, indicating stronger confinement in bright region as a result of larger local QW layer thickness [100]. All the FWHM data can be found in Table 5.3.
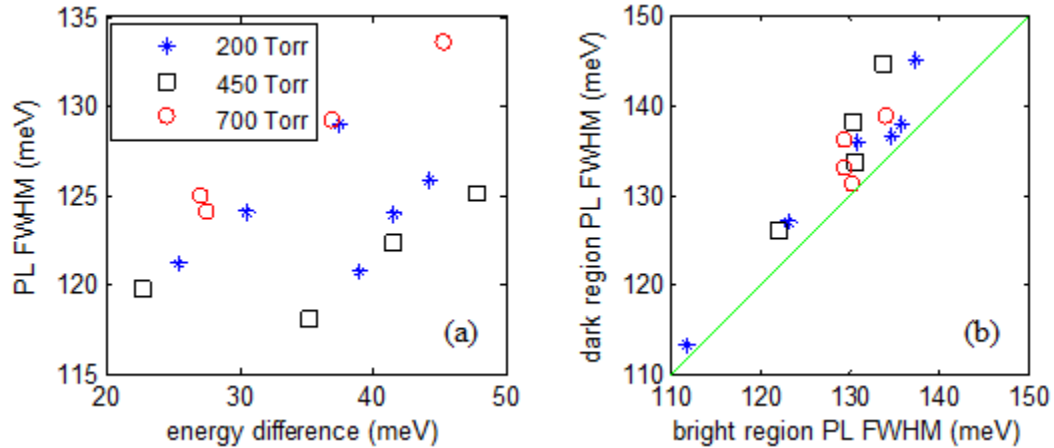
Figure 5.19: (a) FWHM of ensemble PL vs. bandgap energy difference between bright region and dark region; (b) PL FWHM in dark regions vs. PL FWHM in bright regions, solid line shows the place where the two FWHMs equal. InGaN MQWs grown under different pressure are marked with different symbols.

The pixel average intensity of CLSM image is defined as the mean value of each pixel's intensity on the image:

$$\text{CLSM image average intensity} = \frac{\sum \text{pixel intensity}}{\text{number of pixels}}. \tag{5.13}$$

It represents the brightness of the image and the average PL intensity of the MQWs over the sampled area. The CLSM image average intensities of all the samples are listed in Table 5.3. A rough correlation can be seen between CLSM image average intensity and bandgap energy difference between bright region and dark region, as indicated in Figure 5.20(a). As has been proposed above, the energy barrier prevents carriers in small-bandgap-energy region from diffusing to large-bandgap-energy regions. For sample with large bandgap energy difference, a large barrier exists between bright and dark regions and thus localized carriers have very little chance to escape from the bright regions into

dark regions. This reduces the probability of carriers' nonradiative recombination, so more carriers recombine radiatively and a large average PL intensity is expected. In contrary, for sample with small bandgap energy difference, carriers are weakly localized in bright regions and can easily gain enough energy to escape, such that many carriers cannot contribute to radiative recombination and the number of carriers recombining radiatively is reduced, resulting in a small average PL intensity. A proof of this is that the bright region average intensity, which is calculated over a 10×10-pixel-area in the bright region of the CLSM image, increases with the increment of bandgap energy difference, as shown in Figure 5.20(b), indicating more carriers are localized in small-bandgap energy region and recombine radiatively at larger bandgap energy difference.
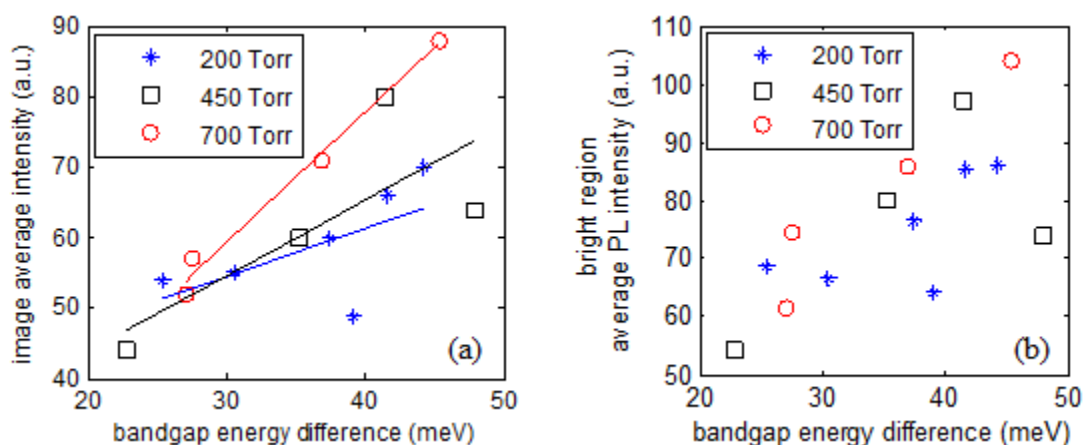
Figure 5.4: (a) CLSM image average intensity vs. bandgap energy difference between bright region and dark region, solid lines show the linear fitting to the data, the adj. R-square for the fitting are 0.22 for 200 Torr data, 0.38 for 450 Torr data, and 0.98 for 700 Torr data; (b)bright region average PL intenisty vs. bandgap energy difference between bright region and dark region.

Linear curve fitting conducted on the data in Figure 5.20(a) for different growth pressures showed that for samples grown at 200 Torr, the image average intensity increased with the energy difference at a rate of 0.68/meV, for samples grown at 450 Torr

the increasing rate is 1.07/meV, and for samples grown at 700 Torr the increasing rate is 1.86/meV, indicating that for samples grown under optimized high pressure conditions, the average intensity increases at a fast rate with the increase of the bandgap energy difference. It is conceivable that samples grown at higher pressure may have fewer point defect and vacancies, and as a result, better crystal quality.

It is also observed that the CLSM image becomes less uniform as the image average intensity increases, since the image standard deviation, which shows how much variation from the average, increases as the image average intensity increases. This is shown in Figure 5.21(a), and occurs because samples with higher average PL intensity have larger bandgap energy differences and larger differences between bright region PL intensities and dark region PL intensities, as indicated in Figure 5.21(b).
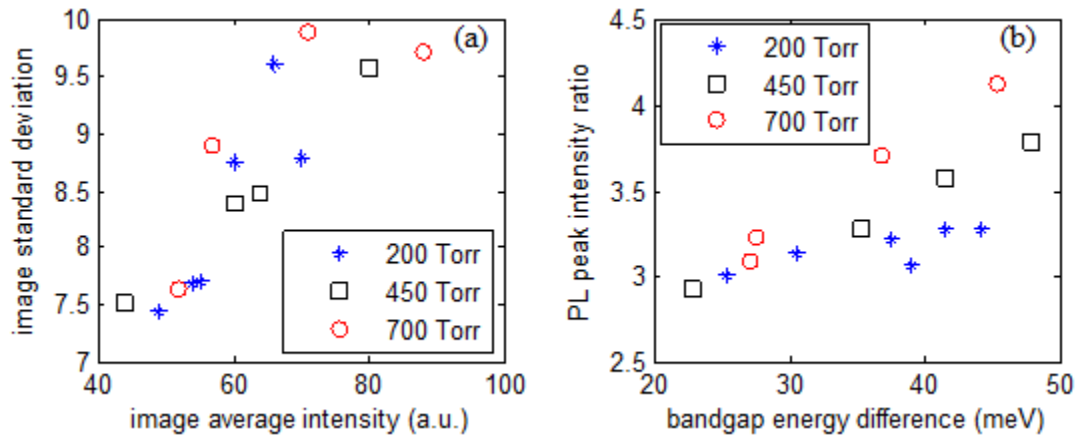
Figure 5.5: (a) CLSM image standard deviation vs. image average intensity; (b) PL peak intensity ratio vs. bandgap energy difference.

5.2.2 TRPL Measurement and PL Lifetimes

TRPL measurements are performed in both bright and dark regions for each sample in group 2. The TRPL spectra, with baseline removed and intensity normalized to

their peak, are plotted in Figure 5.22, showing different PL decay characteristics for the respective regions.

Generally, lifetime data is extracted from the TRPL spectrum by fitting the spectrum with exponential decay functions. Single exponential function, biexponential function, and stretched exponential function are most commonly used for the fitting. Single exponential function is used if there is only one decay-channel, biexponential function is used for two-decay-channel situation, and stretched exponential function is used for disordered system. Previously, because of the bandgap energy fluctuation, generated either by inhomogeneous distribution of indium or by quantum layer thickness fluctuation, InGaN was seen as disordered system and stretched exponential function was used to fit its TRPL spectra. However, although stretched exponential functions can provide very good fitting to TRPL spectra, it does not show significant physical meanings since it's very difficult to explain the stretching exponent β. As a result, in this work, stretched exponential function was not considered for the fitting. On the other hand, Chichibu proposed 'effective PL lifetime', which is the time when the area under TRPL spectrum decreases to 63.2% of the total area under TRPL spectrum [1, 70]. He was then able to compare effective lifetimes from different materials, since different materials may have different number of decay-channels and require different exponential functions for fitting to get lifetime, making the lifetimes from different materials incomparable. However, since in this work all of the samples are InGaN MQWs, effective PL lifetime is not necessary.
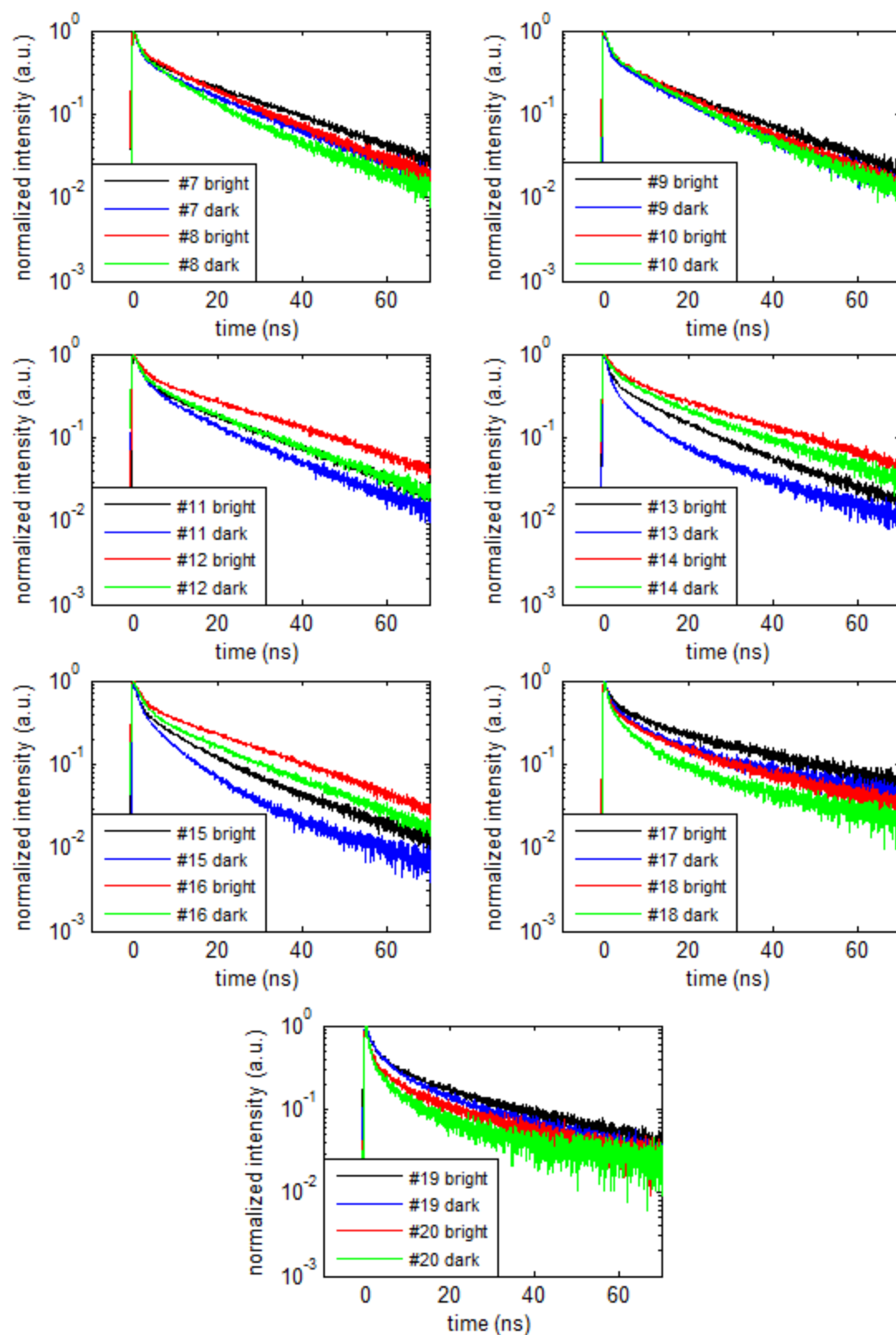
Figure 5.22: TRPL spectrum of samples in both bright region and dark region, with time resolution of 0.0296 ns.

Notice that in Figure 5.22 the y-axis is in logarithmic scale and that the PL intensities do not show linear decay in this logarithmic scale. This means that the PL intensities do not show single exponential decay characteristics and one decay-channel is not enough. In this case, two PL decay channels are assumed, and biexponential function is used for the fitting:

$$I(t) = I_0 + I_1 \exp(-\frac{t}{\tau_1}) + I_2 \exp(-\frac{t}{\tau_2}) \tag{5.14}$$

where I_0 is the baseline, I_1 and I_2 are the intensity of the two decay channels, and τ_1 and τ_2 are the lifetimes of the two decay channels. Since the TRPL spectra are already normalized, $I_0 = 0$.

One important factor needs to be considered when fitting TRPL spectra in Figure 5.22 is the system IRF (instrument response function), which shows the influence of the test system on the measurement results. Any measured result from the system is the convolution of IRF with the ideal result. Ideally, in the CLSM system, if the excitation laser pulse has infinitely narrow pulse width, and all electronics have infinitely short response time, the IRF is a δ function. In this case the measured TRPL spectrum is the same as ideal TRPL spectrum, since convolution of any function with δ function results in the function itself. However, in reality the excitation laser pulse has finite pulse width (as short as 49 ps for the current excitation laser), and the electronics have finite response time; so the IRF is actually a Gaussian function rather than a δ function, and the measured TRPL spectrum is broadened from the ideal TRPL spectrum by the convolution with IRF. In this case, in order to obtain the ideal TRPL spectrum from which accurate

lifetime data can be deduced, the influence from the laser pulse and electronics response are removed by deconvolution of the measured signal in Figure 5.22 with the IRF.

IRF of the CLSM system was measured by replacing the InGaN/GaN MQW samples with a Spectralon sample. Since the Spectralon sample did not fluorescence at all, excitation laser light was scattered when it was focused onto the Spectralon sample's surface. The scattering process finished instantly, after which the scattered light was detected and used for IRF measurement. As mentioned in Chapter 4, the laser beam pulse width depends on its output power; so the laser power was kept the same as the laser power used in TRPL measurements. Figure 5.23 shows the normalized IRF.
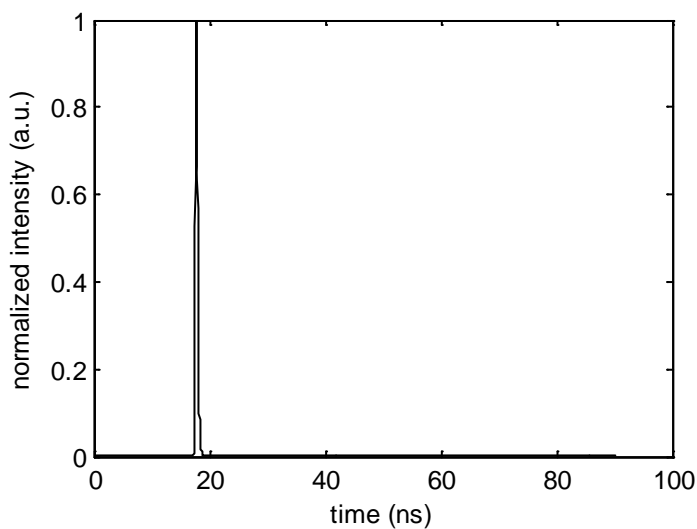
Figure 5.23: IRF of the CLSM system and TRPL system. The FWHM of the IRF is 385 ps.

Figure 5.24 shows one of the curve fitting result. Fitting to TRPL spectrum with biexponential function and deconvolution of IRF was successful since the adjusted R-square of the fitting was higher than 0.99. Two lifetimes obtained from the fitting are

listed in Table 5.4. The same curve fitting process is repeated on all the TRPL spectra and all lifetime data are listed in Table 5.4.
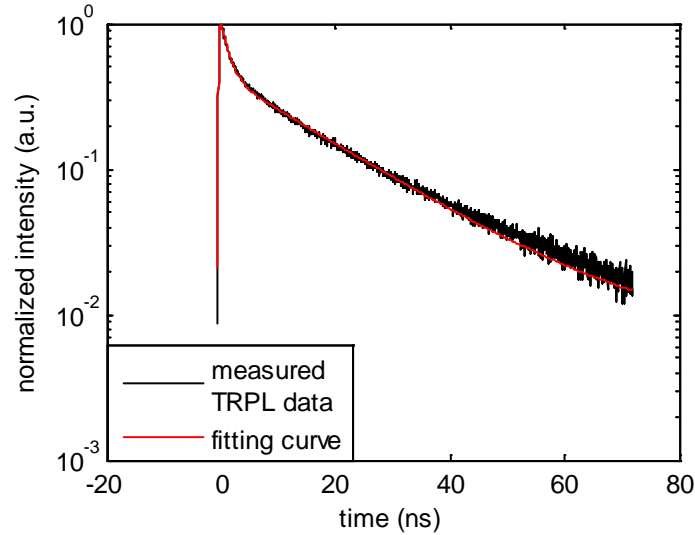
Figure 5.24: Measured TRPL spectrum for bright region in sample #7 and its fitting curve. The Adj. R-square of the fitting is 0.9973.

As shown in Table 5.4, for all samples, both bright region and dark region are characterized by two lifetimes: the short lifetime τ_1 is no more than 3 ns, indicating an early stage fast decay, and the long lifetime τ_2 is longer than 10 ns, indicating an extended slow decay. In our analysis, the fast decay with lifetime τ_1 corresponds to carrier localization in weakly localized states where radiative recombination is more quenched by NRRCs and also competes with carrier transportation into strongly localized states, while the slow decay with lifetime τ_2 corresponds to carrier localization in strongly localized states [124].

Based on previous analysis, one would expect to see that fast decay with lifetime τ_1 only occurs in dark region and slow decay with lifetime τ_2 only occurs in bright region, as it is shown that dark region has large bandgap energy, making it weakly localized state,

and bright region has small bandgap energy, making it strongly localized state. This is in contrary to what is listed in Table 5.4, in which both bright and dark regions have both fast decay and slow decay lifetimes. The possible solution is that the bandgap energy also fluctuates slightly in nanometer-scale in both bright region and dark region, as mentioned in Chapter 3. In this case, the fast decay lifetime τ_1 actually corresponds to carrier localization in local weakly localized states, which is mainly quenched by carrier transportation into local strongly localized states in bright regions, as shown in Figure 5.25(a), or is mainly quenched both by carrier transportation into local strongly localized states and by nonradiative recombination in dark regions, as shown in Figure 5.25(c); the slow decay lifetime τ_2 actually corresponds to carrier localization in local strongly localized states, as shown in Figure 5.25(b) and (d).
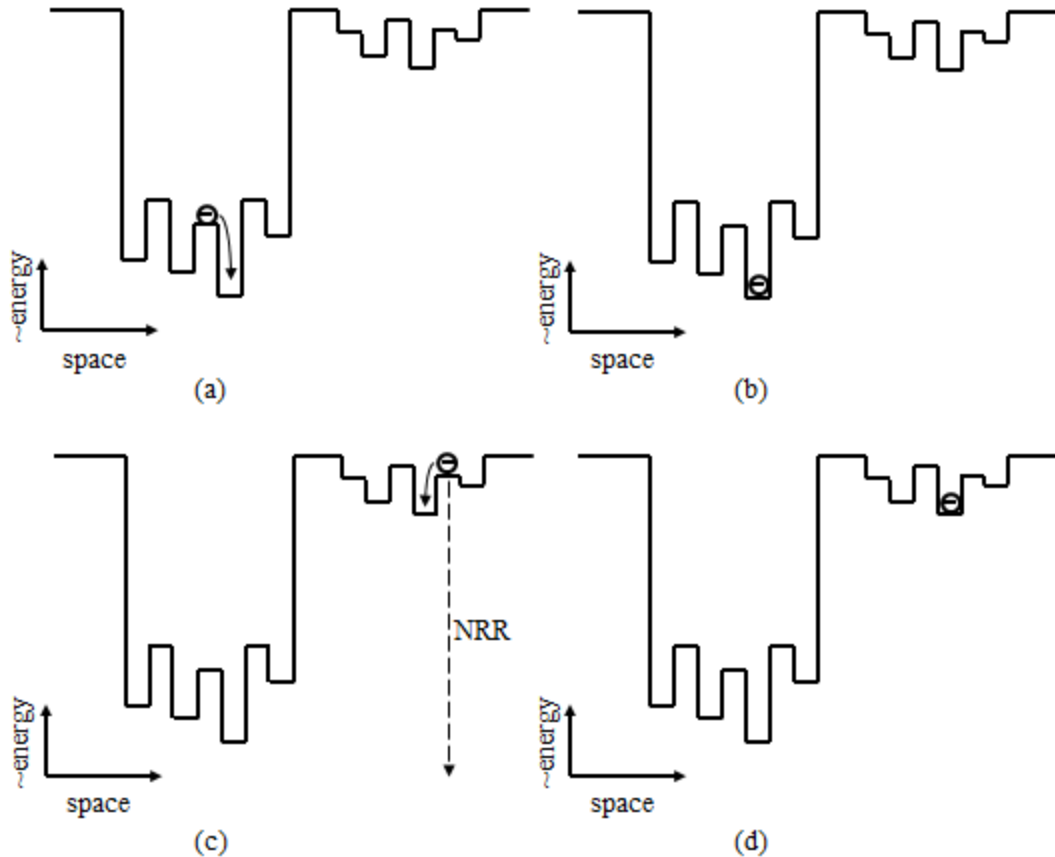
Figure 5.25: Bandgap energy fluctuations in small-bandgap-energy region and large-bandgap-energy region, carrier localization in local weakly localized states (a)(c), and carrier localization in local strongly localized states (b)(d).

It should be noted that the large-scale small-bandgap-energy region (strongly localized state) and large-bandgap-energy region (weakly localized states) are actually related with the two nonradiative channels that were introduced in Section 5.1.1. The first nonradiative channel corresponds to the thermal activation of carriers out of the large-scale small-bandgap-energy regions (strongly localized states), which is in consistence with the channel's large rate constant A, since the probability of nonradiative recombination is increased outside the small-bandgap-energy region. The second nonradiative channel, on the other hand, corresponds to the thermal activation of carriers out of the large-scale large-bandgap-energy regions (weakly localized states). Since in the

large-scale large-bandgap-energy region carriers are weakly localized and have long diffusion length, they have large probability of nonradiative recombination no matter they are activated out of the large-scale large-bandgap-energy region (weakly localized states) or not, which explains the reason for the small rate constant B of the second nonradiative channel.

Table 5.4 and Figure 5.26 show that the bright region has a long slow decay lifetime τ_2 than the dark region does. Since the slow decay lifetime τ_2 is related with radiative lifetime (τ_r) and nonradiative lifetime (τ_{nr}) for the relation:

$$\frac{1}{\tau_2} = \frac{1}{\tau_r} + \frac{1}{\tau_{nr}}. \tag{5.15}$$

And the radiative lifetime can be calculated as [58]

$$\tau_r \propto \frac{\mu(m_0\varepsilon_r a_H / \mu)^2}{4h^2} \cdot \frac{M}{\mu} \cdot \frac{\Delta(T)}{1-\exp(-\Delta(T)/k_B T)} \text{ and } \tau_{nr} = \frac{1}{sN_T\sqrt{8k_B T / \pi m^*}}, \tag{5.16}$$

where $E_B^{2D} = 4h^2/\mu\left(a_0^{2D}\right)^2$ is the quasi 2D exciton binding energy, $a_0^{2D} = \left(m_0\varepsilon_r / \mu\right)a_H$ is the 2D exciton Bohr radius, μ is the reduced mass $\mu^{-1} = \left(m_e^*\right)^{-1} + \left(m_h^*\right)^{-1}$, $M = m_e^* + m_h^*$, m_0 is the free electron mass, ε_r is the relative permittivity, a_H is the Bohr radius of the hydrogen atom, k_B is Boltzmann constant, and $\Delta(T)$ is the exciton linewidth at finite temperature. The radiative lifetime in both bright region and dark region are close to the same. So the bright region has longer τ_{nr} than the dark region does, indicating higher quenching of radiative recombination in strongly localized state in large-bandgap-energy dark regions.
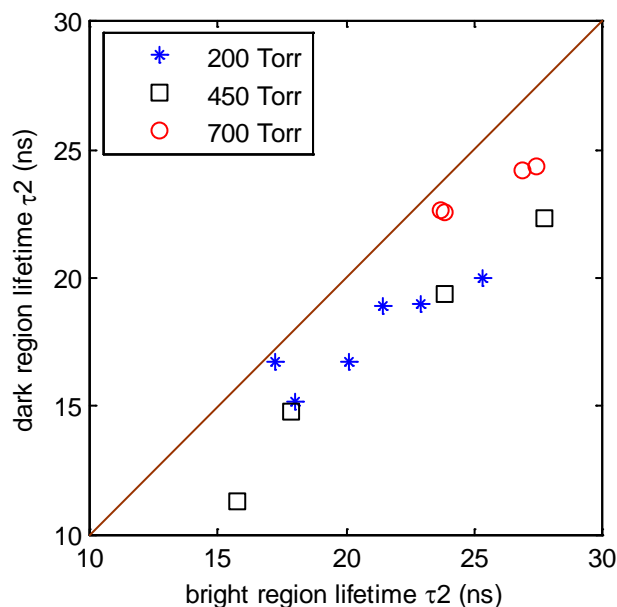
Figure 5.26: Dark region slow decay lifetime τ_2 vs. bright region slow decay lifetime τ_2. Solid line shows the place where dark region lifetime equals bright region lifetime.

The higher PL intensity and longer slow decay lifetime τ_2 of bright regions are consistent with a higher probability of radiative recombination in bright regions, while the lower PL intensity and shorter slow decay lifetime τ_2 of dark regions consist with a higher probability of nonradiative recombination through NRRCs in the dark region and/or carrier transportation from dark regions to bright regions.

It is also noted that the bright region slow decay lifetime τ_2 increases with the increase of the bandgap energy difference, as shown in Figure 5.27(a). This is likely the result of stronger carrier localization. Since carrier escape is one factor that can cause localized carrier's nonradiative loss and quenches the radiative recombination process, with larger bandgap energy difference, the probability of carrier escape is reduced and carriers' nonradiative loss is reduced, so a longer carrier lifetime is expected. On the other hand, the longer bright region slow decay lifetime τ_2 can also be understood as the result of the larger bright region bandgap energy, as illustrated in Figure 5.26(b). Larger

bright region bandgap energy, which is introduced by thinner QW layer thickness or smaller indium composition, corresponds to smaller piezoelectric field and smaller QCSE, which reduces the separation of electron wavefunction and hole wavefunction, resulting in higher probability of recombination, and consequently leading to smaller slow decay lifetime τ_2.
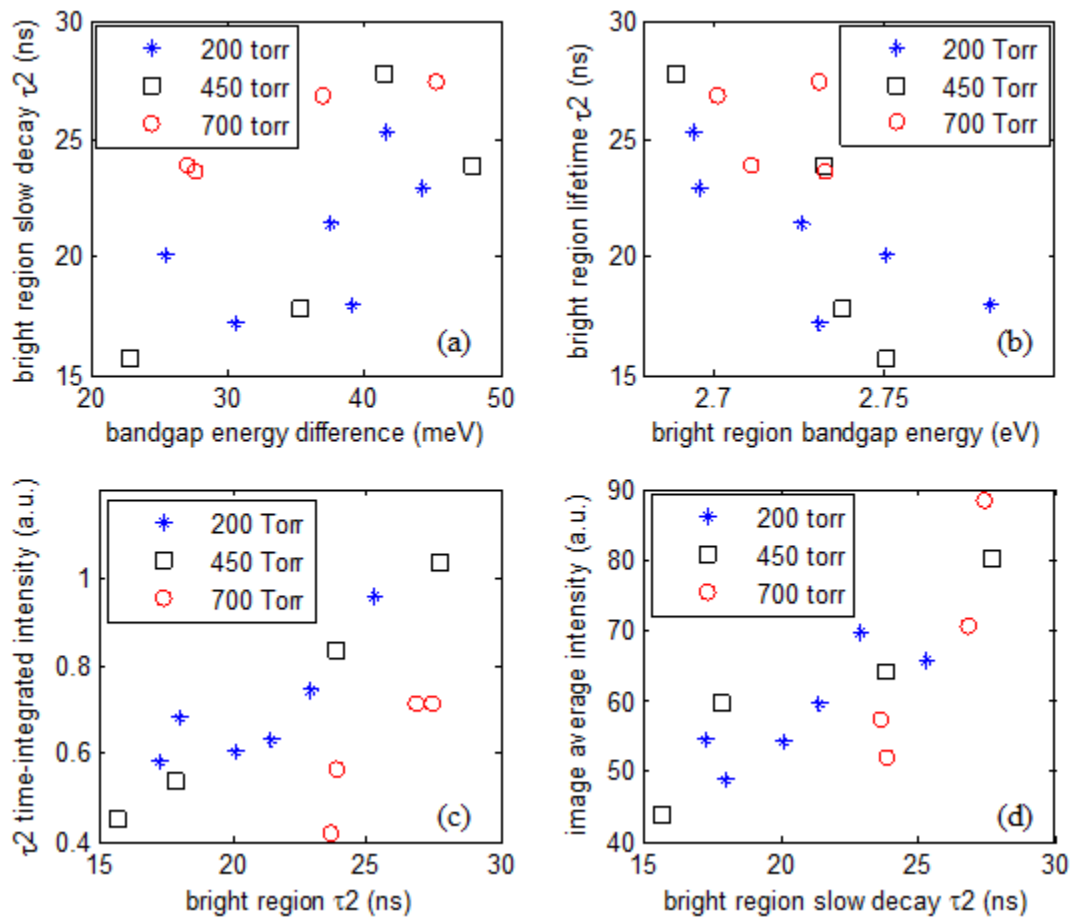
Figure 5.27: (a) CLSM image average intensity vs. bright region slow decay lifetime $\tau2$; (b) Time-integrated PL intensity vs. bright region slow decay lifetime $\tau2$; (c) Bright region slow decay lifetime $\tau2$ vs. bandgap energy difference; (d) Bright region lifetime $\tau2$ vs. bright region bandgap energy.

Since τ_1 time-integrated intensity, which is calculated by

$$\tau_1 \text{ time-integrated intensity} = \int_0^{+\infty} I_1 \exp(-\frac{t}{\tau_1})dt = I_1\tau_1, \quad (5.17)$$

is around an order of magnitude smaller than the τ_2 time-integrated intensity, which is calculated by

$$\tau_2 \text{ time-integrated intensity} = \int_0^{+\infty} I_2 \exp(-\frac{t}{\tau_2})dt = I_2\tau_2, \quad (5.18)$$

the PL intensity is mainly contributed by the slow decay process. Moreover, since the radiative recombination mainly takes place in small-bandgap-energy bright regions, the slow decay lifetime τ_2 in bright region tends to identify the overall optical quality of MQWs. Figure 5.27(c) shows that the CLSM image average intensity increases with the increase of bright region slow decay lifetime τ_2. This is because the τ_2 time-integrated PL intensity increases with the increase of τ_2, as shown in Figure 5.26(d), and that the image average intensity is actually the space-average of this time-integrated PL intensity. In addition, as indicated in Figure 5.27(a), longer bright region slow decay lifetime corresponds to larger bandgap energy difference. Previous analysis has shown that larger bandgap energy difference results in stronger carrier localization effect and higher CLSM image average intensity. The combination of these two factor also leads to the fact that longer bright region slow decay lifetime τ_2 corresponds to larger CLSM image average intensity.

Table 5.4: TRPL data for group 2 samples

Sample ID	Bright region				Dark region			
	Fast decay lifetime τ1 (ns)	τ1 time-integrated intensity	Slow decay lifetime τ2 (ns)	τ2 time-integrated intensity	Fast decay lifetime τ1 (ns)	τ1 time-integrated intensity	Slow decay lifetime τ2 (ns)	τ2 time-integrated intensity
#7	1.42	0.071032	22.94	0.744411	1.31	0.068956	18.97	0.568668
#8	1.33	0.055609	17.99	0.682145	1.38	0.068768	15.17	0.500695
#9	1.10	0.061691	20.11	0.606756	0.96	0.056132	16.77	0.510386
#10	1.30	0.063726	17.25	0.581049	1.30	0.066791	16.75	0.548389
#11	1.87	0.091927	21.41	0.632304	2.07	0.106597	18.88	0.516094
#12	1.95	0.077037	25.31	0.957108	1.87	0.083999	20.00	0.661652
#13	1.31	0.070495	17.86	0.539075	1.38	0.090785	14.82	0.304905
#14	2.69	0.099982	27.75	1.033214	2.49	0.094747	22.31	0.778571
#15	1.18	0.06749	15.72	0.451306	1.28	0.075193	11.31	0.303319
#16	1.80	0.07898	23.87	0.837917	1.91	0.093188	19.34	0.577396
#17	2.08	0.090979	26.85	0.712331	2.82	0.140404	24.17	0.452946
#18	1.53	0.086505	23.85	0.56656	1.63	0.098355	22.57	0.391785
#19	2.17	0.111647	27.44	0.713342	2.34	0.127229	24.34	0.52899
#20	1.24	0.084245	23.67	0.421058	1.68	0.110833	22.63	0.239199

5.3 CLSM Imaging and Growth Parameters Analysis

5.3.1 CLSM Imaging

A third group of 10 blue-emitting InGaN/GaN MQW samples are analyzed. These samples are grown under 5 different pressure regimes: 100 Torr, 200 Torr, 450 Torr, 500 Torr, and 700 Torr. Similar as the samples in Section 5.2, these samples are grown on the same GaN templates and have same MQW structure. However, different from the samples in Section 5.2, these samples were grown with one growth parameter being tuned while all other parameters being kept unchanged. In this case, it is possible to analyze the effect of growth parameters on the bandgap energy difference and average PL intensity. The primary growth parameters (growth pressure, In/Ga ratio and N_2/NH_3 ratio) used during the sample growth are listed in Table 5.5.

Table 5.5: Parameters used in MOCVD growth

Sample ID	Growth pressure (Torr)	In/Ga ratio (molar)	N_2/NH_3 (slm)	Notes
#21	200	1.5	72/40	Standard
#22	200	2.5	72/40	Increase In/Ga
#23	100	1.5	30/50	Low P, high NH_3
#24	700	1.5	200/50	High P, low GR
#25	100	1.5	50/30	Low P, low NH_3
#26	500	1.5	170/30	High P, low NH_3
#27	700	1.5	200/30	High P, low NH_3
#28	700	1.5	200/50	High P, high GR
#29	450	1.7	225/50	Low T
#30	450	1.7	225/50	High T

Figure 5.28 shows the ensemble PL spectra of the samples, from which a variation of PL intensity and a stronger yellow luminescence can be seen. The stronger yellow luminescence is because that an old NH_3 source was used during the growth, which introduced a lot of H_2O contamination.

Figure 5.29 and Figure 5.30 show the CLSM images for the samples, taken with both 445/40 nm BPF and 538 nm LPF. Similar as what was shown in Figure 5.13, the CLSM images taken with BPF showed inhomogeneous distribution of PL intensities in micrometer scale. However, different from Figure 5.14, which shows almost nothing, in Figure 5.30 the CLSM images taken with 538 nm LPF show a lot of features: "dots" that are around 500 nm in diameter can clearly be seen. PL spectrum taken on the dots show luminescence peak at around 550 nm, as shown in Figure 5.31, which agrees with the stronger yellow luminescence in ensemble PL spectra of these samples, indicating that these dots are yellow luminescence dots.

These yellow luminescence dots are from the threading edge dislocations in combination with C, H, O [125] or Ga vacancies [126]. A proof of this is that a z-scan shows that the yellow luminescence dots are visible in a vertical range of at least 3.1 μm, which is about the total thickness of the MQWs and the GaN buffer layers, as shown Figure 5.32.
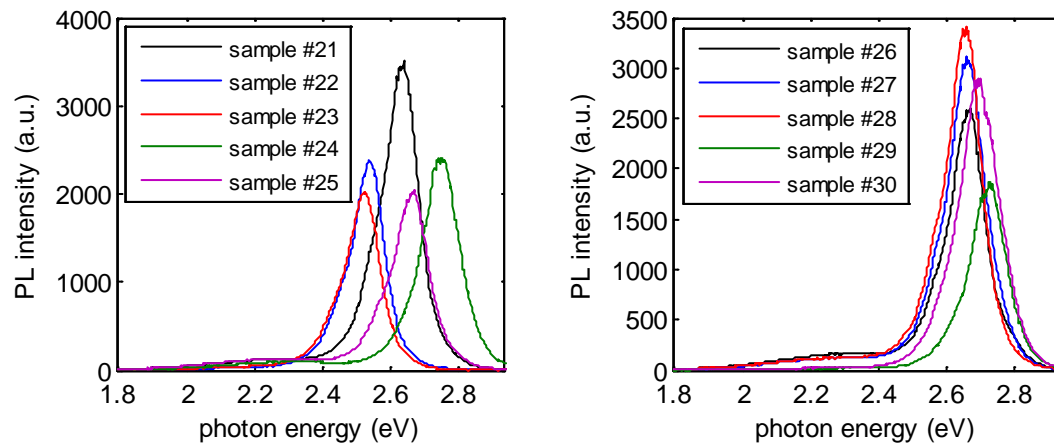
Figure 5.28: Ensemble PL spectra of sample #21 to #30. Excited by 325 nm HeCd laser.
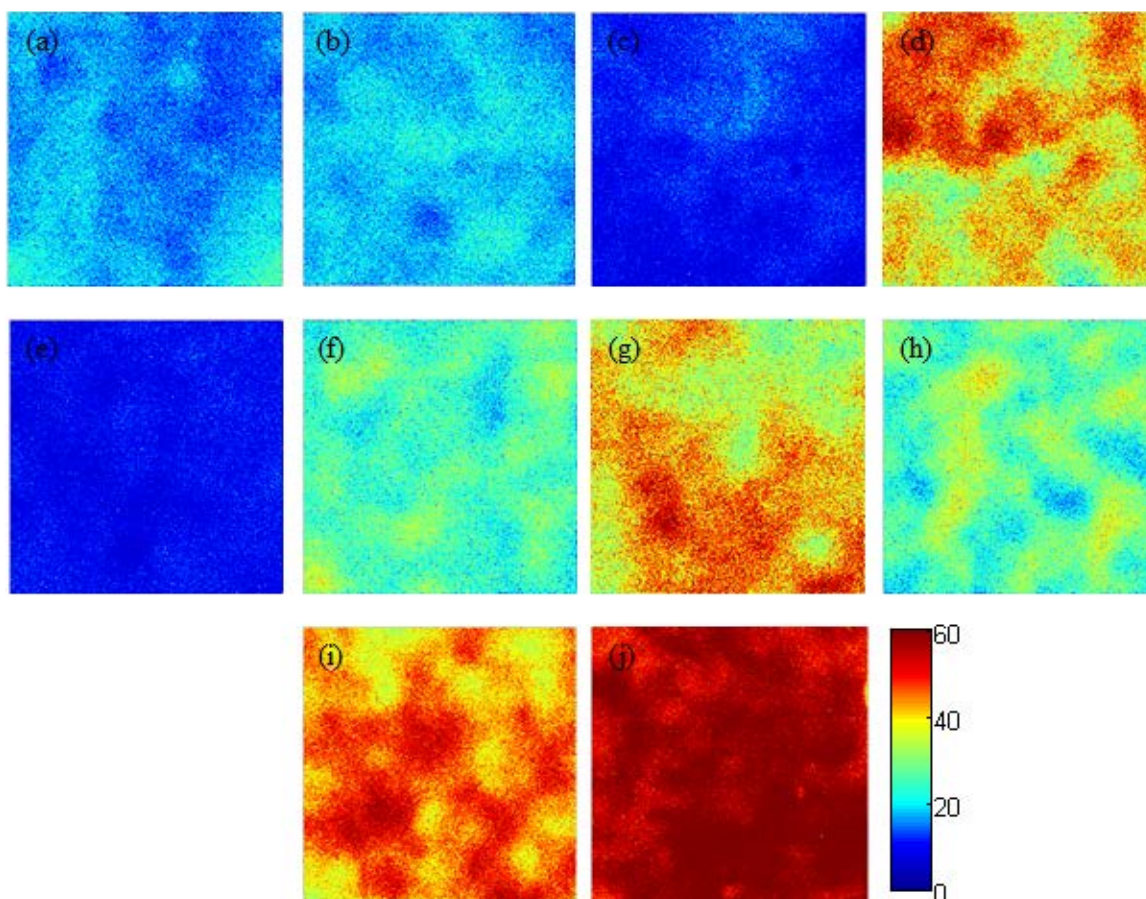
Figure 5.29: (Color) CLSM images taken with 445/40 nm BPF. Figures (a)-(j) correspond to sample #21-#30. All images are 20μm×20μm in size.
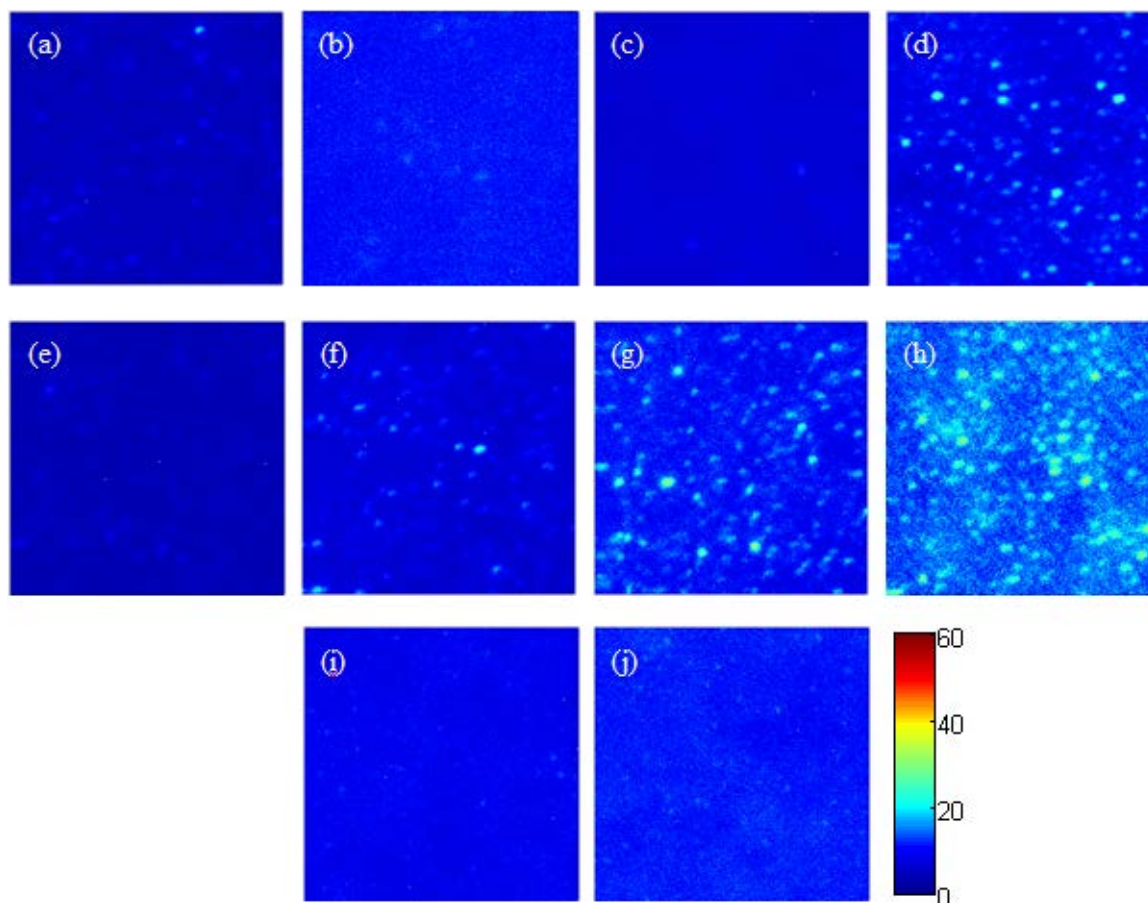
Figure 5.30: (Color) CLSM images taken with 538 nm LPF, at the same place where Figure 5.29 was taken. Figures (a)-(j) correspond to sample #21-#30. All images are 20μm×20μm in size.
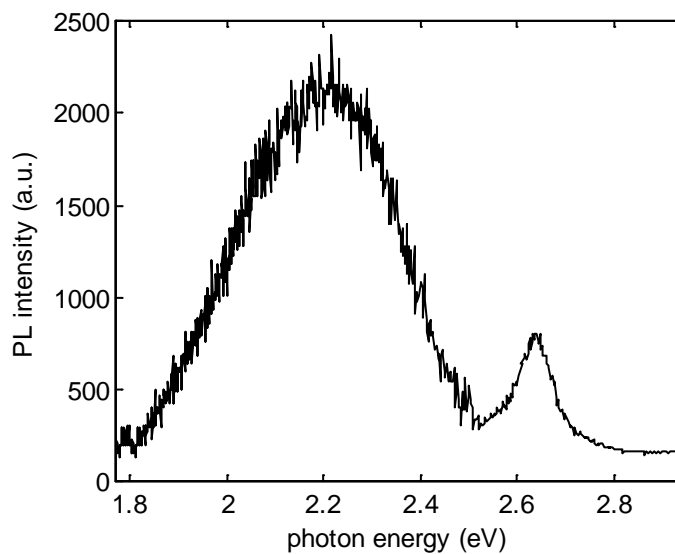
Figure 5.31: PL spectrum of sample #21 at yellow dot. The primary peak at 550 nm indicates yellow luminescence. The secondary peak at around 460 nm is from bandedge emission light which is not totally blocked by the LPF.
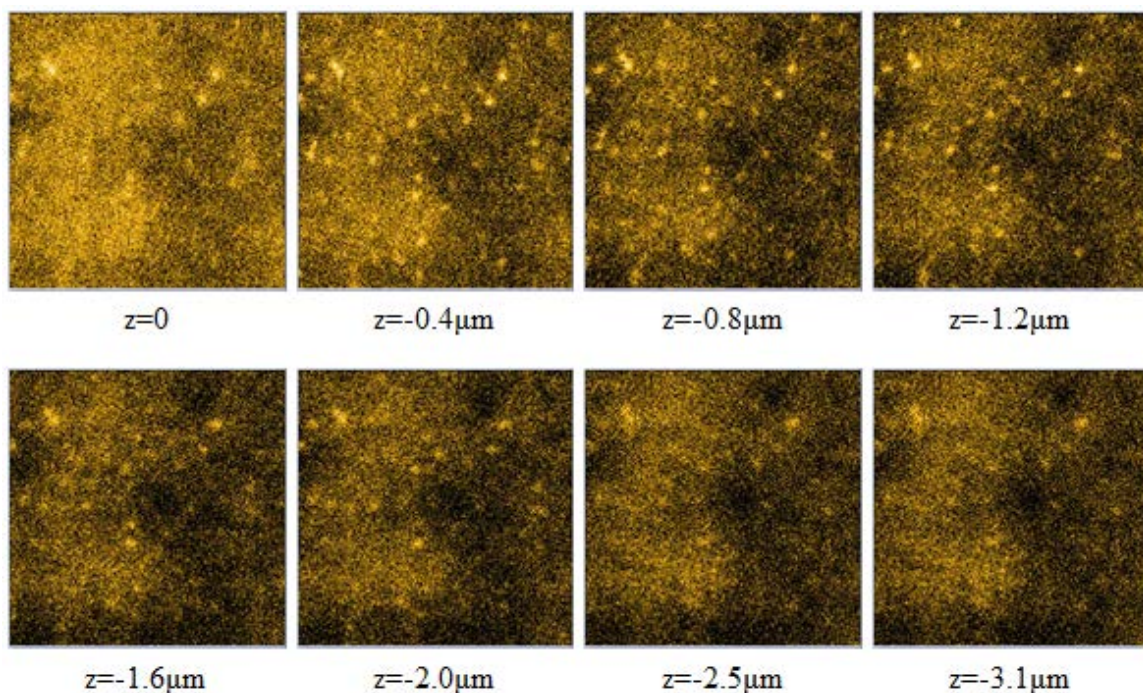
Figure 5.32: z-scan of with 538 nm LPF. z=0 means the focal point is at the sample surface; z=-3.1 μm means the focal point is 3.1 μm inside the sample.

It is reasonable to assume that there should be a dark spot in the CLSM image taken with BPF at the place where the corresponding CLSM image taken with LFP shows

a yellow luminescence dot, since carriers contribute to yellow luminescence rather than bandedge emission. However, as can be seen from Figure 5.29, the bandedge emission CLSM images do not show any dark dots that correspond to the yellow luminescence dots at all. This is because the CLSM system has lateral resolution of 200 nm, which enlarges any features by 200 nm on their edges. As a result, when imaging with LPF, the yellow luminescence features are enlarged, indicating that the real yellow luminescence features are smaller than the 500-nm-diameter dots; on the other hand, when imaging with BPF, the enlarged bandedge luminescence overlays the small yellow luminescence features, making it invisible.

Comparing Figure 5.29 with Figure 5.30, it is seen that the visible yellow luminescence dots are mainly distributed in bright regions. This is the result of the higher carrier concentration in small-bandgap-energy bright regions. In bright regions a huge number of carriers can contribute to yellow luminescence, while in dark regions few carriers can contribute to yellow luminescence.

The bandgap energy difference between bright and dark regions, the CLSM image average intensity, and the PL peak intensity ratio between bright and dark regions for the samples are all listed in Table 5.6.

5.3.2 Effect of Growth Parameters

To study the effect of growth parameters on the PL brightness of MQW samples, the samples introduced before were divided into several groups according to their growth conditions, as listed in Table 5.6.

5.3.2.1 The Effect of Pressure

In group A, three samples were grown under three different pressures but all other growth parameters were kept the same. Since increasing growth pressure increases the indium incorporation into the samples, in order to keep the sample's PL peak energy constant, growth temperature was also adjusted also. Table 5.6 shows that for samples grown at higher pressure, its bright region PL peak is more red-shifted compared with its dark region PL peak, and its PL peak intensity ratio is higher, indicating a stronger localization effect, which is because that higher growth pressure reduces the number of vacancies and leads to better crystal quality [127]. This explains why sample's average PL intensity becomes larger with the increment of sample's growth pressure. As a result, increasing growth pressure may increase bandgap energy difference between bright and dark regions and the extent of carrier localization in the quantum well layer, and consequently, increase the sample average PL intensity.

According to the analysis in previous section, Sample #27, which was grown at highest pressure and had largest bandgap energy difference, should have most visible yellow luminescence dots since most carriers are localized in small-bandgap-energy regions. However, Table 5.6 shows that all three samples have similar number of visible yellow luminescence dots. This is because the sample grown at higher pressure has fewer vacancies. So the effect of carrier localization cancels the effect of better crystal quality, resulting similar number of visible yellow luminescence dots.

5.3.2.2 The Effect of Growth Rate

Group B shows two samples grown with different growth rate. Sample #28, grown with higher growth rate, has relatively smaller ensemble PL peak energy,

indicating higher indium incorporation with higher growth rate. This increased indium incorporation is because at higher growth rate the indium atoms are trapped by the new growing layer so that their tendency to leave the crystal, due to InN decomposition and In atom evaporation, is suppressed [128].

Sample #28 has sample average PL intensity that is 2/3 smaller than sample #24 does. This can be attributed to the low crystal quality as a result of high growth rate. On the other hand, this can also be explained by the fact that samples #28 has smaller bandgap energy difference than sample #24 does.

Table 5.6: Effect of growth pressure, growth rate, and growth temperature

Sample ID	Group A			Group B		Group C	
	#25	#26	#27	#28	#24	#29	#30
	Increased growth pressure			Reduced growth rate		Increased growth temperature	
Ensemble PL peak energy (eV)	2.661	2.684	2.690	2.719	2.756	2.728	2.694
CLSM image average intensity (a.u.)	15	31	57	22	66	54	80
Number of visible yellow luminescence features	58	57	59	71	72	62	70
Bright region bandgap (eV)	2.670	2.675	2.665	2.694	2.673	2.731	2.689
Dark region bandgap (eV)	2.689	2.696	2.696	2.713	2.716	2.768	2.731
Bandgap energy difference between bright-and-dark region (meV)	19.1	21.5	31	19.4	43.4	37.7	41.5
Bright region PL peak intensity (a.u.)	4018	5371	8576	4429	11718	3991	4387
Dark region PL peak intensity (a.u.)	1909	2413	3383	2138	3110	1202	1225
PL peak intensity ratio between bright-and-dark region	2.1	2.22	2.54	2.07	3.77	3.32	3.58
CLSM image standard deviation	4.04	6.10	8.81	5.56	8.40	8.25	9.58

It is seen that the growth rate does not affect the number of visible yellow luminescence dots. This is because even though sample #24 has larger bandgap energy difference, the low growth rate of sample #24 results in better crystal quality (less defects and vacancies). As a result, the effect of better crystal quality cancels the effect of larger bandgap energy difference, leading to similar number of visible yellow luminescence features.

5.3.2.3 The Effect of Growth Temperature

In group C two samples were grown under the same conditions except that the growth temperature of sample #29 was lower than the growth temperature of sample #30. It is seen that the ensemble PL peak energy of sample #29 is smaller than that of sample #30. This is because InN has very poor thermal stability and dissociates easily at high temperature, which reduces the indium incorporation in the quantum well layer grown at high temperature, as mentioned in Section 2.1.2. For sample #30 which was grown at higher temperature and as a result better crystal quality [34], there is larger bandgap energy difference, so higher average PL intensity is expected, as shown in Table 5.6.

Similar as previous condition, the effect of better crystal quality cancels the effect of larger bandgap energy difference, so changing the growth temperature does not affect the number of visible yellow luminescence features too much.

5.3.2.4 The Effect of Effective V/III Ratio and Effective Gas Speed

As shown in Table 5.2, the definition of effective V/III ratio (V/III*) and effective gas speed (S*) allows us to compare growth conditions over a wide process space. For easy comparison, some data from Table 5.2 and Table 5.3 are listed in Table 5.7.

Table 5.7: Effect of V/III* and S*

Sample ID	Group D		Group E		Group F		Group G	
	#13	#16	#15	#16	#8	#7	#19	#20
Condition	450 Torr S* same V/III* increases		450 Torr S* increases V/III* increases		200 Torr S* increases V/III* increases		700 Torr S* same V/III* increases	
CLSM image average intensity (a.u.)	60	64	44	64	49	70	88	57
Bandgap energy difference (meV)	35.3	47.9	22.8	47.9	39.1	44.2	45.3	27.6
PL peak intensity ratio	3.27	3.79	2.93	3.79	3.06	3.27	4.12	3.23
CLSM image standard deviation	8.38	8.48	7.52	8.48	3.27	8.78	9.71	8.9

In group D, two samples grown at 450 Torr, sample #13 and sample #16, have same effective gas speed while the effective V/III ratio for sample #16 is much larger than that for sample #13. Table 5.7 shows that the higher effective V/III ratio of sample #16 led to larger bandgap energy difference between bright region and dark region and consequently larger average PL intensity. Similarly, sample #16 was grown under both higher effective V/III ratio and higher effective gas speed than sample #15, and sample #7 was grown under both higher effective V/III ratio and higher effective gas speed than sample #8. Larger bandgap energy difference and higher average PL intensity are observed for sample #16 and #7, comparing with sample #15 and #8, respectively. So at 200 Torr and 450 Torr growth pressures, higher effective V/III ratio results in larger bandgap energy difference, stronger carrier localization, and stronger average PL intensity, as a result of increased NH_3 decomposition.

On the other hand, in group G, sample #20, which was grown with higher effective V/III ratio than sample #19 and almost the same effective gas speed as sample #19, shows much smaller bandgap energy difference and average PL intensity than

sample #19 does, indicating that at 700 Torr growth pressure, increasing the effective V/III ratio does not result in higher bandgap energy difference and improved PL intensity, but reduces bandgap energy difference and the PL intensity, unlike the cases for 200 Torr and 450 Torr growth pressures. This is because the parasitic gas-phase reactions, which occur between TEGa, TMIn and NH_3 before they reach the growth surface, are amplified at high growth pressure as a result of the high gas density. The gas-phase reactions consume the reactants, change the ratio of chemical adducts adsorbed onto the growth surface, and create particles on the growth surface, resulting in poor crystal quality of the MQW sample. To lessen the gas phase reaction, increasing the effective gas speed is necessary, so that the time needed for reactants to reach the growth surface after mixture is reduced. Figure 5.33 shows that as the effective gas speed is increased, larger bandgap energy difference and higher average PL intensities can be obtained, indicating that higher optical quality material can be realized. In Figure 5.33 the drop in average PL intensity for the 700 Torr MQWs in not entirely unexpected; due to the geometrical limitations in the reactor and injector design, the system was not meant to work at pressure as high as 700 Torr, so it is very difficult to obtain laminar and stable streamlines. Figure 5.33 also shows that the strongest PL intensity samples are obtained at higher growth pressure (450 Torr and 700 Torr), which could not be achieved at 200 Torr growth pressure, even after process optimization. This agrees with our previous analysis on the effect of growth pressure.
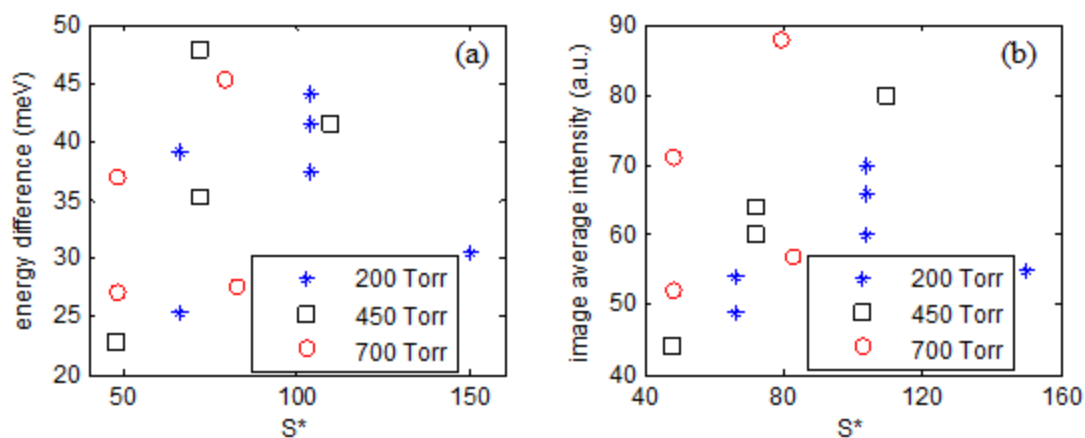
Figure 5.6: (a) Bandgap energy difference and (b) CLSM image average intensity as a function of effective gas speed (S^*) for sample #7 to sample #20. Note the highest intensity samples are at 450 Torr and 700 Torr.

As a result, at low growth pressures (200 Torr and 450 Torr), increasing the effective V/III ratio and increasing effective gas speed may increase the bandgap energy difference of the MQW sample, resulting in higher average PL intensity. In contrary, at high growth pressure (700 Torr), parasitic gas-phase reaction can dominate. In this case, increasing the effective V/III ratio may reduce quality of the material, reduce the bandgap energy difference and result in low average PL intensity. At any growth pressure, the gas-phase reaction can be suppressed with high effect gas flow rate, which decrease the gas resident time and improve the overall PL intensity.

5.4 Summary and Conclusion

In this chapter, different techniques, including temperature dependent PL spectroscopy, confocal microscopy, and TRPL spectroscopy, are applied to analyze the bandgap energy fluctuation, carrier localization, and carrier dynamics in blue-emitting InGaN/GaN MQWs.

In temperature dependent PL spectroscopy, the Arrhenius equation was used to analyze the temperature-dependent spectrum-integrated PL intensity. The analysis

showed that the spectrum-integrated PL intensity was quenched by two nonradiative channels, in which the one with higher activation energy corresponded to thermal activation of carriers out of the strongly localized states, and the one with lower activation energy corresponded to thermal activation of carriers out of the weakly localized states. The S-shaped shift of PL peak energy and the inverse S-shaped shift of PL FWHM were also observed with increasing temperature, which were then explained with carrier localization and carrier dynamics.

In confocal microscopy, CLSM images and nanometer-scale PL spectra were taken on MQWs. Laterally inhomogeneous distribution of PL intensity was observed in micrometer scale. The measurements showed that the bright region had smaller bandgap energy than the dark region did, so that carriers are localized in small-bandgap-energy regions and their probability of meeting NRRCs is reduced.

The experiments showed that in this research the TDs surrounded by V-pits did not contribute to nonradiative recombination, as no MQWs were grown on the sidewall of the V-pits.

TRPL spectroscopy and double exponential curve fitting showed that both bright region and dark region are characterized by two lifetimes: the fast decay lifetime was smaller than 3 ns, and corresponded to carrier localization in weakly localized state, where radiative recombination was more quenched by NRRCs and also competed with carrier transportation into strongly localized states, while the slow decay with lifetime τ_2 was longer than 10 ns and corresponded to carrier localization in strongly localized states. Since both two lifetimes were observed in both bright region and dark region, it was concluded that inside bright/dark region there were also bandgap energy fluctuations in

nanometer length scale. Moreover, it was found out that the slow decay lifetime in bright region was longer than the slow decay lifetime in dark region, indicating higher probability of nonradiative recombination in dark region and/or carrier transportation from dark regions to bright regions.

The experiments showed that the larger the bandgap energy difference is, the larger the sample average PL intensity is, the less uniform the lateral PL intensity distribution is, and the longer the bright region slow decay lifetime is.

Finally, the influence of growth parameters on MQW sample bandgap energy difference, carrier localization, and average PL intensity were analyzed. It was found that by increasing growth pressure, reducing growth rate, increasing growth temperature, increasing effective V/III ratio (for low growth pressure) or increasing effective gas speed, it was possible to increase the bandgap energy difference, resulting in stronger carrier localization and larger room-temperature average PL intensity.

CHAPTER 6: CONCLUSION AND SUGGESTIONS FOR FUTURE RESEARCH

The research about bandgap energy fluctuation and carrier localization in InGaN/GaN MQWs in this dissertation has made several advances in understanding the bandgap energy fluctuation and carrier localization in blue-emitting InGaN/GaN MQWs.

In temperature dependent PL spectroscopy, the decrease of spectrum-integrated PL intensity with increasing temperature was analyzed with Arrhenius equation. The analysis indicated two nonradiative channels that can quench the spectrum-integrated PL intensity. The first channel with larger activation energy corresponded to thermal activation of carriers out of the strongly localized states, and the second channel with smaller activation energy corresponded to thermal activation of carriers out of the weakly localized states. The S-shaped shift of PL peak energy and the inverse S-shaped shift of PL FWHM with increasing temperature were explained using carrier localization in localized states and carrier dynamics.

In confocal microscopy, the lateral fluctuation of PL peak intensity and PL peak energy was observed in hundreds of nanometer to micrometer scale. The bandgap energy in bright regions was generally tens of meV smaller than the bandgap energy in dark regions, and the bright region was at least twice at bright at dark region. This showed that carriers were localized in bright regions and were diffusion limited, which reduced their chance to meet NRRCs. The NRRCs were probably point defect, vacancies, stacking faults, or TDs that were not surrounded by V-pits. TDs surrounded by V-pits, however,

could not contribute to nonradiative recombination. The effect of the carrier localization was observed: the larger the bandgap energy difference between bright region and dark region was, the larger the sample average PL intensity was, the brighter the small-bandgap-energy region was compared with the large-bandgap-energy region, and the less uniform the lateral PL intensity distribution became.

Through nanometer-scale TRPL spectroscopy, it was found out that both bright region and dark region were characterized by two lifetimes: the fast decay lifetime (<3 ns) corresponded to carrier localization in weakly localized states, where radiative recombination was more quenched by NRRCs and also competed with carrier transportation into strongly localized states, while the slow decay lifetime (>10 ns) corresponded to carrier localization in strongly localized states. The fact that both lifetimes occurred in both bright region and dark region showed that there were bandgap energy fluctuations in nanometer-scale (local weakly localized states and local strongly localized states) inside bright/dark region. Carriers not only transported from dark region (large-scale weakly localized states) to bright region (large-scale strongly localized states), but also transported from local weakly localized states to local strongly localized states inside the bright/dark region.

The influence of some growth parameters on MQW sample bandgap energy fluctuation and average PL intensity were also analyzed in this research. Research showed that larger bandgap energy difference and average PL intensity can be achieved by increasing the growth pressure, reducing growth rate, increasing growth temperature, increasing effective V/III ratio (for low growth pressure) or increasing effective gas speed.

In this research, due to the limitation of available experiment devices, the PL spectra and TRPL spectra was only taken at several pixels in the CLSM image. A PL spectra or TRPL spectra at each pixel in the CLSM image is able to tell more about the properties of the bandgap energy fluctuation.

Although it has been mentioned in this research that a large quantum well layer thickness fluctuation could result in large bandgap energy fluctuation and high IQE, a too large QW thickness fluctuation could lead to a rough surface, which decreases the EQE (external quantum efficiency) since the light extraction is reduced. Moreover, the bandgap energy fluctuation can increase the IQE only under limited excitation density. At high excitation density, when the confining potential is filled, it cannot further localize other carriers. In this case, the un-localized carriers are able to diffuse freely as if there is no confining potential at all, and reach NRRCs. This phenomenon is called "efficiency droop". In this case, a further analysis of the band-filling and efficiency droop is necessary.

A new high-pressure MOCVD system has recently been built in the Stokes' group for the growth of high quality InGaN/GaN MQWs. A detailed analysis of the high-pressure grown InGaN/GaN MQWs with the techniques introduced in this research would benefit the understanding of high-pressure MOCVD tool and achieving high quality InGaN/GaN MQWs.

REFERENCES

1. Chichibu, S.F., et al., *Origin of defect-insensitive emission probability in In-containing (Al, In, Ga) N alloy semiconductors.* Nature Materials, 2006. **5**(10): p. 810-816.

2. Nakamura, S., et al., *High-Brightness Ingan Blue, Green and Yellow Light-Emitting-Diodes with Quantum-Well Structures.* Japanese Journal of Applied Physics Part 2-Letters, 1995. **34**(7A): p. L797-L799.

3. Nakamura, S., *The roles of structural imperfections in InGaN-Based blue light-emitting diodes and laser diodes.* Science, 1998. **281**(5379): p. 956-961.

4. Wang, J.X., et al., *Study on internal quantum efficiency of blue InGaN multiple-quantum-well with an InGaN underneath layer.* Science China-Technological Sciences, 2010. **53**(2): p. 306-308.

5. Herzog, A.H., D.L. Keune, and M.G. Craford, *High-Efficiency Zn-Diffused Gaas Electroluminescent Diodes.* Journal of Applied Physics, 1972. **43**(2): p. 600-&.

6. Hitzel, F., et al., *Correlation of defects and local bandgap variations in GaInN/GaN/AlGaN LEDs.* Physica Status Solidi B-Basic Research, 2001. **228**(2): p. 407-410.

7. Narukawa, Y., et al., *Role of self-formed InGaN quantum dots for exciton localization in the purple laser diode emitting at 420 nm.* Applied Physics Letters, 1997. **70**(8): p. 981-983.

8. Galtrey, M.J., et al., *Compositional inhomogeneity of a high-efficiency In(x)Ga(1-x)N based multiple quantum well ultraviolet emitter studied by three dimensional atom probe.* Applied Physics Letters, 2008. **92**(4).

9. van der Laak, N.K., et al., *Role of gross well-width fluctuations in bright, green-emitting single InGaN/GaN quantum well structures.* Applied Physics Letters, 2007. **90**(12).

10. Galtrey, M.J., et al., *Three-dimensional atom probe analysis of green- and blue-emitting In(x)Ga(1-x)N/GaN multiple quantum well structures.* Journal of Applied Physics, 2008. **104**(1).

11. Galtrey, M.J., et al., *Atom probe revels the structure of InxGe1-xN based quantum wells in three dimensions.* Physica Status Solidi B-Basic Solid State Physics, 2008. **245**(5): p. 861-867.

12. Oliver, R.A., M.J. Galtrey, and C.J. Humphreys, *High resolution transmission electron microscopy and three-dimensional atom probe microscopy as complementary techniques for the high spatial resolution analysis of GaN based quantum well systems.* Materials Science and Technology, 2008. **24**(6): p. 675-681.

13. Narayan, J., et al., *Effect of thickness variation in high-efficiency InGaN/GaN light-emitting diodes.* Applied Physics Letters, 2002. **81**(5): p. 841-843.

14. Kwon, S.Y., et al., *Optical and microstructural studies of atomically flat ultrathin In-rich InGaN/GaN multiple quantum wells.* Journal of Applied Physics, 2008. **103**(6).

15. Sonderegger, S., et al., *High spatial resolution picosecond cathodoluminescence of InGaN quantum wells.* Applied Physics Letters, 2006. **89**(23).

16. Kaneta, A., M. Funato, and Y. Kawakami, *Nanoscopic recombination processes in InGaN/GaN quantum wells emitting violet, blue, and green spectra.* Physical Review B, 2008. **78**(12).

17. Jeong, M.S., et al., *Spatially resolved photoluminescence in InGaN/GaN quantum wells by near-field scanning optical microscopy.* Applied Physics Letters, 2001. **79**(7): p. 976-978.

18. Jeong, M.S., et al., *Spatial variation of photoluminescence and related defects in InGaN/GaN quantum wells.* Applied Physics Letters, 2001. **79**(21): p. 3440-3442.

19. Kaneta, A., et al., *Spatial and temporal luminescence dynamics in an InxGa1-xN single quantum well probed by near-field optical microscopy.* Applied Physics Letters, 2002. **81**(23): p. 4353-4355.

20. Graham, D.M., et al., *Optical and microstructural studies of InGaN/GaN single-quantum-well structures.* Journal of Applied Physics, 2005. **97**(10).

21. Sugahara, T., et al., *Role of dislocation in InGaN phase separation.* Japanese Journal of Applied Physics Part 2-Letters, 1998. **37**(10B): p. L1195-L1198.

22.   Sugahara, T., et al., *Direct evidence that dislocations are non-radiative recombination centers in GaN.* Japanese Journal of Applied Physics Part 2-Letters, 1998. **37**(4A): p. L398-L400.

23.   Chichibu, S., K. Wada, and S. Nakamura, *Spatially resolved cathodoluminescence spectra of InGaN quantum wells.* Applied Physics Letters, 1997. **71**(16): p. 2346-2348.

24.   Bertram, F., et al., *Microscopic correlation of redshifted luminescence and surface defects in thick InxGa1-xN layers.* Applied Physics Letters, 2002. **80**(19): p. 3524-3526.

25.   Bertram, F., et al., *Spatial variation of luminescence of InGaN alloys measured by highly-spatially-resolved scanning cathodoluminescence.* Materials Science and Engineering B-Solid State Materials for Advanced Technology, 2002. **93**(1-3): p. 19-23.

26.   Gerthsen, D., et al., *Composition fluctuations in InGaN analyzed by transmission electron microscopy.* Physica Status Solidi a-Applications and Materials Science, 2000. **177**(1): p. 145-155.

27.   O'Neill, J.P., et al., *Electron-beam-induced segregation in InGaN/GaN multiple-quantum wells.* Applied Physics Letters, 2003. **83**(10): p. 1965-1967.

28.   Okamoto, K., et al., *Confocal microphotoluminescence of InGaN-based light-emitting diodes.* Journal of Applied Physics, 2005. **98**(6).

29.   Dobrovolskas, D., et al., *Confocal spectroscopy of InGaN LED structures.* Journal of Physics D-Applied Physics, 2011. **44**(13).

30.   Okamoto, K., et al., *Submicron-scale photoluminescence of InGaN/GaN probed by confocal scanning laser microscopy.* Japanese Journal of Applied Physics Part 1-Regular Papers Short Notes & Review Papers, 2004. **43**(2): p. 839-840.

31.   O'Donnell, K.P., et al., *Spectroscopic imaging of InGaN epilayers.* Physica Status Solidi B-Basic Research, 1999. **216**(1): p. 157-161.

32.   O'Donnell, K.P., et al., *Confocal microscopy and spectroscopy of InGaN epilayers on sapphire.* Journal of Microscopy-Oxford, 1999. **193**: p. 105-108.

33.   Nakamura, S., et al., *InGaN-based multi-quantum-well-structure laser diodes.* Japanese Journal of Applied Physics Part 2-Letters, 1996. **35**(1B): p. L74-L76.

34.   Morkoç, H.U., *Handbook of Nitride Semiconductors and Devices, Materials Properties, Physics and Growth*. 2009: Wiley.

35.   Oliver, R., *Growth and characterisation of nitride nanostructures*. Materials Science and Technology, 2002. **18**(11): p. 1257-1271.

36.   Pearton, S. and G.U. Fasol, *The Blue Laser Diode: The Complete Story*. 2000: Springer.

37.   Levinshtein, M., *Handbook Series on Semiconductor Parameters*. 1996: World Scientific.

38.   Truell, R., C. Elbaum, and B.B.U. Chick, *Ultrasonic Methods in Solid State Physics*. 1969: Acad. Press.

39.   Bechstedt, F., U. Grossner, and J. Furthmuller, *Dynamics and polarization of group-III nitride lattices: A first-principles study*. Physical Review B, 2000. **62**(12): p. 8003-8011.

40.   Wei, S.H. and A. Zunger, *Valence band splittings and band offsets of AlN, GaN, and InN*. Applied Physics Letters, 1996. **69**(18): p. 2719-2721.

41.   Bernardini, F., V. Fiorentini, and D. Vanderbilt, *Spontaneous polarization and piezoelectric constants of III-V nitrides*. Physical Review B, 1997. **56**(16): p. 10024-10027.

42.   Shi, J.J. and Z.Z. Gan, *Effects of piezoelectricity and spontaneous polarization on localized excitons in self-formed InGaN quantum dots*. Journal of Applied Physics, 2003. **94**(1): p. 407-415.

43.   Tansley, T.L. and C.P. Foley, *Optical Band-Gap of Indium Nitride*. Journal of Applied Physics, 1986. **59**(9): p. 3241-3244.

44.   Wu, J., et al., *Unusual properties of the fundamental band gap of InN*. Applied Physics Letters, 2002. **80**(21): p. 3967-3969.

45.   Hamberg, I. and C.G. Granqvist, *Evaporated Sn-Doped In2o3 Films - Basic Optical-Properties and Applications to Energy-Efficient Windows*. Journal of Applied Physics, 1986. **60**(11): p. R123-R159.

46.   Tansley, T.L. and C.P. Foley, *Infrared-Absorption in Indium Nitride*. Journal of Applied Physics, 1986. **60**(6): p. 2092-2095.

47. Wakahara, A. and A. Yoshida, *Heteroepitaxial Growth of Inn by Microwave-Excited Metalorganic Vapor-Phase Epitaxy.* Applied Physics Letters, 1989. **54**(8): p. 709-711.

48. Petrov, I., et al., *Synthesis of Metastable Epitaxial Zinc-Blende-Structure Ain by Solid-State Reaction.* Applied Physics Letters, 1992. **60**(20): p. 2491-2493.

49. Gerthsen, D., et al., *Molecular beam epitaxy (MBE) growth and structural properties of GaN and AlN on 3C-SiC(0 0 1) substrates.* Journal of Crystal Growth, 1999. **200**(3-4): p. 353-361.

50. Fan, W.J., et al., *Electronic properties of zinc-blende GaN, AlN, and their alloys Ga1-xAlxN.* Journal of Applied Physics, 1996. **79**(1): p. 188-194.

51. Perry, P.B. and R.F. Rutz, *Optical-Absorption Edge of Single-Crystal Ain Prepared by a Close-Spaced Vapor Process.* Applied Physics Letters, 1978. **33**(4): p. 319-321.

52. Berrah, S., A. Boukortt, and H. Abid, *Electronic and optical properties of zincblende AlN, GaN and InN compounds under pressure.* Physica Scripta, 2007. **75**(4): p. 414-418.

53. Levinshtein, M.E., S.L. Rumyantsev, and M.S. Shur, *Properties of Advanced Semiconductor Materials: GaN, AIN, InN, BN, SiC, SiGe*. 2001: Wiley.

54. Wu, J., et al., *Small band gap bowing in In1-xGaxN alloys.* Applied Physics Letters, 2002. **80**(25): p. 4741-4743.

55. Yun, F., et al., *Energy band bowing parameter in AlxGa1-xN alloys.* Journal of Applied Physics, 2002. **92**(8): p. 4837-4839.

56. Li, J., et al., *Optical and electrical properties of Mg-doped p-type AlxGa1-xN.* Applied Physics Letters, 2002. **80**(7): p. 1210-1212.

57. Suzuki, M., et al., *Doping characteristics and electrical properties of Mg-doped AlGaN grown by atmospheric-pressure MOCVD.* Journal of Crystal Growth, 1998. **189**: p. 511-515.

58. Bhattacharya, P.U., *Semiconductor optoelectronic devices*. 1997: Prentice Hall PTR.

59. Fox, M.U., *Optical Properties of Solids*. 2010: OUP Oxford.

60. Martin, R.W. and K.P. O'Donnell, *Calculation of optical transition energies for self-formed InGaN quantum dots.* Physica Status Solidi B-Basic Research, 1999. **216**(1): p. 441-444.

61. Miller, D.A.B., et al., *Band-Edge Electroabsorption in Quantum Well Structures - the Quantum-Confined Stark-Effect.* Physical Review Letters, 1984. **53**(22): p. 2173-2176.

62. Chichibu, S., et al., *Spontaneous emission of localized excitons in InGaN single and multiquantum well structures.* Applied Physics Letters, 1996. **69**(27): p. 4188-4190.

63. Takeuchi, T., et al., *Quantum-confined stark effect due to piezoelectric fields in GaInN strained quantum wells.* Japanese Journal of Applied Physics Part 2-Letters, 1997. **36**(4A): p. L382-L385.

64. Bernardini, F. and V. Fiorentini, *Macroscopic polarization and band offsets at nitride heterojunctions.* Physical Review B, 1998. **57**(16): p. R9427-R9430.

65. Chichibu, S.F., et al., *Optical properties of InGaN quantum wells.* Materials Science and Engineering B-Solid State Materials for Advanced Technology, 1999. **59**(1-3): p. 298-306.

66. Hangleiter, A., et al., *Optical properties of nitride quantum wells: How to separate fluctuations and polarization field effects.* Physica Status Solidi B-Basic Research, 1999. **216**(1): p. 427-430.

67. Waltereit, P., et al., *Nitride semiconductors free of electrostatic fields for efficient white light-emitting diodes.* Nature, 2000. **406**(6798): p. 865-868.

68. Onuma, T., et al., *Localized exciton dynamics in nonpolar (1120) InxGa1-xN multiple quantum wells grown on GaN templates prepared by lateral epitaxial overgrowth.* Applied Physics Letters, 2005. **86**(15).

69. Holst, J.C., et al., *The origin of optical gain in cubic InGaN grown by molecular beam epitaxy.* Applied Physics Letters, 2000. **76**(20): p. 2832-2834.

70. Chichibu, S.F., et al., *Recombination dynamics of localized excitons in cubic InxGa1-xN/GaN multiple quantum wells grown by radio frequency molecular beam epitaxy on 3C-SiC substrate.* Journal of Vacuum Science & Technology B, 2003. **21**(4): p. 1856-1862.

71.   Sasaoka, C., et al., *High-quality InGaN MQW on low-dislocation-density GaN substrate grown by hydride vapor-phase epitaxy.* Journal of Crystal Growth, 1998. **189**: p. 61-66.

72.   Syrkin, A., et al., *First all-HVPE grown InGaN/InGaN MQW LED structures for 460-510 nm.* physica status solidi (c), 2008. **5**(6): p. 2244-2246.

73.   Yamane, T., et al., *Growth of thick AlxGa1-xN ternary alloy by hydride vapor-phase epitaxy.* Journal of Crystal Growth, 2007. **300**(1): p. 164-167.

74.   Ruterana, P., M. Albrecht, and J. Neugebauer, *Nitride semiconductors: handbook on materials and devices*. 2003: Wiley-VCH Verlag GmbH.

75.   Singh, R. and T.D. Moustakas, *Growth of InGaN Films by MBE at the Growth Temperature of GaN.* MRS Online Proceedings Library, 1995. **395**.

76.   Van Hove, J.M., et al., *Molecular beam epitaxy grown InGaN multiple quantum well structures optimized using in situ cathodoluminescence.* Journal of Vacuum Science & Technology B, 1998. **16**(3): p. 1286-1288.

77.   Johnson, M.A.L., et al., *A critical comparison between MOVPE and MBE growth of III-V nitride semiconductor materials for opto-electronic device applications.* Mrs Internet Journal of Nitride Semiconductor Research, 1999. **4**: p. art. no.-G5.10.

78.   Matsuoka, T., et al., *Wide-Gap Semiconductor Ingan and Ingaaln Grown by Movpe.* Journal of Electronic Materials, 1992. **21**(2): p. 157-163.

79.   Morkoc, H., et al., *Large-Band-Gap Sic, Iii-V Nitride, and Ii-Vi Znse-Based Semiconductor-Device Technologies.* Journal of Applied Physics, 1994. **76**(3): p. 1363-1398.

80.   Johnson, M.A.L., et al., *A Critical Comparison Between Movpe and MBE Growth of III-V Nitride Semiconductor Materials for Opto-Electronic Device Applications.* MRS Online Proceedings Library, 1998. **537**.

81.   Chung, T., et al., *Growth of InGaN HBTs by MOCVD.* Journal of Electronic Materials, 2006. **35**(4): p. 695-700.

82.   Yu, H.B., E. Ulker, and E. Ozbay, *MOCVD growth and electrical studies of p-type AlGaN with Al fraction 0.35.* Journal of Crystal Growth, 2006. **289**(2): p. 419-422.

83. Nagatomo, T., et al., *Properties of Ga1-Xinxn Films Prepared by Movpe.* Japanese Journal of Applied Physics Part 2-Letters, 1989. **28**(8): p. L1334-L1336.

84. Wang, Y., et al., *Effects of barrier growth temperature ramp-up time on the photoluminescence of InGaN/GaN quantum wells.* Journal of Applied Physics, 2007. **101**(3).

85. Wu, X.H., et al., *Dislocation generation in GaN heteroepitaxy.* Journal of Crystal Growth, 1998. **189**: p. 231-243.

86. Kwon, Y.B., et al., *On the origin of a-type threading dislocations in GaN layers.* Journal of Vacuum Science & Technology A, 2005. **23**(6): p. 1588-1591.

87. Lee, S.R., et al., *Effect of threading dislocations on the Bragg peakwidths of GaN, AlGaN, and AlN heterolayers.* Applied Physics Letters, 2005. **86**(24).

88. Van de Walle, C.G. and J. Neugebauer, *Universal alignment of hydrogen levels in semiconductors, insulators and solutions.* Nature, 2003. **423**(6940): p. 626-628.

89. Kent, P.R.C. and A. Zunger, *Carrier localization and the origin of luminescence in cubic InGaN alloys.* Applied Physics Letters, 2001. **79**(13): p. 1977-1979.

90. Smeeton, T.M., et al., *Electron-beam-induced strain within InGaN quantum wells: False indium "cluster" detection in the transmission electron microscope.* Applied Physics Letters, 2003. **83**(26): p. 5419-5421.

91. Smeeton, T.M., et al., *Analysis of InGaN/GaN single quantum wells by X-ray scattering and transmission electron microscopy.* Physica Status Solidi B-Basic Research, 2003. **240**(2): p. 297-300.

92. Smeeton, T.M., et al., *The impact of electron beam damage on the detection of indium-rich localisation centres in InGaN quantum wells using transmission electron microscopy.* Journal of Materials Science, 2006. **41**(9): p. 2729-2737.

93. Cerezo, A., T.J. Godfrey, and G.D.W. Smith, *Application of a Position-Sensitive Detector to Atom Probe Microanalysis.* Review of Scientific Instruments, 1988. **59**(6): p. 862-866.

94. Miller, M.K., *Atom probe field ion microscopy.* 1986. p. Medium: X; Size: Pages: 14.

95. Kelly, T.F., et al., *Atom probe tomography of electronic materials.* Annual Review of Materials Research, 2007. **37**: p. 681-727.

96.   Bartel, T.P., et al., *Phase separation in InxGa1-xN*. Philosophical Magazine, 2007. **87**(13): p. 1983-1998.

97.   Hangleiter, A., et al., *Suppression of nonradiative recombination by V-shaped pits in GaInN/GaN quantum wells produces a large increase in the light emission efficiency*. Physical Review Letters, 2005. **95**(12).

98.   Costa, P., et al., *Misfit dislocations in green-emitting InGaN/GaN quantum well structures*. GaN, AIN, InN and Related Materials, 2006. **892**: p. 639-643.

99.   Costa, P.M.F.J., et al., *Misfit dislocations in In-rich InGaN/GaN quantum well structures*. Physica Status Solidi a-Applications and Materials Science, 2006. **203**(7): p. 1729-1732.

100.   Oliver, R.A., et al., *Microstructural origins of localization in InGaN quantum wells*. Journal of Physics D-Applied Physics, 2010. **43**(35).

101.   Silfvast, W.T., *Laser fundamentals*. 1996: University Press.

102.   *Verdi G-series family data sheet*, Coherent Inc.

103.   *Mira optima 900 data sheet*, Coherent Inc.

104.   *Harmonic generator data sheet*, Coherent Inc.

105.   Rulliere, C., *Femtosecond Laser Pulses: Principles and Experiments*. 2005: Springer.

106.   Hecht, E., *Optics*. 2002: Addison-Wesley.

107.   Pearton, S. and G. Fasol, *The Blue Laser Diode: The Complete Story*. 2000: Springer.

108.   Petermann, K., *Laser diode modulation and noise*. 1991: Kluwer Academic Publishers.

109.   Zory, P.S., *Quantum well lasers*. 1993: Academic Press.

110.   *PicoQuant laser diode*, PicoQuant.

111.   *CTI-Cryogenics 8200 compressor user manual*, Trillium.

112.   Lin, F.L., et al., *Confocal and force probe imaging system for simultaneous three-dimensional optical and mechanical spectroscopic evaluation of biological samples.* Review of Scientific Instruments, 2009. **80**(5).

113.   *Time-correlated single photon counting*, PicoQuant.

114.   Robinson, J.W., *Time-Integrated and Time-Resolved Optical Studies of InGaN Quantum Dots*. 2005, University of Oxford.

115.   Leroux, M., et al., *Temperature quenching of photoluminescence intensities in undoped and doped GaN.* Journal of Applied Physics, 1999. **86**(7): p. 3721-3728.

116.   Yasan, A., et al., *Photoluminescence study of AlGaN-based 280 nm ultraviolet light-emitting diodes.* Applied Physics Letters, 2003. **83**(20): p. 4083-4085.

117.   Monemar, B., *Bound excitons in GaN.* Journal of Physics-Condensed Matter, 2001. **13**(32): p. 7011-7026.

118.   Chen, J.H., et al., *Optical and structural properties of InGaN/GaN multiple quantum well structure grown by metalorganic chemical vapor deposition.* Thin Solid Films, 2006. **498**(1-2): p. 123-127.

119.   Feldmann, J., et al., *Linewidth Dependence of Radiative Exciton Lifetimes in Quantum-Wells.* Physical Review Letters, 1987. **59**(20): p. 2337-2340.

120.   Cho, Y.H., et al., *"S-shaped" temperature-dependent emission shift and carrier dynamics in InGaN/GaN multiple quantum wells.* Applied Physics Letters, 1998. **73**(10): p. 1370-1372.

121.   Monemar, B. and B.E. Sernelius, *Defect related issues in the "current roll-off" in InGaN based light emitting diodes.* Applied Physics Letters, 2007. **91**(18).

122.   Li, Y., et al., *Cathodoluminescence Studies of InGaN/GaN Multiple Quantum Well Structure Grown by Metal Organic Chemical Vapor Deposition* in *ECS Transactions*. 2012. p. 31-38.

123.   Berkowicz, E., et al., *Optical spectroscopy of InGaN/GaN quantum wells.* Physica Status Solidi B-Basic Solid State Physics, 1999. **216**(1): p. 291-300.

124.   Feng, S.W., et al., *Multiple-component photoluminescence decay caused by carrier transport in InGaN/GaN multiple quantum wells with indium aggregation structures.* Applied Physics Letters, 2002. **80**(23): p. 4375-4377.

125. Kucheyev, S.O., et al., *Chemical origin of the yellow luminescence in GaN.* Journal of Applied Physics, 2002. **91**(9): p. 5867-5874.

126. Saarinen, K., et al., *Observation of native Ga vacancies in GaN by positron annihilation.* Physical Review Letters, 1997. **79**(16): p. 3030-3033.

127. Armour, E.A., et al., *Effect of Growth Pressure and Gas-Phase Chemistry on the Optical Quality of InGaN/GaN Multi-Quantum Wells.* MRS Online Proceedings Library, 2013. **1538**: p. 341-351.

128. Keller, S., et al., *Growth and characterization of bulk InGaN films and quantum wells.* Applied Physics Letters, 1996. **68**(22): p. 3147-3149.

129. Wang, F., et al., *Mg acceptor energy levels in Al(x)In(y)Ga(1-x-y)N quaternary alloys: An approach to overcome the p-type doping bottleneck in nitrides.* Physical Review B, 2008. **77**(11).

130. Wei, S.H., *Overcoming the doping bottleneck in semiconductors.* Computational Materials Science, 2004. **30**(3-4): p. 337-348.

131. Van de Walle, C.G. and J. Neugebauer, *First-principles calculations for defects and impurities: Applications to III-nitrides.* Journal of Applied Physics, 2004. **95**(8): p. 3851-3879.

132. Nakamura, S. and S.F. Chichibu, *Introduction to Nitride Semiconductor Blue Lasers and Light Emitting Diodes*. 2000: Taylor & Francis.

133. Nakamura, S., M. Senoh, and T. Mukai, *Highly P-Typed Mg-Doped Gan Films Grown with Gan Buffer Layers.* Japanese Journal of Applied Physics Part 2-Letters, 1991. **30**(10A): p. L1708-L1711.

134. Saxler, A., et al., *Aluminum gallium nitride short-period superlattices doped with magnesium.* Applied Physics Letters, 1999. **74**(14): p. 2023-2025.

135. Bremser, M.D., et al., *Growth, doping and characterization of AlxGa1-xN thin film alloys on 6H-SiC(0001) substrates.* Mrs Internet Journal of Nitride Semiconductor Research, 1996. **1**(1-46): p. U59-U71.

136. Katsuragawa, M., et al., *Thermal ionization energy of Si and Mg in AlGaN.* Journal of Crystal Growth, 1998. **189**: p. 528-531.

137. Lopatiuk, O., A. Osinsky, and L. Chernyak. *Studies of electron trapping in III-nitride semiconductors*. 2006.

138.   Amano, H., et al., *P-Type Conduction in Mg-Doped Gan Treated with Low-Energy Electron-Beam Irradiation (Leebi).* Japanese Journal of Applied Physics Part 2-Letters, 1989. **28**(12): p. L2112-L2114.

139.   Nakano, Y., O. Fujishima, and T. Kachi, *High-temperature annealing behavior of p-type doping characteristics in Mg-doped GaN.* Journal of the Electrochemical Society, 2004. **151**(9): p. G574-G577.

140.   Gotz, W., et al., *Deep-Level Defects in N-Type Gan.* Applied Physics Letters, 1994. **65**(4): p. 463-465.

141.   Gotz, W., et al., *Activation energies of Si donors in GaN.* Applied Physics Letters, 1996. **68**(22): p. 3144-3146.

142.   Tauc, J., *Optical Properties and Electronic Structure of Amorphous.* Materials Research Bulletin, 1968. **3**(1): p. 37-&.

143.   Ridley, B.K., *Quantum Processes in Semiconductors*. 1999: OUP Oxford.

144.   Ejder, E., *Refractive Index of Gan.* Physica Status Solidi a-Applied Research, 1971. **6**(2): p. 445-&.

145.   Pastrnak, J. and Roskovco.L, *Refraction Index Measurements on Ain Single Crystals.* Physica Status Solidi, 1966. **14**(1): p. K5-&.

146.   McGill, S.A., et al., *Bound-polaron model of effective-mass binding energies in GaN.* Physical Review B, 1998. **57**(15): p. 8951-8956.

147.   Osotchan, T., et al., *Electronic Band-Structure of Alxga1-Xas/Alyga1-Yas/Gaas Double-Barrier Superlattices.* Physical Review B, 1994. **50**(4): p. 2409-2419.

148.   Pankove, J.I., S. Bloom, and G. Harbeke, *Optical-Properties of Gan.* Rca Review, 1975. **36**(1): p. 163-176.

149.   Kim, K., et al., *Effective masses and valence-band splittings in GaN and AlN.* Physical Review B, 1997. **56**(12): p. 7363-7375.

APPENDIX

A.1 P-type AlGaN

A.1.1 Introduction

Since the first introduction of AlGaN, there have been a lot of efforts to obtain p-type AlGaN. However, as mention in Section 1.1.5, it is very difficult to obtain p-type doping for AlGaN because of its large bandgap energy and the lack of shallow acceptor levels [129-131]. Moreover, because of the intrinsic defects such as vacancies, AlGaN has a natural and strong tendency to exhibit n-type conductivity. The intrinsic defects may either introduce donor levels in the bandgap, or act as compensating centers which reduce the function of the intentional p-type dopant. For example, nitrogen vacancies can act as donors to provide donor levels, making undoped AlGaN n-type conductive; nitrogen vacancies can also act as compensating center in p-type AlGaN, and in this case the function of the intentionally incorporated acceptor impurity would be abated. In addition, unintentionally incorporated impurities could also make AlGaN show n-type conductivity. For example, oxygen, which comes from water-contaminated ammonia source, or silicon, which comes from the substrate if silicon or SiC substrate is used, can be unintentional n-type dopant for AlGaN.

A.1.2 P-type Dopant Elements in AlGaN

There are three factors that are used to evaluate the role of a p-type dopant element in a semiconductor material: 1) solubility, which defines the equilibrium concentration of the p-type dopant in the lattice of the semiconductor material; 2) compensation stability, which defines the stability of a given p-type dopant against

compensation by other configurations; 3) ionization energy, which is the energy required to ionize the acceptor atoms [132].

The p-type dopants for AlGaN are generally elements from Group I and Group II. For Group I, lithium has been tried as p-type dopants. For Group II, beryllium, cadmium, calcium, magnesium, mercury, and zinc have been tried as p-type dopants. It was found that comparing with elements of Group I, elements of Group II show much better solubility in AlGaN. In Group II, researches showed that Zn (zinc) and Mg were promising p-type dopant for AlGaN. However, since Zn tends to compensate III-N semiconductors, it leads to the production of very resistive semiconductor materials [34]. As a result, Mg is currently the most promising and commonly used p-type dopant for not only AlGaN but also GaN and InGaN. Hole concentration of Mg-doped AlGaN at room temperature is generally smaller than 3×10^{18} cm^{-3} with a mobility of 9 cm^2/Vs [133].

During the crystal growth, Mg can be introduced into AlGaN using different methods. In MBE, Mg is introduced by being evaporated from a high pure solid source in Knudsen effusion cells. In MOCVD, Mg is introduced by using metalorganic precursor Cp$_2$Mg (bis(cyclopentadienyl)magnesium).

It should be mentioned that carbon has also been tried as p-type dopant for AlGaN. However, researches showed that carbon tends to be amphoteric in AlGaN: it acts as donor if carbon is located on Ga-site, while acts as acceptor if carbon is located on N-site. In this case, as it is not easy to control where carbon is located, it's not a good candidate for p-type dopant.

A.1.2.1 Ionization Energy of Mg in AlGaN

One drawback of Mg as acceptor dopant is that the acceptor has very large ionization energy. To make things worse, the acceptor ionization energy increases with increasing Al mole fraction [134-136]. Mg ionization energy in AlGaN has been reported to be 260 meV and 310 meV for an Al mole fraction of 27% and 30% respectively by Saxler [134], 232 meV and 252 meV for an Al mole fraction of 15% and 20% respectively by Chernyak [137]. Figure A.1 shows the Mg acceptor ionization as a function of the Al mole fraction, which is calculated by Saxler [57].

This acceptor ionization energy is much higher than the thermal energy at room temperature, which is 25.9 meV. As a result, at room temperature, very few Mg acceptors can be ionized. Researches show that acceptor activation ratio is smaller than 10^{-2}, so an Mg concentration of 10^{20} cm^{-3} is required [134] to get a reasonable hole concentration of the order of 10^{18} cm^{-3}.
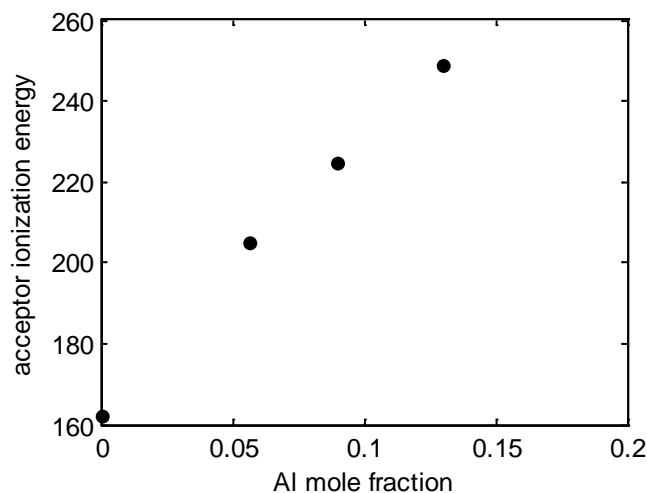

Figure A.1: Mg acceptor ionization energy vs. Al mole fraction in AlGaN [57].

A.1.2.2 Counteracting Role of Hydrogen

Hydrogen contamination is very difficult to be removed, since the very small size of the hydrogen atom makes it very easy to diffuse through the walls of the MOCVD reactor or MBE reactor, and since the hydrogen is sometimes used as carrier gas in MOCVD and HVPE growth.

The hydrogen contamination can greatly affect the electrical behavior of p-type Mg-doped AlGaN, resulting in high resistivity. This is because hydrogen atoms can act as donor in Mg-doped AlGaN and passivate Mg atoms by forming a Mg-H bond, as shown in Figure A.2.
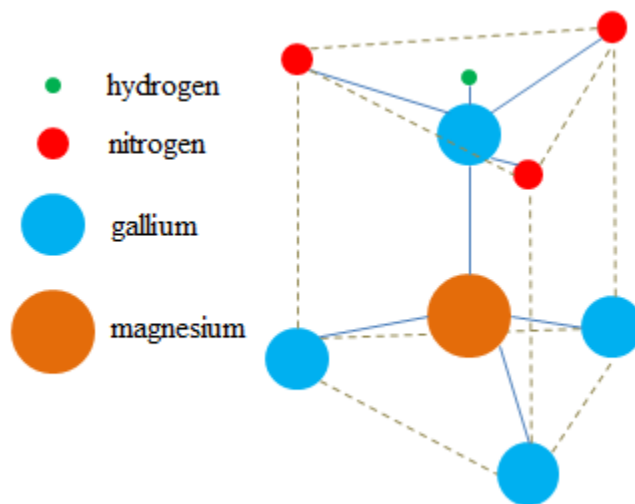

Figure A.2: Schematic diagram of the Mg-H bond in GaN. The hydrogen is located in the anti-bonding site, which is thought to be the most favorable place. [132]

Researches have also shown that in MOCVD growth hydrogen plasma treatment can passivate Mg-doped AlGaN; this treatment is often used to prepare the surface of sapphire substrate before the deposition of AlN buffer layer, or used for surface passivation as a post-growth treatment.

A.1.2.3 Activation of Mg Acceptors

In order to make the p-type Mg dopant work and make the doped AlGaN p-type conductive, it is very necessary to break the Mg-H bond, which is responsible for the passivation of Mg acceptor in Mg-doped AlGaN, as mentioned in the previous section. There are two methods to for Mg acceptor activation: LEEBI (low energy electron beam irradiation) and RTA (rapid thermal anneal).

First, the Mg-H bond can be broken by means LEEBI, which is the technique that was used to produce the very first Mg-doped GaN sample that showed p-type conductivity [138]. This is because the electron beam generates electron-hole pairs in the semiconductor material which can either provide enough energy to provoke the dissociation of the Mg-H bond, or lower its energy level [132].

More common methods of activating Mg acceptors in Mg-doped AlGaN are RTA and HTA (high temperature anneal), which are generally conducted in-situ as a post-growth treatment. Researches have shown that the effective hole concentration increased with increasing anneal temperature, and resistivity decreased with increasing anneal temperature [139-141].

A.2 P-type AlGaN Thin Film Grown by MOCVD

The AlGaN sample in this research was an Mg doped p-type AlGaN. It was provided by Sensor Electronic Technology Inc. and was grown by MOCVD. The AlGaN sample was grown on double side polished planar c-plane oriented (0001) sapphire substrate.

The sapphire substrate was first in-situ cleaned in hydrogen (H_2) atmosphere, to achieve clean surface for the following crystal growth. 400-nm-thick AlN buffer layer

was grown on sapphire substrate, followed by 200-nm-thick nominally undoped AlGaN. Finally, 150 nm thick Mg doped AlGaN was deposited. The Al mole fraction of Mg doped AlGaN was kept the same as that of undoped AlGaN, both of which were between 30 % and 35%. A schematic diagram of the sample structure is shown in Figure 2.9.
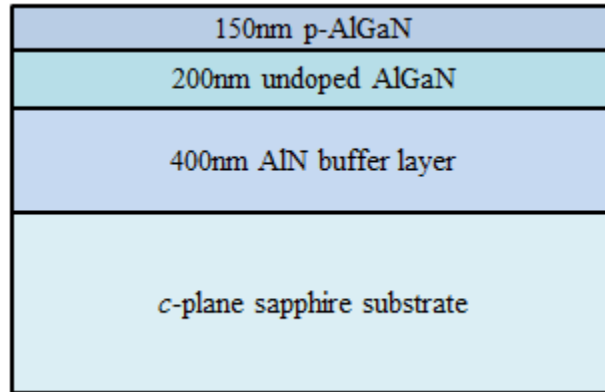
| 150nm p-AlGaN |
| 200nm undoped AlGaN |
| 400nm AlN buffer layer |
| c-plane sapphire substrate |

Figure A.3: Structure of p-AlGaN sample provided by Sensor Electronic Technology Inc.

A.3 IR Absorption in Mg Doped AlGaN

The structure of the Mg doped p-type AlGaN was introduced in Section 1.3.2.5. Since the sapphire substrate was double side polished and AlN, which has larger bandgap energy than GaN did, was used as buffer layer, transmission spectroscopy could be applied.

Figure A.4 shows the transmission spectrum of the sample measured by a VARIAN UV-VIS-IR spectrophotometer. Based on the transmission spectrum, the absorption coefficient spectrum can be calculated as:
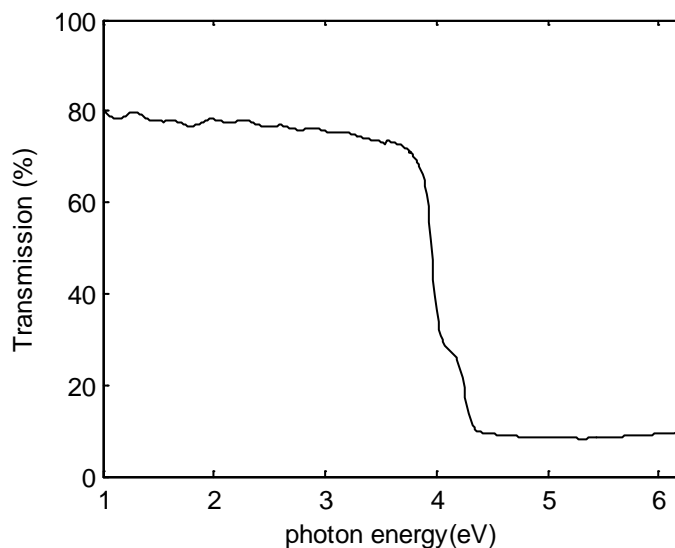
$$\alpha = -\frac{1}{t}\ln(T1), \tag{A.1}$$

Figure A.4: Transmission spectrum of AlGaN sample, measured by UV-VIS-IR spectrophotometer.

where t=350 nm is the total thickness of the p-type AlGaN layer and undoped AlGaN layer (as they have same amount of Al mole fraction), and $T1$ is the transmission shown in Figure A.4. Notice that the 88.7% transmission of bare double side polished sapphire substrate has already been removed during the calculation. The absorption coefficient spectrum is shown in Figure A.5. Based on Tauc's model [142], the bandgap energy could be obtained from the absorption edge. Squared absorption coefficient multiplying by squared photon energy was plotted as a function of photon energy, and linear curve fitting was done on the part where the transmission changed fast, as indicated in Figure A.6. The intersection of the linear fitting line and the x-axis, which is also called the absorption edge, indicates the AlGaN bandgap energy. The bandgap energy was identified to be 4.14 eV in the experiment through calculation. Based on Equation (1.3), the alloy contained 33% of Al. This experiment-derived Al mole fraction was in consistence with the estimated Al mole fraction that was controlled during the sample growth (between 30% and 35%). It should be noted that in Figure A.6 there is a small

shoulder near the absorption edge. Linear curve fitting of the shoulder showed intersection energy that is 240 meV smaller than the bandgap energy. This energy level corresponds to the acceptor-bond exciton level [117].
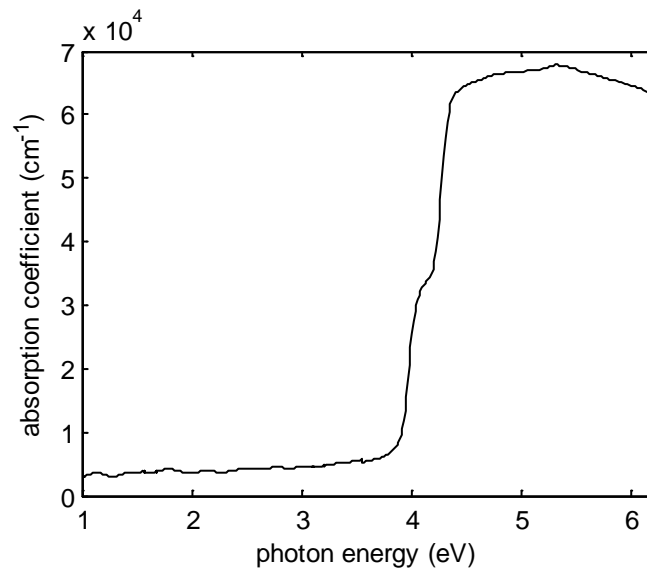

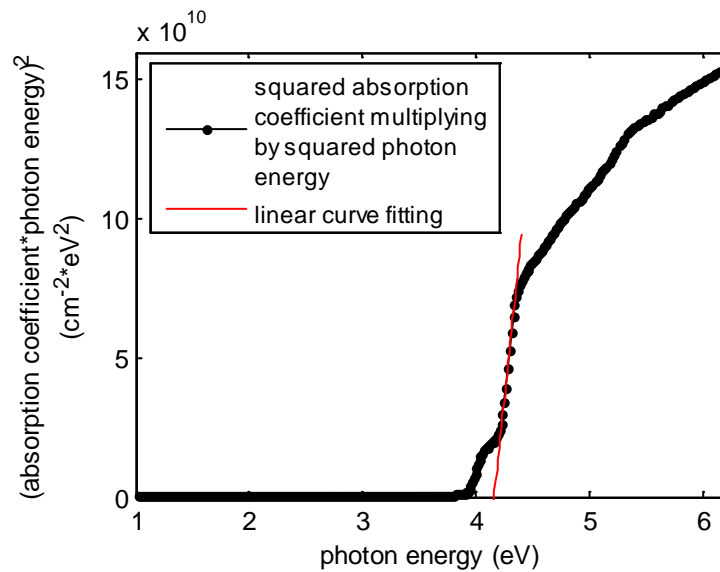Figure A.5: Absorption coefficient spectrum of the AlGaN sample.

Figure A.6: Squared absorption coefficient multiplying by squared photon energy vs. photon energy. The intersection between the linear fitting line and the *x*-axis indicates the bandgap energy.

Figure A.7 shows the transmission spectrum of AlGaN in IR region. Nd:YAG laser pumped OPO/OPA system and OPHIR energy meter were used to measure this transmission spectrum: the output energy spectrum of the Nd:YAG laser pumped OPO/OPA system was measured with and without the AlGaN sample presenting at the output of the OPO/OPA system, and the transmission spectrum was then calculated by

$$T2 = \frac{I_{sample}(\lambda)}{I_0(\lambda)} \tag{A.2}$$

where $I_0(\lambda)$ is the output energy spectrum taken without AlGaN sample presented, and $I_{sample}(\lambda)$ is the energy spectrum taken with AlGaN sample presented. The figure indicates that the transmission decreases by around 10% when the photon energy increases beyond 500 meV, which is proposed to be the result of photon absorption by acceptors. To identify the acceptor ionization energy, as well as the ionized acceptor concentration (hole concentration), here a curve fitting method was proposed.
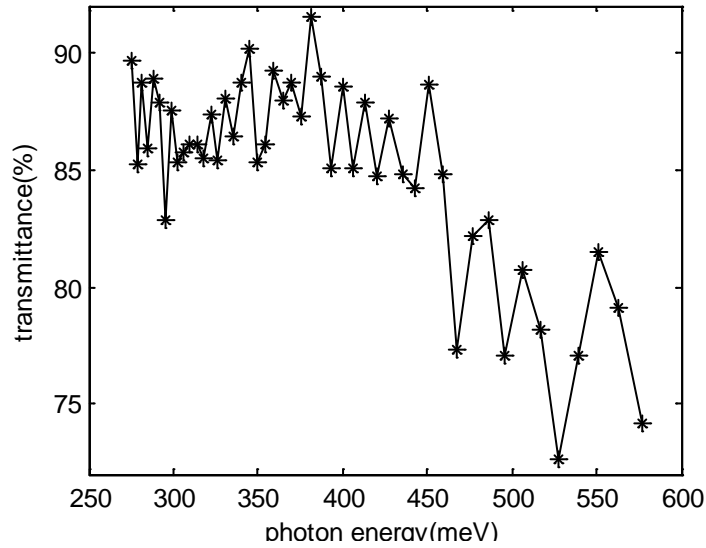
Figure A.7: Transmission spectrum of AlGaN sample, measured by OPO/OPA and power meter.

Based on the IR transmission spectrum, OD (optical density, also called absorbance) spectrum can be calculated by

$$OD_e = -\log_{10}(\frac{I_{sample}(\lambda)}{I_0(\lambda)}) = -\log_{10}(T2),$$ (A.3)

as indicated in Figure A.9, where the subscript e indicates that this OD value is calculated from experimental data. Similar as before, the 88.7% transmission of bare double side polished sapphire substrate has already been removed during the calculation.

On the other hand, OD can also be calculated by

$$OD_f = -\log_{10}(\frac{I_{sample}(\lambda)}{I_0(\lambda)}) = -\log_{10}(\frac{A - A\sigma_v N_A^- t}{A}) = -\log_{10}(1 - \sigma_v N_A^- t)$$ (A.4)

where A is the AlGaN sample surface area, $t = 150$ nm is the Mg doped p-type AlGaN layer thickness, N_A^- is the ionized acceptor concentration (the hole concentration) in p-type AlGaN layer, σ_v is acceptor photo-ionization cross section, and the subscript f indicates that the OD is calculated from theoretical formulas. Equation (A.4) is valid

under the assumption that acceptors do not overlap with each other in c-plane, which means that if a straight line is drawn along c-axis from the substrate to the sample surface, it will encounter one acceptor at most, as shown in Figure A.8(a). Since the acceptor density is several orders of magnitudes smaller than the intrinsic atom density, this assumption is reasonable. Under this assumption, in Equation (A.4) the light intensity ratio can be transformed into area ratio, in which $AN_A^- t$ shows the amount of ionized acceptors (holes), $A\sigma_v N_A^- t$ shows the total area of the ionized acceptors, and $A - A\sigma_v N_A^- t$ shows the total area of the region in which no acceptors become ionized (or to say, no IR light is absorbed). Based on B. K. Ridley's work [143], the acceptor photo-ionization cross section is calculated by:
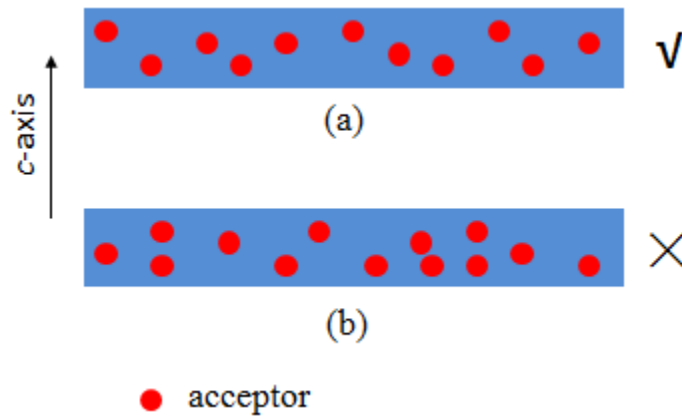

acceptor

Figure A.8: (a) the model of calculation in Equation A.4, no acceptors overlap in c-axis; (b) acceptors overlap in c-axis, which is not reasonable under low doping density.

$$\sigma_v = \frac{16}{3}\alpha a_H^2 \left(\frac{R_H}{\hbar\omega_v}\right)\frac{1}{\eta_r}\frac{m}{m^*}\frac{2\pi\left(v_T a_H^*\right)^3 \left(2m^*/\hbar^2\right)^{3/2} E_k^{3/2}}{\left[1+\left(E_k/E_T\right)\right]^2} \tag{A.5}$$

where

$$\alpha = \frac{e^2 / 4\pi\varepsilon_0}{\hbar c},$$

$$a_H = \frac{\hbar^2 / m}{e^2 / 4\pi\varepsilon_0},$$

$$a_H^* = \frac{m\varepsilon}{m^*\varepsilon_0} a_H,$$

$$R_H = \frac{e^2 / 4\pi\varepsilon_0}{2a_H}, \qquad \text{(A.6)}$$

$$R_H^* = \frac{\left(e^2 / 4\pi\varepsilon\right)^2}{2\left(\hbar^2 / m^*\right)},$$

$$v_T = \left(R_H^* / E_T\right)^{1/2},$$

$$E_k = \hbar\omega_v - E_T,$$

$$\varepsilon = \varepsilon_0\varepsilon_r,$$

E_T is acceptor ionization energy, $\hbar\omega_v$ is photon energy, η_r is refractive index, m is free electron mass, and m^* is hole effective mass. Parameters for p-type $Al_{0.33}Ga_{0.67}N$ are calculated based on Vegard's linear law and the parameters of GaN and AlN, and are listed in Table A.1. So Equation (A.5) can be simplified as

$$\sigma_v = \frac{1.85 \times \dfrac{1}{\hbar\omega_v} \times \left(\dfrac{\hbar\omega_v - E_T}{E_T}\right)^{3/2}}{\left(\dfrac{\hbar\omega_v}{E_T}\right)^2}. \qquad \text{(A.7)}$$

Substitution of σ_v in Equation (A.4) with Equation (A.7) results in

$$OD_f = -\log_{10}\left[1 - N_A^- t \frac{1.85 \times \dfrac{1}{\hbar\omega_v} \times \left(\dfrac{\hbar\omega_v - E_T}{E_T}\right)^{3/2}}{\left(\dfrac{\hbar\omega_v}{E_T}\right)^2}\right]. \qquad \text{(A.8)}$$

Table A.1: Parameters for GaN, AlN, and $Al_{0.33}G_{0.67}N$.

	GaN	AlN	$Al_{0.33}G_{0.67}N$
Band gap energy(eV)	3.44	6.2	4.14
Infrared refractive index	2.33 [144]	2.15 [145]	2.27
Dielectric constant (static 300K)	8.9 [146]	8.5 [147]	8.77
Relative hole effective mass	0.8 [148]	5.6 [149]	1.5

Equation (A.8) shows that the OD is actually a function of photon energy, acceptor ionization energy and ionized acceptor concentration (hole concentration). In this case, it is possible to fit the OD_e with OD_f, by adjusting the values for acceptor ionization energy and ionized acceptor concentration (hole concentration). Figure A.9 shows the best fitting result, which gives acceptor ionization energy of 390 meV and ionized acceptor concentration (hole concentration) of 1.8×10^{18} cm^{-3}. Based on Suzuki's work [57], Mg doped p-type AlGaN alloy with 33% of Al is supposed to have acceptor ionization energy of 385 meV, as indicated in Figure A.10, which agrees well with the experiment result here, with only 1% difference.
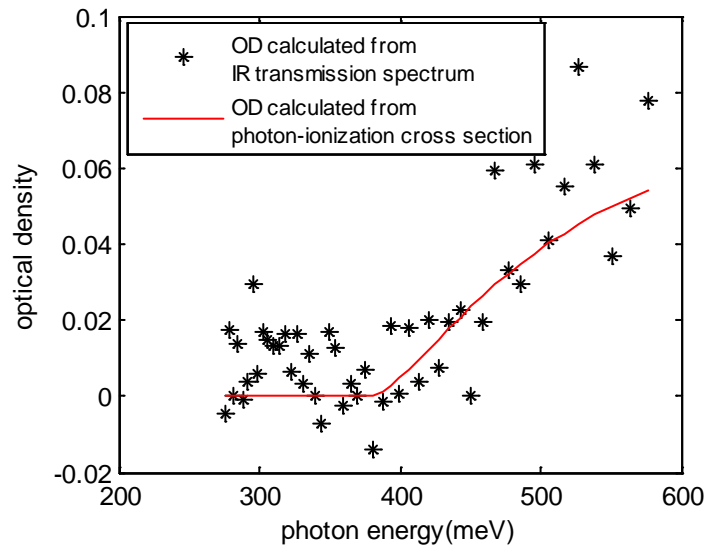

Figure A.9: OD calculated by both Equation (A.3) and Equation (A.4), the R-square for the fitting is 0.6155.
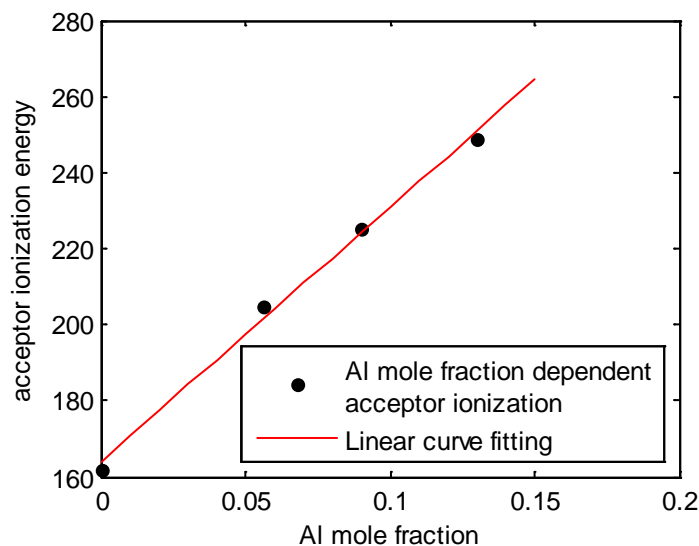
Figure A.10: The relation between acceptor ionization energy and Al mole fraction, replotted from ref [57], and the linear fitting for it. The adjusted R-square of the fitting is 0.9927.

As a result, it is possible to identify the acceptor ionization energy and the ionized acceptor concentration (hole concentration) by measuring the material's IR transmission spectrum and fitting OD_e, which is calculated based on IR transmission spectrum, with OD_f, which is calculated based on theoretical formulas. Comparing with traditional characterization techniques such as Hall effect measurement and DLTS (deep level transient spectroscopy) measurement, this optical characterization technique is simple and non-destructive.